ISSN 0915-6348

NATIONAL INSTITUTE FOR FUSION SCIENCE

Proceedings of Workshop on Emissions from Heavy Current Carrying High Density Plasma and Diagnostics

(Received – Apr. 5, 1991)

NIFS-PROC-7 May, 1991

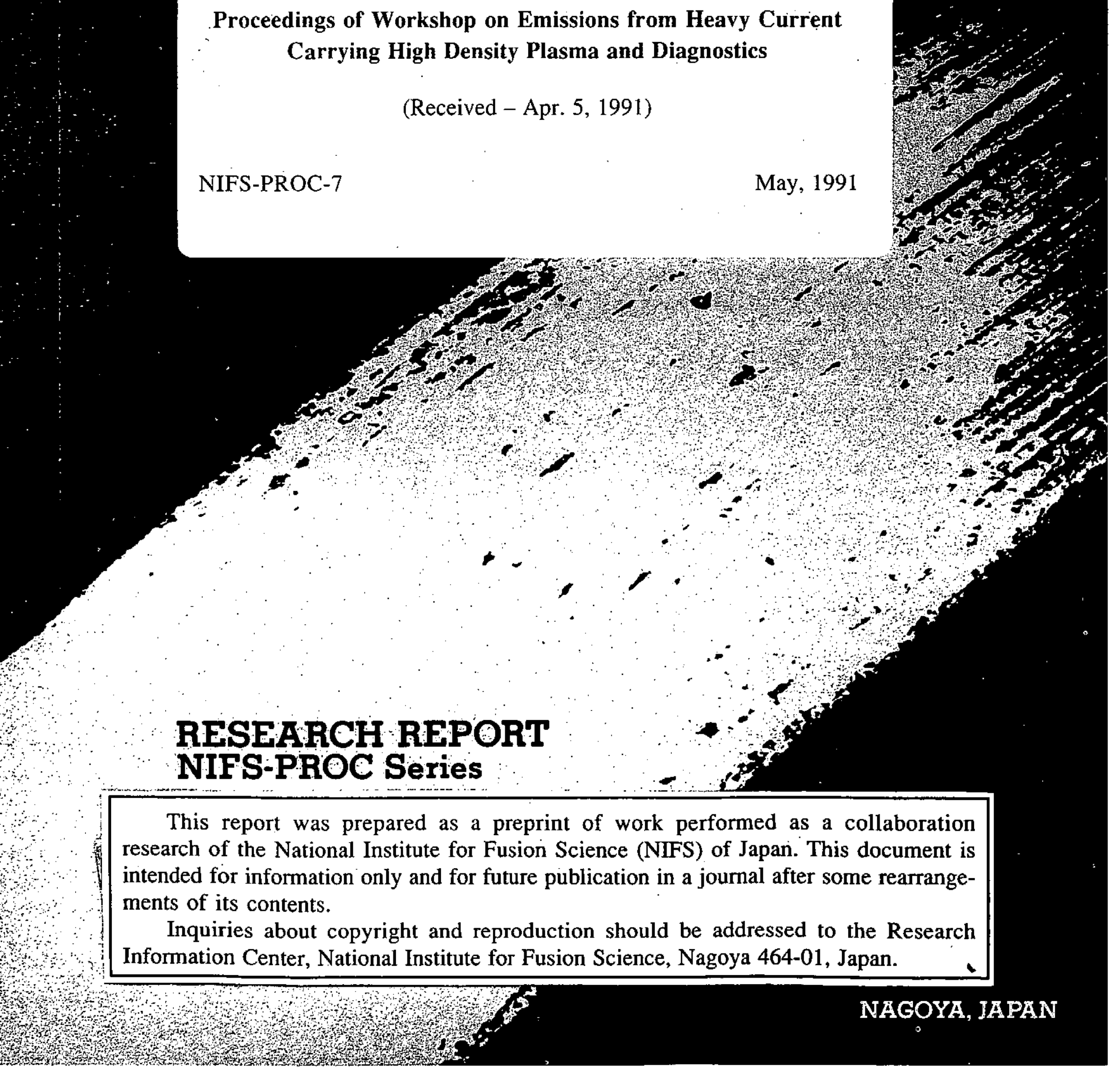

RESEARCH REPORT
NIFS-PROC Series

NAGOYA, JAPAN

Proceedings of Workshop on Emissions from Heavy Current Currying High Density Plasma and Diagnostics

Edited by Katsumi Hirano

Keywords; Z Pinch, Plasma Focus, Intense Charged Particle Beams, Soft X rays, UV laser, Pulse Power Technology, High Voltage Technology, Megagauss Field.

Emission from heavy current carrying high density plasma and their diagnostics

Edited by Katsumi Hirano

Abstract

Workshop on "Emissions from heavy current carrying high density plasma and diagnostics" was held at National Institute for Fusion Science, Nagoya on 5. and 6. December 1990 under a collaborating research Program.

The workshop was attended by 35 researchers from 18 laboratories. A total of 10 papers were submitted and are presented in these proceedings. The largest group of papers was that on soft X-ray, ion- and electron beam emission. It seems these topics are foremost interest for groups which engaged in research of the pulse power generator, the Z pinch and the plasma focus. A variety of problems in pinched dense plasmas, namely spectroscopy, diagnostics, pinch dynamics, and related engineering aspects were also discussed.

The editor of these proceedings wish to thank all authors of papers, workshop participants and the Sub-commitee on Scientific Research Collaborations of the National Institute for Fusion Science who contributed to the success of this workshop.

A SPECTROSCOPIC STUDY OF A PLASMA LIGHT SOURCE EXCITED BY A DOUBLE BLUMLEIN PULSE FORMING NETWORK

Ken SATOH and Tetsuya AKITSU
Department of Electrical Engineering and Computer Science,
Yamanashi University
Kofu,Yamanashi 400 Japan

1. Introduction

In coaxial pinch discharges, high density plasma can be produced by the use of comparatively simple devices. In this paper, we present a spectroscopic study of a plasma light source which can be used in the study on the electron and ion dynamic effect on spectral emission. Such plasma light source can find practical use in the field of optical excitation.

2. Experimental apparatus

Figure 1 shows a pulse plasma light source, which consists of a double Blumlein PFN and coaxial electrodes. The discharge was initiated by a pressurized N_2 trigger gap switch. The PFN consists of four layers 30 ceramic capacitors with 2000pF each capacitance. The total capacitance of this PFN is 0.24μF. The stored energy is 52.3J in a repetitively used experimental condition and 108J at the maximum charging voltage of 30kV. The coaxial electrodes, 1mm OD Th-W cathode settled at the center of 19mmID hollow anode, with 100mm in length was settled in a vacuum chamber and spectral emission was observed through a quartz window.

The intensity of spectral emission was measured by the use of a spectromator (Nihon Bunkou, CT-25C) and a photo-multiplier (Hamamatsu, R-376). The relative spectral sensitivity of this system was calibrated by the use of a standard halogen tungsten lamp with 3111°K. The intensity of total light and soft X-ray were measured by pin diode (Hamamatsu,1722-02).

3. Electrical characteristics of Blumlein PFN

Figure 2 shows output voltage and current wave form of the PFN terminated by a $CuSo_4$ liquid resistor. The pulse width is 500ns with negative polarity when the intermidiate layer was charged with positive polarity.

The phase velocity was estimated from the pulse width and the total inductance of the distributed inductance was estimated as $L=0.26\mu H$ where the phase velocity $U_p=4x10^6 m/s$ determined by $U_p=(LC)^{-1/2}$ combining with the total capacitance. The characteristic impedance $Z_0=1.04$.

In a series of experiment, we observed a change of output voltage waveform depending on the stray inductance of the trigger gap and distributed inductance of the PFN. The effect of these circuit parameters was studied by the use of an analogue circuit simulator, Micro Cap III, Spectrum Software, with a circuit model shown in fig.3(a). One can find a reasonable correlation between the result of this simulation, fig.3(b), and the experimental result. This result suggests that the design of PFN becomes much easier when such analogue circuit simulator was used. Some of the circuit parameters can be estimated even if the measurement of these parameters are practically difficult in the experiment.

As the PFN has a distributed circuit characteristics, the output voltage wave form can be tailored by changing the number of ceramic capacitors. Figure 4 shows this change of the voltage wave form when the number of capacitors at each layer was changed from 30 to 15 and one. The pulse width changed from 500 ns to 100 ns.

4. Spectral emission of a helium plasma excited by PFN discharge

(a) Stark broadening of HeI, 388.9nm and 587.6nm

Stark broadening was used as a diagnostic tool for the electron density. The maximum half width $\Delta\lambda_{1/2}$ of each spectral line can be related to the electron density N and temperature T_e, in the following form.

$$\Delta\lambda_{1/2}=2W\left(\frac{N}{10^{16}}\right)+3.5A\left(\frac{N}{10^{16}}\right)^{1/4}\left[1-\frac{3}{4}N_D^{-1/3}\right]W\left(\frac{N}{10^{16}}\right)\quad[\text{Å}]$$

where w=0.115, A=0.068 and D=0.047 for 388.9nm and w=0.174, A= 0.0597 and D=-0.029 for 587.6nm.

The profile of 388.9nm line was compared with a Gaussian profile in fig.5, which was measured in the case of V_c=-12kV and helium pressure p=2 Torr. A series of similar experiment were carried out and summerized in table1. The result for 587.6nm is shown in table 2.

TABLE 1 He I 3889Å Stark broadenig and electron density

Voltage [-kV]	Pressure [torr]	He density [cm^{-3}]	$\Delta\lambda_{1/2}$ [Å]	$\Delta\lambda_{1/2}$(A-G) [Å]	n_e [cm^{-3}]	n_e(A-G) [cm^{-3}]
12	0.5	1.6×10^{16}	3.0	—	1.1×10^{17}	—
12	2	6.6×10^{16}	2.0	1.5	7.5×10^{16}	4.9×10^{16}
12	10	3.3×10^{17}	2.3	2.3	8.6×10^{16}	8.6×10^{16}
18	0.5	1.6×10^{16}	1.9	2.0	7.1×10^{16}	7.5×10^{16}
18	2	6.6×10^{16}	2.2	3.0	8.2×10^{16}	1.1×10^{17}
18	10	3.3×10^{17}	1.8	3.6	6.8×10^{16}	1.3×10^{17}

(A-G:After Grow)

TABLE 2 He I 5876Å Stark broadenig and electron density

Voltage [-kV]	Pressure [torr]	He density [cm^{-3}]	$\Delta\lambda_{1/2}$ [Å]	n_e [cm^{-3}]
12	0.5	1.6×10^{16}	3.0	7.6×10^{16}
12	2	6.6×10^{16}	3.4	8.5×10^{16}
12	10	3.3×10^{17}	4.4	1.1×10^{17}
18	0.5	1.6×10^{16}	4.5	1.1×10^{17}

Figure 6 shows the variation of the intensity of 388.9nm when the helium pressure was changed from 0.2 to 20 Torr. One can recognize the enhancement of this line during the decay phase of the after glow plasma, which corresponds to 5 to 10μsec after the termination of electric energy input.

(b) Stark broadening of He II,468.6nm

A hydrogen-like, singly ionized helium ion can be used as a standard of line broadening. In a series of experiments, we obtained $\Delta\lambda_{1/2}$ = 4.0 to 4.8 angstroms, which corresponds to N= 8×10^{16} to 1.1×10^{17}cm^{-3}. This result shows reasonable agreement to the former results.

(c)Stark broadening of He I,447.1nm-446.9nm, forbidden allowed line pair

Some of the recent studies on line broadening have suggested the practical usage of the so-called forbidden allowed line pair as a diagnostic tool for the electron temperature. In the context of Stark broadening theory forbidden lines occur as a result of the breakdown of the parity selection rules induced by the electrostatic micro fields by electron collision. The Stark effect on F-A pair is more complicated than isolated lines discussed in the former section. Figure 7 shows typical profiles of the allowed 2^3P-4^3D and the forbidden 2^3P-4^3F transitions.

The ratio of peak intensities, the ratio of valley to peak intensity and the separation between peaks were measured varing the charging voltage and helium pressure. The result of this experiment showed a good agreement to the result obtained from isolated lines.

(d)Intensity ratio of He II,468.6nm/He I,587.6nm

The electron temperature was estimated from the intensity ratio of a singly ionized helium line to a neutral helium line using Mewe's model.

A criterion for the conservation of LTE condition given by McWhirter is,

$$N \gtrsim 1.4\times 10^{14} T^{1/2} [E\ (m, n)]^{3} \quad [cm^{-3}]$$

where T denotes for electron temperature and E is the energy separation between levels in eV. In the present experiment, we neglect low energy lines and the criterion can be reduced to,

$$N \gtrsim 2\times 10^{18} \frac{Z^{6}\sqrt{T(eV)}}{n^{17/2}} \quad [cm^{-3}]$$

where n denotes for the principle quantum number,Z ionic charge. The second criterion can be satisfied if the electron density is greater than $10^{16}cm^{-3}$.

The result of the present experiment and estimation of electron temperature are summerized in table 3.

TABLE 3 Electron Temperature from the Spectral-line intensity ratio of He II 4686 Å/He I 5876 Å

Voltage [kV]	Pressure [torr]	He density [cm^{-3}]	intensity ratio	T_e [eV]
12	0.5	1.6×10^{16}	0.85	4.9
12	2	6.6×10^{16}	0.87	4.9
12	10	3.3×10^{17}	0.81	4.8
18	0.5	1.6×10^{16}	0.78	4.7

6. Conclusion

A combination of a coaxial electrode and double Blumlein PFN produced relatively high density plasma despite the simplicity of experimental apparatus. Double Blumlein PFN has a capacity of -21kV,5.6kA pulse output with 500 ns pulse width. The electric circuit was simulated by the use of an analogeu ciecuit simulator Micro Cap III, and uncertain circuit parameters and its dependence to the circuit parameter have been clarified.

Spectroscopic study of He I,388.9nm,587.6nm, 447.1-446.9nm, F-A pair, and He II, 468.6nm have been carried out and some of the plasma parameters have been measured in good agreement with each other. Typical temperature and density are 4.9eV,$1\text{x}10^{17}\text{cm}^{-3}$. The ratio of the kinetic energy stored in plasma to input energy is,

$$\frac{W_p}{W_{blum}} = \frac{n_e T_e \times 1.6\times 10^{-19} \times \pi r^2 l}{\frac{1}{2} C V^2} \fallingdotseq 11\ [\%]$$

when the charging voltage is -12kV, and helium pressure 2 Torr. The efficient plasma production with rather high temperature and density has been achieved by the compact PFN discharge.

Acknowledgement

The authors express their special gratitude to Prof. H. Matsuzawa for fruitful discussions and to T.Fujita, N.Otobe, M.Hatano and K.Miyazaki for their collaboration during the experiment.

Reference

1.R,Mewe,Brit.J.Appl.Phys.,18(1967)107

2.R.W.P. McWhirter," *Spectral Intensities*",in *Plasma diagnostic*

Techniques",R.H.Huddlestone and S.L.Leonard,ed.(Academic ,New York,1965)

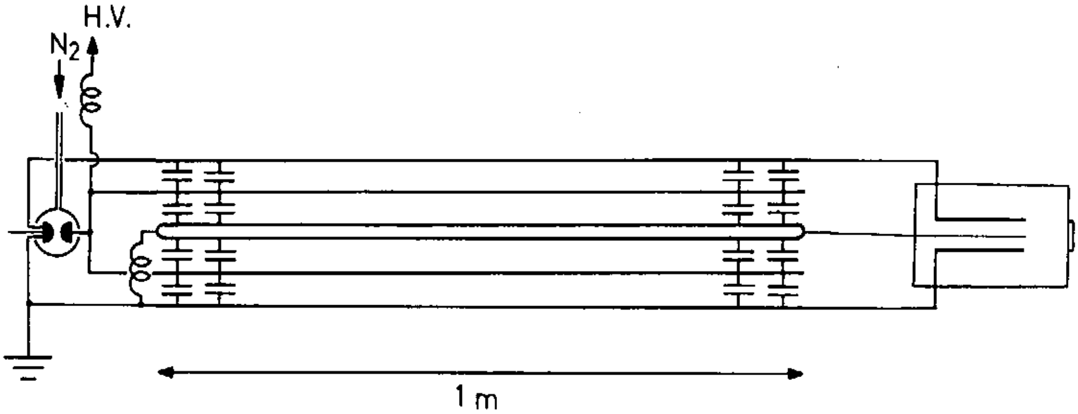

Figure 1 Experimental setup

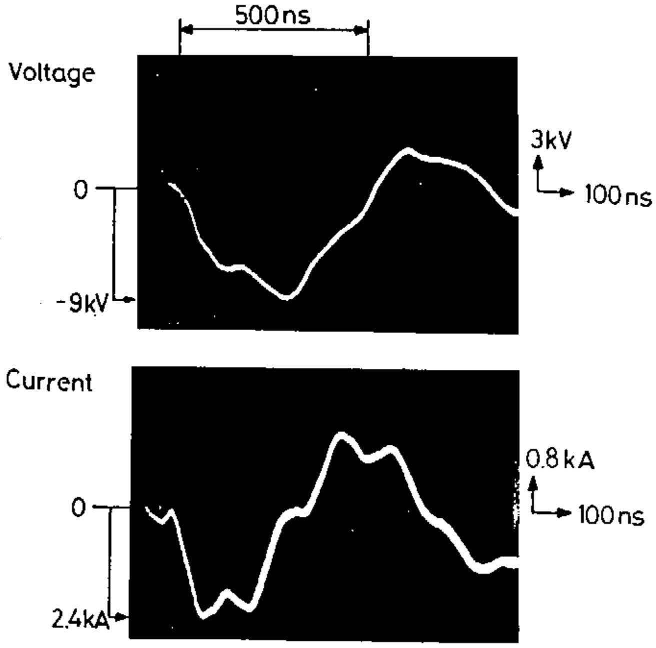

Figure 2 Output voltage and current wave form of double Blumlein PFN,V_C=9kV.

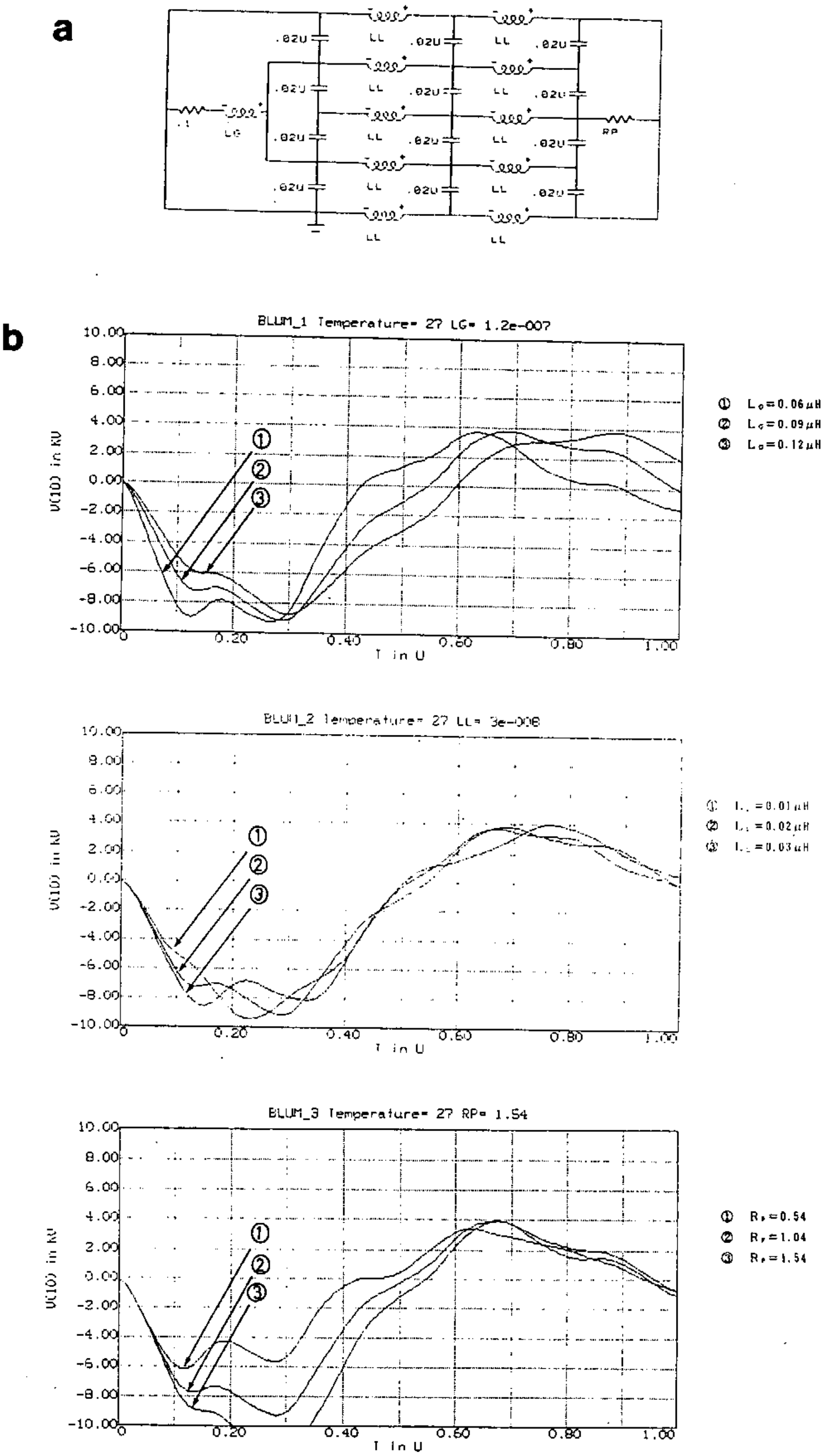

Figure 3 (a) A circuit model for PFN, (b) Voltage wave form, parameters, L_G,L_L,R_p.

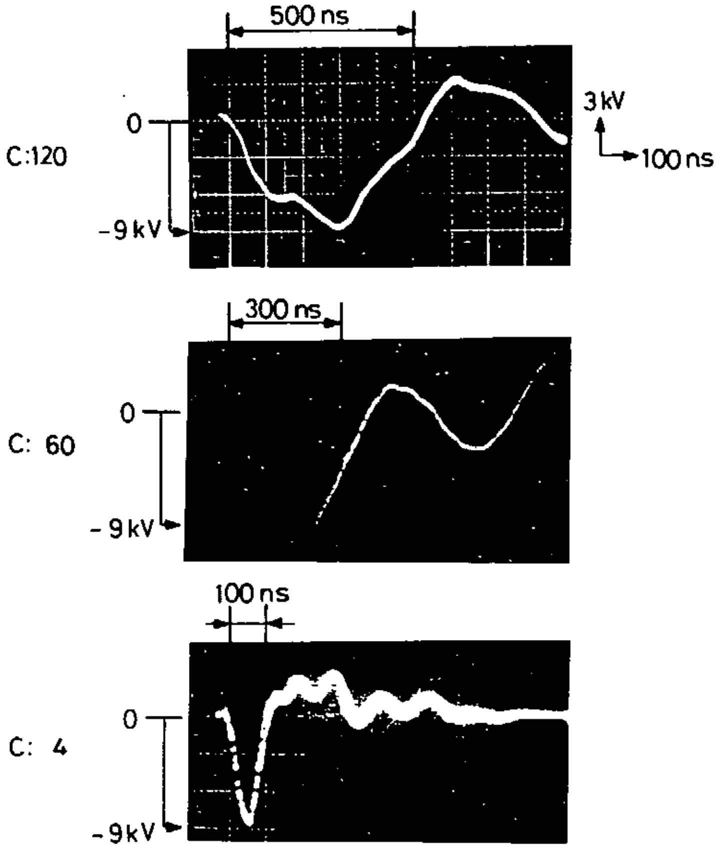

Figure 4 Output voltage wave form for different number of ceramic capacitors.

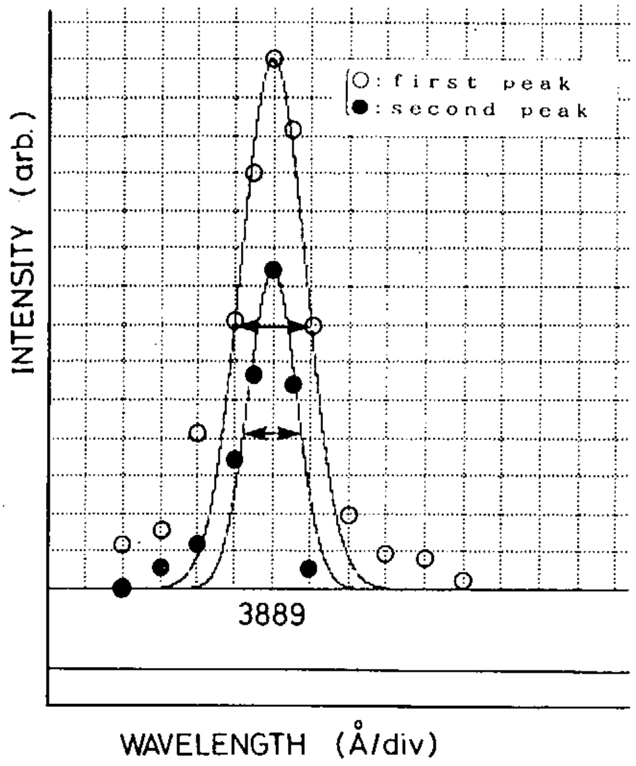

Figure.5 Stark broadening of 388.9nm, charging voltage,-12kV, helium pressure 2 Torr.

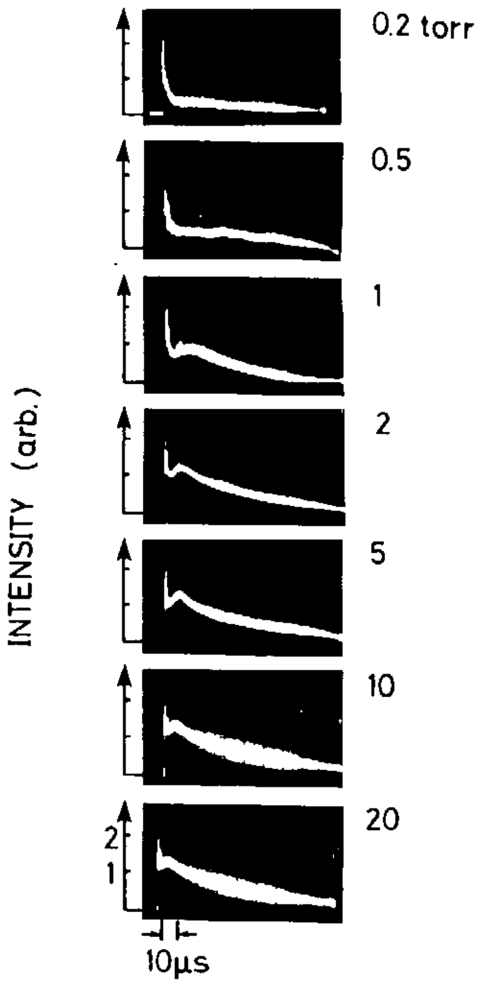

Figure 6 Temporal evolution of the intensity of 388.9nm.

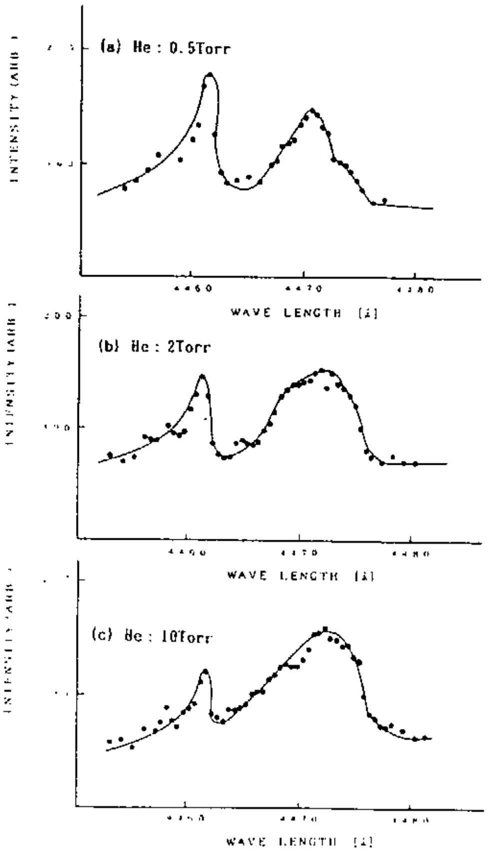

Figure 7 Stark broadening of 447.1-446.9 nm,F-A pair, charging voltage,-18kV, helium pressure 0.5,2 and 10 Torr.

Soft X-ray emission and diagnosis from fiber pinch and conductive thin film liner compression plasma

Yoshikazu Hoshina, Mamoru Kanou, Satoshi Ogura, Kazuhiko Horioka,
Kouichi Kasuya, Teruhiko Tajima*, and Shozo Ishii
Tokyo Institute of Technology
*National Institute for Fusion Science

Abstract

Dense and high energy density Z-pinch plasmas are created by two different ways and are examined experimentally. A stable plasma column has been created in a carbon fiber pinch driven by a pulsed power generator. Conductive thin film liner compression is proposed to overcome the disadvantages of metallic liner compression and gas puff Z-pinch. The dense Z-pinch plasmas are well diagnosed by X-ray measurements. X-ray diodes are used to obtain time-resolved X-ray spectrum.

§1. Introduction

Z-pinch plasmas easily creating dense and high energy density plasma open up various applications. Intense X-ray emission from Z-pinch plasma is applied to X-ray laser and intense X-ray source for semiconductor lithography. Since linear Z-pinch discharges are compact in size and simple in structure, various configurations have been proposed and investigated, namely, fiber pinch, plasma focus, metallic liner compression, gas puff Z-pinch, and gas embedded Z-pinch initiated by a laser beam. In all these experiments, efforts are made to establish a dense plasma. The dense plasma is easily created in Z-pinch plasma initiated from solid matter rather than gaseous state. If the restriction of the material to become plasma is extended from gas to solid, the degree of freedom in choosing the wavelength range of soft

X-ray emission from Z-pinch as an intense X-ray source becomes so large. In this paper, we report on X-ray emission from a fiber pinch and a thin film liner compression in which plasmas are initiated both from solid matter.

§2. Carbon fiber pinch

In fiber pinch, large current flows in the small region, having diameters of 10-100μm. A typical experiment is on the frozen deuterium fiber pinch by NRL group[1]. They have reported neutron production from the pinch. The plasma is stably confined as far as plasma current rises. However, it is troublesome to prepare the equipment for making the frozen fiber. The carbon fiber pinch, which we have studied, does not require such a complicated apparatus. Since carbon has the small atomic number and its conductivity is not so high as that of metallic wires, plasma properties have some similarities in between the carbon fiber pinch and the deuterium fiber pinch. Experimental investigations on the carbon fiber pinch are useful to understand the physics on the complicated phenomena occurring in the deuterium fiber pinch.

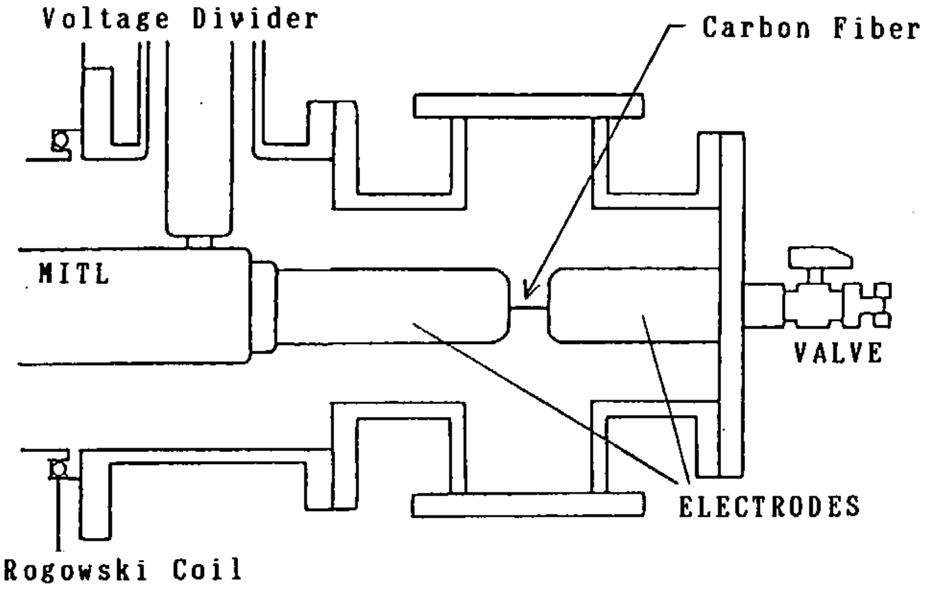

Fig.1. Carbon fiber pinch apparatus.

A carbon fiber pinch apparatus is shown schematically in Fig.1. Two types of carbon fiber are used in the experiment: a carbon fiber with and without metal coating on the surface. Copper or nickel layer of 200Å in thickness is coated on the surface of the carbon fiber of 7μm in diameter. The fiber can be placed between electrodes in a chamber without breaking a high vacuum by means of a specially designed fiber loading system. The discharge electrodes with the separation of 2cm are mounted in a coaxial geometry in the vacuum chamber which has four windows to allow measurements of X-ray and visible radiation in the radial direction.

The carbon fiber pinch has driven by the Marx-waterline generator, "LIMAY-I" installed at National Institute for Fusion Science. The stored energy is 13kJ, when the output voltage of the Marx generator is 1.6MV. The peak current of 200kA rises in about 80ns.

Temporal evolution of the pinch is diagnosed by streak photography taken through the acrylic window in the radial direction, and by conventional voltage and current measurements. X-ray emission is measured by a plastic scintillator (NE102A), which is a cylindrical shape of 3mm in diameter and 1mm in thickness. A PIN diode (Quantrad Co. 100-PIN-125) has been used as another X-ray detector. Filters of Be or Al having different thickness are mounted in front of the scintillator or the PIN diode to cut off visible light radiated from the plasma and to obtain rough estimation of radiated X-ray photon energy spectrum. An X-ray pinhole camera has been used for spatially resolved X-ray measurement. X-ray spectra in the wavelength range of 8-11Å are obtained by a flat crystal spectrograph with a KAP (Potassium Acid Phthalate) crystal[2)].

Typical waveforms of the discharge current and the X-ray emission detected by the PIN diode are shown in Fig.2. Intense

X-ray is emitted from the copper or nickel coated carbon fiber pinches. Two peaks have appeared in the X-ray signal reproducibly. The first peak has appeared during the current rising phase. At the same time, a small dip is seen in the plasma current trace. The second peak has appeared simultaneously just after the peak of current. Since the amplitude of the first peak decreases as the thickness of the filter increases, X-ray emission corresponding to the first peak comes from the high temperature plasma established in the maximum compression phase of the pinch. On the other hand, the amplitude of the second peak does not show any significant variance according to different thickness. The second peak is mainly high energy photons radiated from collisionally excited ions by high energy electrons. One plausible mechanism of electron acceleration is due to high electric field generated by the m=0 mode instability. The m=0 mode instability is observed at the current peak as seen in the visible light framing photographs. The electron temperature of the copper coated fiber pinch is about 2000eV and that of the nickel coated fiber pinch is

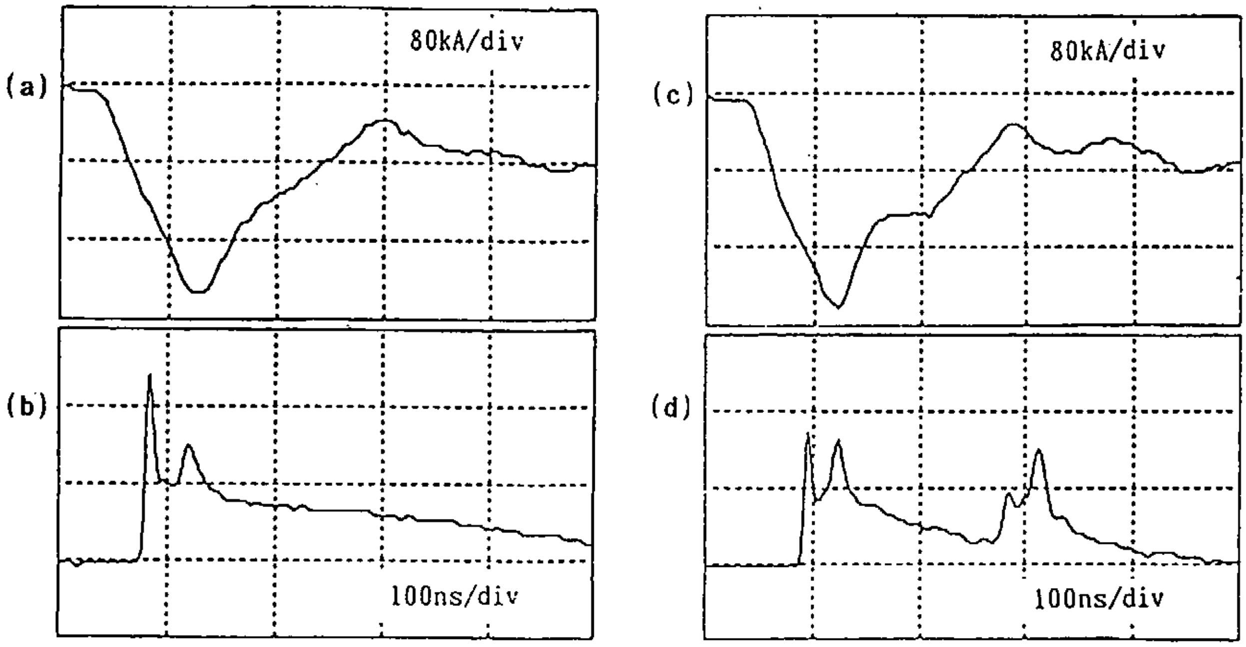

Fig.2. Copper or nickel coated carbon fiber pinch with LIMAY-I, (a) pinch current, (b) soft X-ray signal (copper coated), (c) pinch current, (d) soft X-ray signal (nickel coated).

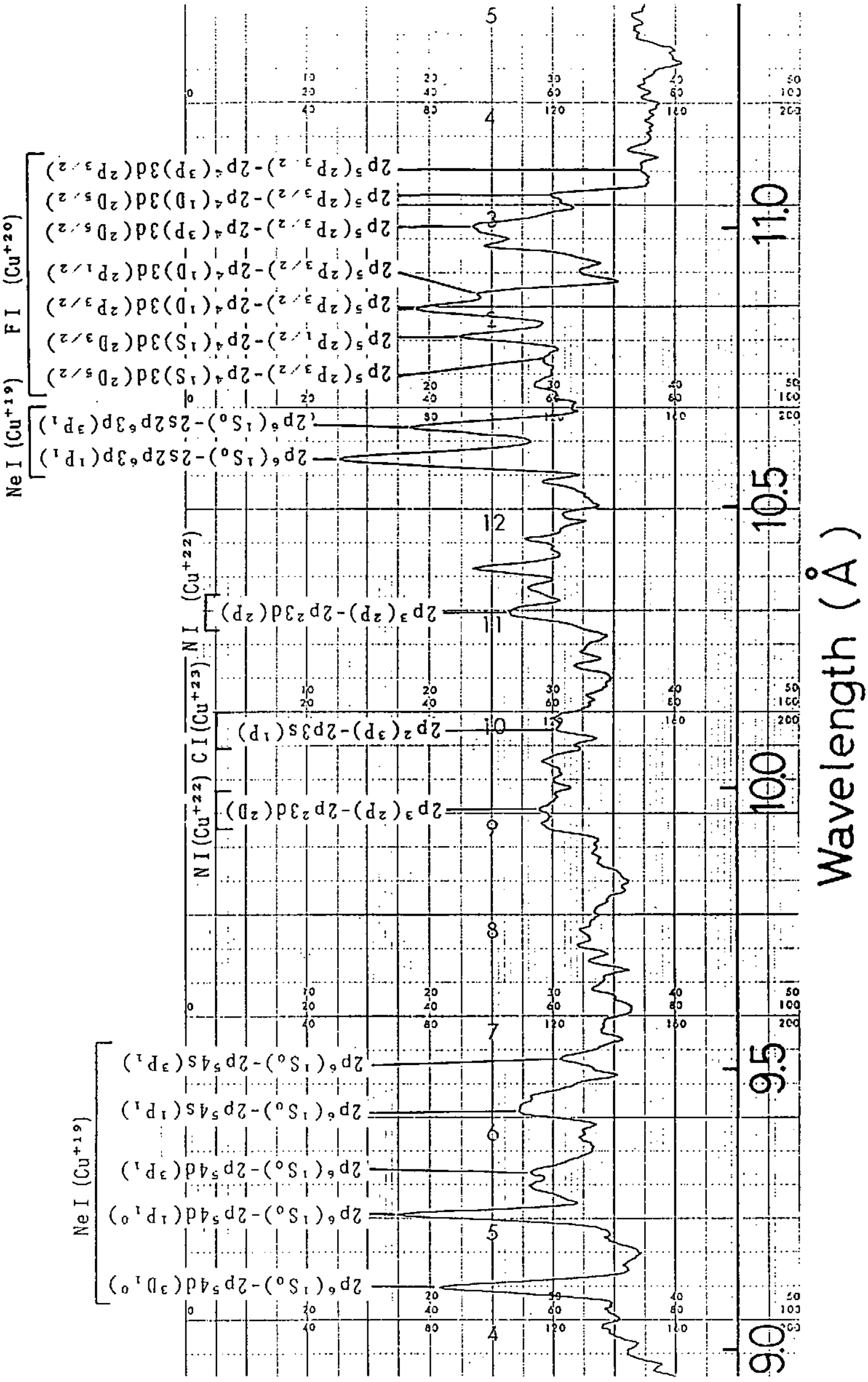

Fig.3. X-ray spectrum observed by a crystal spectrograph (copper coated carbon fiber pinch with LIMAY-I).

400eV, by evaluating from the foil absorption method. The variety of X-ray signals observed through the filters having various thicknesses have been compared with calculated results by means of hybrid atomic model (HAM)[3]. X-ray spectrum observed by a crystal spectrograph is shown in Fig.3. The line spectra of Ne-like ions and F-like ions are observed.

§3. Conductive thin film liner compression

Metallic thin foil liner compression can attain higher compressed state than gas puff Z-pinch. The implosion of metallic liner is uniform and reaches to a very small radius. This strong compression is suitable for intense pulsed soft X-ray source application and for generating high magnetic fields. However, high repetition rate operation is impossible, because it is very difficult to place a mechanically weak metallic liner between the electrodes. In case of gas puff Z-pinch, hollow cylindrical pulsed gas flow is used as the compression liner, and the operation with high repetition rate is possible. The disadvantage of the gas puff Z-pinch is that the imploding plasma layer is thicker than that of metallic liner compression and is nonuniform in the axial direction.

To overcome these problems, we propose a scheme to use a conductive thin film deposited on the inner surface of discharge tube wall as a compression liner. Strong compression can be obtained by implosion of a sub-milimeter thick plasma layer in vacuum. Imploding kinetic energy is efficiently converted to thermal and radiation energy. Since the liner can be made of any materials which become thin film, radiation from the pinched plasmas have a variety of radiation spectra. This is advantageous to soft X-ray source applications. X-ray laser pumping is also possible by this new liner compression scheme, when properly designed multi-layered liners are used.

A conductive thin film liner compression apparatus is shown schematically in Fig.4. The vacuum chamber made of stainless steel is evacuated by a oil-diffusion pump and the operating pressure is 5×10^{-5} torr. A conductive thin film liner is formed on the inner surface of an acrylic resin tube located inside the chamber. A pair of annular electrodes are placed with the separation of 4cm at both the end of the tube of 7cm in diameter. Mechanical dimension of the liner can be varied by changing the diameter of electrodes and of an acrylic resin tube. The cathode is connected directly to the vacuum chamber which works as a return conductor. There are a window above the anode in the axial direction and four windows in the radial direction viewing the tube surface. X-ray and visible radiation are detected through these windows.

The thin film liner is formed by a vacuum vapor deposition method. The evaporating source is mounted below the cathode region as shown in the figure. Evaporating materials, namely, aluminum, copper, silver, and indium are heated in a crucible, which is a alumina (aluminum oxide) coated tungsten wire.

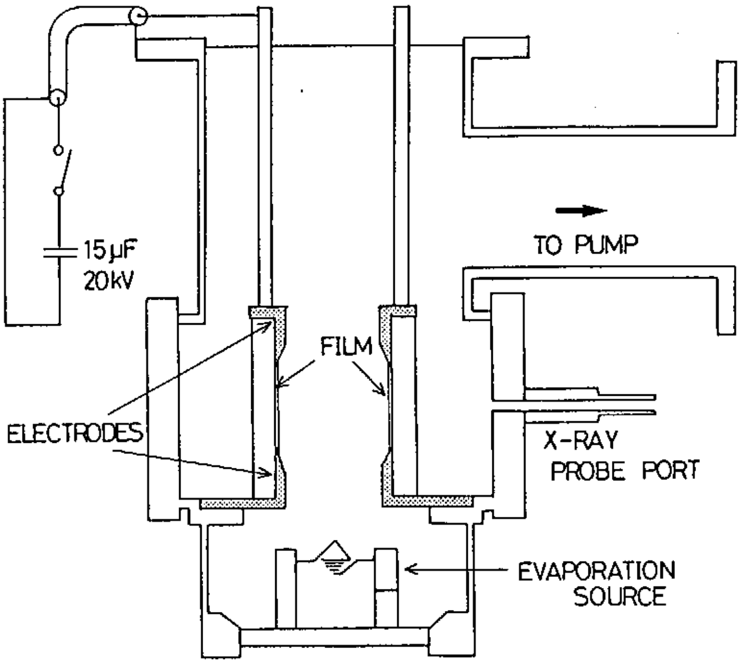

Fig.4. Conductive thin film liner compression apparatus.

The thin film metallic liner is driven by a capacitor bank with the total capacitance of 15μF. The bank consists of five capacitor units, each of which has two 1.5μF capacitors with a pressurized air-gap switch and is charged up to 20kV. The total stored energy is 3kJ.

The pinch characteristics are diagnosed by streak photography taken through the acrylic window in the radial direction, and by conventional voltage and current measurements. The X-ray emission in both the axial and the radial direction is measured by a plastic scintillator (NE102A). Beryllium filter of 15μm in thickness is mounted in front of the scintillator.

Copper is mainly used as a evaporating material throughout the experiments. The liner mass is controlled by the opening time of a shutter mounted in the upper region of the evaporating source. However, the shutter operation cannot be withstood in the high temperature environment, since the shutter is too close to the evaporating source. Therefore, we cannot obtain the data with the different mass liners. Typical waveforms of the discharge current and the X-ray emission detected by the plastic scintillator are shown in Fig.5. The peak value of the discharge current is about 195kA. The visible light in the streak photograph of radial evolution starts to appear from the time of the first peak of the current. X-ray emission is not obtained at the same time. The reason of this phenomenon is not known, but is believed to be a pre-pinch of a layer of material from the inner surface of the thin film. This pre-pinch is not related to the initial liner mass. The main pinch occurs at the second compression. At the same time, X-ray emission is obtained. This signal is not reproducible, since X-ray emission characteristics are severely related to the initial mass of liner.

We have calculated the relation of the emitted X-ray intensity to the initial liner mass. The results with a 1D-MHD model and an average-ion model are shown in Fig.6. As the initial condition, we used exponential profiles for the density and temperature in space having the peak at the tube wall. N_0 is the

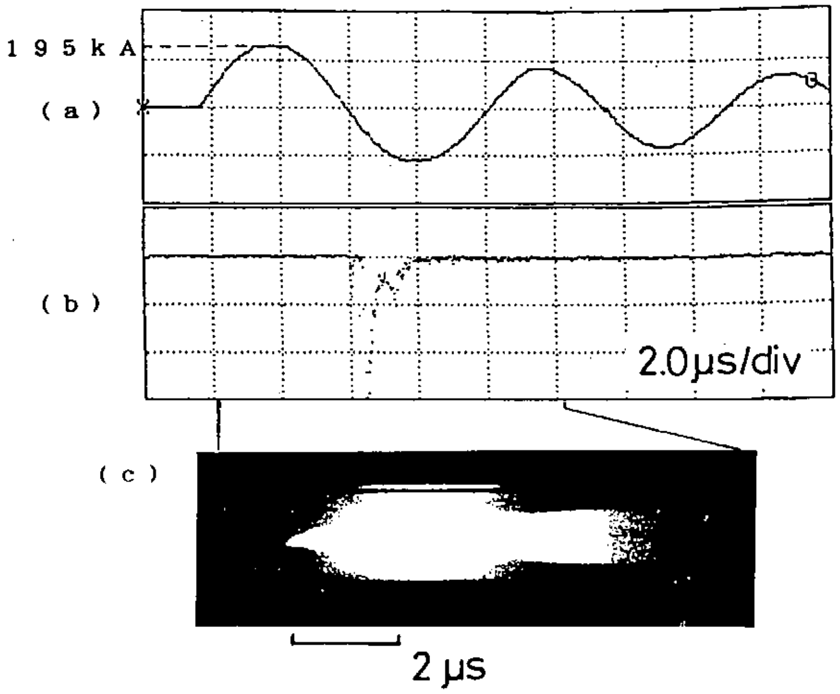

Fig.5. Conductive thin film liner compression,
(a) pinch current, (b) soft X-ray signal,
(c) streak photograph of radial profile.

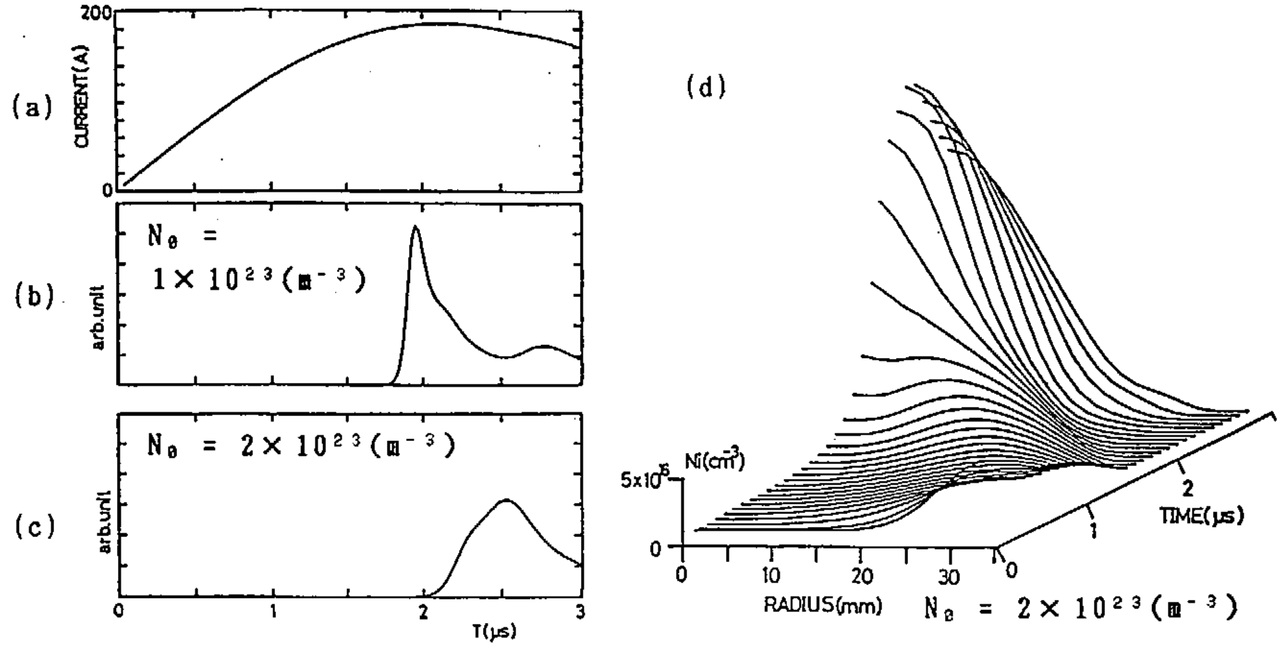

Fig.6. The results with a 1D-MHD model and an average-ion model,
(a) pinch current, (b)(c) the emission intensity,
(d) radial profile of the ion number density vs. time.

ion number density at the tube wall. The intensity and temporal profile of the emitted X-ray show a significant variance by the initial liner mass.

§ 4. X-ray diagnosis

The dense Z-pinch plasmas are well diagnosed by X-ray measurements. X-ray diode is a time-resolved detector being able to cover the wide range of photon energy[4]. The signal obtained from the X-ray diode depends on the photocathode quantum efficiency, the thickness and composition of the absorbing filter. It is possible to obtain time-resolved X-ray spectrum by using a number of diodes, each with a different spectral response. We made a set of three X-ray diodes and have tested in the measurement of vacuum spark discharge. We are investigating the deconvolution routine to obtain the X-ray spectrum.

§ 5. Conclusion

In a metal coated carbon fiber pinch, two peaks of X-ray emission have appeared. The first peak of X-ray emission comes from the high temperature plasma in the pinch, and the line spectra of Ne-like ions and F-like ions of coating metal are observed. A conductive thin film liner is a new scheme to overcome problems of conventional liner type compression experiments. This scheme is applicable to various applications.

References

1) J. D. Sethian, A. E. Robson, K. A. Gerber, and A. W. DeSilva: Phys. Rev. Lett., 59, 892 (1987).

2) K. Shimoda, T. Yamamoto, S. Takada, H. Sone and K. Hirano: Jpn. J. Appl. Phys., 26, 451 (1987).

3) M. Itoh and T. Yabe: Phys. Rev., A35, 233 (1987).

4) J. E. Bailey: "Effect of Radiation Cooling and Plasma Atomic Number on Z-pinch Dynamics" (1983).

Time resolved electron spectrum analyzer

Katsumi HIRANO, Toshikazu YAMAMOTO, Kouji ASAMI and Makoto SHINDO

Department of Electronic Engineering, Gunma University,
Kiryu, Gunma 376

Synopsis

An electron energy analyzer is designed for a time resolved measurement of pulsed energetic electron beams whose energy is in the range from 200 keV to several MeV, and successfully used to obtain energy distribution of the electron beam generated by a plasma focus device. The beam detection system is based on Cerenkov effect. The electrons are injected into an optical medium to generate the Cerenkov radiation. The radiation is detected by six photomultipliers through optical fibers at different angles which depend on the electron energy. For the optical medium lucite is employed. Energy resolution of the detector is presented as a function of the electron energy.

1 Introduction

The electron energy analyzer for the impulsive electron beam has received considerable interest in the field such as the pulse power electron source, free electron laser and the dense plasma physics. Above all, a dense plasma such as z-pinch, plasma focus and an ICF usually emits energetic electrons and ions whose energy extend up to the MeV range. Those emissions closely correlated with the plasma dynamics, and so the measurement of those emissions is important to explain the mechanism of plasma heating. For the ions time- and energy-resolved observations have been carried out.[1-3] However, in the electrons few authors considered to obtain the energy analyzed measurement with time resolving. In few papers, the energy distribution of the electron beam produced with a plasma focus was considered.[4] Recently Smith et al. proposed a magnetic energy analyzer in which a phosphor plate was used as a detector.[5] However, those analyzers were not able to make a time resolved measurement.

In this paper, we intend to construct a time resolved electron energy spectrometer based on the Cerenkov radiation. In many cases, the magnetic analyzers have been employed to obtain the energy spectra with developing various detectors. In several experiment, the Cerenkov detector was used for detection of the energetic electrons without energy analysis.[6-8]

The Cerenkov effect in an optical medium allows a determination of the energy spectrum of charged particles incident into the medium. The effect involves that radiation is emitted by the medium under the action of the electric field of the electrons moving in the medium, when the velocity of the particles are higher than that of light in that medium. Like the shock wave in air, the wave front of the Cerenkov radiation conically propagates with respect to the direction of the incident electrons. The direction of the propagation is forward at an angle θ_c, Cerenkov angle, from the direction of the electron, where θ_c is given by the relation,

$$\cos\theta_c = 1/\{n(\lambda)\beta\} \qquad (1)$$

here $n(\lambda)$ is the refraction index of the medium as a function of the wavelength and $\beta = v/c$, where c and v are the velocity of light in vacuum and the incident electrons, respectively.

For the relativistic electrons, the kinetic energy is described by θ_c as following;

$$T = m_0c^2\{1/[1 - 1/\{n(\lambda)\cos\theta_c\}^2]^{1/2} - 1\} \qquad (2)$$

where m_0 is the rest mass of the electron. The relationship between T and θ_c is shown in Fig. 1.

It should be noted that the intensity of the Cerenkov radiation has an angular distribution which is proportional to $\sin^2\theta_c$.[9]

2 Experimental

2-1 Detection system

In this experiment, a semi-circular lucite (Mitsubishi Rayon #001) plate whose radius and thickness are 100mm and 10 mm is used for the optical medium. The schematic diagram of the detection system is shown in Fig. 2. The index of the refraction is given by the manufacturer as a function of the wavelength.[10]

The electron beam is incident into the medium after being collimated by a pinhole of 1 mm in radius. The Cerenkov radiation is detected at the six angles by six photomultiplier tubes (Hamamatsu Photonics H1161) through the slit systems and optical fibers mounted along the circumference of the medium. The slit system consists of two slit of 0.5 mm in width whose distance is 50 mm.

The Cerenkov radiation propagates to the conical direction in the semi-circular optical medium. The radiation which is directed to the faces of the medium plate is reflected on the face as shown in Fig. 3. The slit system is designed so as to accept only the radiation which propagates along the generation line of θ_c.

The Cerenkov angles are determined as the function described in eq. (1). The system is shielded by lead plate and pipes of 3 mm in thickness from the scattered X-rays. Signals from the system are displayed on the six channel digitizing scope (HP 16500A) and memoryed by a personal computer (NEC PC-9801RA2). The frequency response of the system was 100 MHz.

Energy- and sensitivity calibration of the system should be performed using an appropriate electron source. Althouth a source ranging from 200 KeV to several Mev is most accurate one, it requires an electron accelerator which is sometimes unavailable. Because of the difficulty, we used a method to calculate the relationship of the electron energy and the Cerenkov angle instead of the energy calibration. For sensitivity, we could not help doing with relative unit for the energy distribution function to be obtained.

2-2 Sensitivity of the spectrometer

The angular distribution of the Cerenkov radiation and the spectral absorption coefficient of lucite[10] were taken into account for relative sensitivity. Moreover, the intensity of the Cerenkov radiation which is accepted by the detection system is inversely proportional to the length of the generation line of the cone formed by the Cerenkov angle. This means that the amplitude of the signal at θ_c should be corrected to divide it by sin θ_c. Then, the relative intensity of the system $I \propto \sin^2 \theta_c \cdot (1/\sin \theta_c)$. The relationship between the electron energy and the relative intensity is shown in Fig. 4.

2-3 Energy loss of the incident electrons

The incident electrons loss their energy by various interactions with the medium. When the losses are not negligible, Cerenkov radiation detected at θ_c does not correspond to the electron energy before injection into the medium. For the correction, it will be sufficient if we consider the losses that are normally taken into account for calculation of the electron range in the medium and the loss concerning the Cerenkov radiation itself. Namely, they consist of,

1) energy loss with the Cerenkov radiation, $(dT/dx)_{cer}$ [11]
2) Collision loss with orbital electrons in the medium materials, $(dT/dx)_{coll}$. [12] However, the collision loss is reduced by the density effect of the material. The reduction rate of the collision loss Δ_p is given in ref. 13.
3) loss with Bremsstrahlung, $(dT/dx)_{rad}$ [14]

where x is direction to that of the incident electrons. Therefore, total energy loss of the incident electrons, T_e which is given as

$$T_\ell = \int_0^\ell \left\{ \left(\frac{dT}{dx}\right)_{coll} - \Delta_p + \left(\frac{dT}{dx}\right)_{rad} + \left(\frac{dT}{dx}\right)_{cer} \right\} dx \tag{3}$$

where ℓ is the length that the electrons emit the Cerenkov radiation in the medium discussed in 2-4.

It was found that the Cerenkov loss was negligibly small in the energy region which was expected in this experiment. Therefore, we made the correction of electron energy taking losses, 2) and 3) into account. Calculated results for each loss are shown in Fig. 5 as functions of the electron energy.

2-4 Energy resolution

A schematic diagram showing a relation between the Cerenkov angle and the detection system is illustrated in Fig. 6. The electron beam whose radius is r, is incident into the medium and the system detects the Cerenkov radiation emitted for the length ℓ, as mentioned above. The slit widths of S_1 and S_2 are d_1 and d_2, respectively. The distance of the slits is L.

Elecrons whose kinetic energy are T, emit the Cerenkov radiation in the direction θ_c. However, the radiation emitted in θ_1 and θ_2 is accepted by the system through the slits, S_1 and S_2, of finite width. This brings an ambiguity in determination of electron energy. Those angles are given as

$$\tan \theta_1 = \frac{(R + L) \sin \theta_c + (d_2/2) \cos \theta_c - r}{(R + L) \cos \theta_c - (d_2/2) \sin \theta_c - \ell} \tag{4}$$

$$\tan \theta_2 = \frac{(R + L) \sin \theta_c - (d_2/2) \cos \theta_c - r}{(R + L) \cos \theta_c + (d_2/2) \sin \theta_c} \tag{5}$$

$$\ell = (R \tan \theta_s + \frac{d_1}{2})(\sin \theta_c + \frac{\cos \theta_c}{\tan \theta_1}) + \frac{r}{\tan \theta_1} \tag{6}$$

Namely, we observe the electron energy between T_1 and T_2 through the slits S_1 and S_2. The incident electrons loss their energy by T_1 during they penetrate into the length ℓ. The energy loss can not be ignored with compare to the incident energy, especially in low energy region. The kinetic energy of the electrons T_c, T_1 and T_2 corresponding to θ_c, θ_1 and θ_2 can be calculated using eq. (2) taking the energy loss into account. Here, we define the energy resolution, R as

$$R \equiv \Delta T/T = (T_1 + T_\ell - T_2)/T_c. \tag{7}$$

The calculated result is shown in Fig. 7. It is clear that R increases in the lower energy region because a small θ_c brings a larger ℓ, then ΔT becomes larger. In the higher energy region, a larger R is caused by a small increasing rate of $d\theta_c/dT$ as shown in Fig. 1. Improvement of the energy resolution is possible optimizing the slit width and the slit distance.

The spectral response of the detector system, covers a certain range of wavelength of the Cerenkov radiation. This means that β, namely T changes between the upper and the lower limit of the spectral response according to eq. (1). However, it was found that the effect was much smaller than that by eq. (7) in the experimental region.

2-5 Plasma focus as the electron beam generator

A Mather type plasma focus device was employed to examine the performance of the spectrometer. The coaxial electrodes were 35 and 80 mm, respectively. The length of the electrodes was 80 mm. The condenser bank consisted of 4 x 1.06 μF, 100 kV capacitors. The device was operated at the bank voltage of 60 kV and at an embedded gas pressure of 6 Torr H_2. The electron beam is emitted in the upstream direction the discharge current. Hard X-rays were observed by a scintillation detector at 5 m from the focus plasma and 90° from the electrode axis. Details of the focus device are described in the previous publication.[15]

3 Performance of the spectroanalyzer

It was confirmed when the incident electron beam to the optical medium was cut by a magnet with suitable magnetic field, no signals were obtained from the six detection systems. Moreover, at the angles of $\theta = 0$ and $\theta > \cos^{-1}1/(n\beta) \sim 48°$ any signals were not detected.

Typical examples of the Cerenkov signal for each electron energy and the streak photograph are shown in Fig. 8. It is recognized that the Cerenkov signals appear at the same time which is immediately after the maximum compression of the plasma. The FWHM's of the signals is 8 ns approximately. Normally, the pinched plasma is stably sustained for ~15 ns. This almost agrees with Choi et al. though they measured electrons whose energy was less than 200 keV.[7]

Since the hard X-rays appears with the disruption, it is understood that the X-rays are ascribed to impinging of such high-energy electrons on the structure made of metals.

Figure 9 shows a typical energy spectrogram obtained from the energy analyzed electron signals shown in Fig. 8. The peak energy is nearly at 500 keV, and electrons in the high-energy tail decrease monotonically. At the high-energy tail, the distribution obviously extends up to higher than 1 MeV.

Although the result demonstrated in Fig. 9 is quite different from those carried out by Stygar et al.,4) it is almost similar to our previous experiment which is a time integrated one.8) Stygar et al. reported on the electron beam whose energies distributed from nearly 20 keV to 500 keV by using a magnetic analyzer in which Faraday cups were used as detectors. In their case, the energy spectrum of the electrons produced with a plasma focus obeyed a power law: $dN/dE \propto E^{-(3.5\pm0.5)}$. The acceleration mechanism remained unexplained in this experiment. Further investigation should be continued.

In summary, an electron energy spectrometer which is based on Cerenkov effect was developed and examined by the electron beam generated in the plasma focus. Main results are as follows,

1) Time resolved energy spectrum of electron beam was obtained.
2) Timing of the beam generation was able to determine for pulsed electron source.
3) The spectrometer can be used to investigate the electron acceleration mechanism with conducting a simultaneous observation with the plasma behavior.
4) It is possible to improve the energy resolution by optimizing the slit width, the slit distance and aperture radius for incident electrons.

References

1) K. Hirano, T. Yamamoto, Y. Okabe and K. Hirano: Rev. Sci. Instrum. 58 (1987) 20.

2) A. Mozer, M. Sadowski, H. Herold and H. Schmidt: J. Appl. Phys. 53 (1982) 2959.

3) G. Gerdin, W. Stygar and F. Venneri J. Appl. Phys. 55 (1981) 3269.

4) W. Stygar, G. Gerdin, F. Venneri and J. Mandrekas: Nucl. Fusion 22 (1982) 1161.

5) J. R. Smith, C. M. Luo, M. J. Rhee and R. F. Schneider: Phys. Fluids 28 (1985) 2305.

6) W. Neff, H. Krompholz, F. Rühl, K. Schönbach and G. Herziger: Phys. Lett. 79A (1980) 165

7) P. Choi, C. Deeney and C. S. Wong: Phys. Lett. A 128 (1988) 80.

8) K. Hirano, I. Kaneko, K. Shimoda and T. Yamamoto : Jpn. J. Appl. Phys. 29 (1990) 1182.

9) J. Marshall: Phys. Rev. 86 (1952) 685

10) Technical Handbook for Shinko Lite-A, Mitsubishi Rayon Co., Ltd. (1990).

11) R. M. Sternheimer: Methods of Experimental Physics, eds, L. C. L. Yuan and C. Wu (Academic, New York, 1961) Vol. 5A, p. 8.

12) R. D. Birkhoff: Handbuch der Physik (Splinger, Berlin, 1958) Vol. 34, p.63.

13) E. Fermi: Phys. Rev. 57 (1940) 485.

14) H. A. Bethe and J. Ashkin: Experimental Nuclear Physics, ed. E. Segre (John Wiley & Sons, New York, 1953) Vol. I, p. 266.

15) K. Hirano, T. Yamamoto, K. Shimoda and H. Nakajima: J. Phys. Soc. Jpn. 58 (1989) 3591

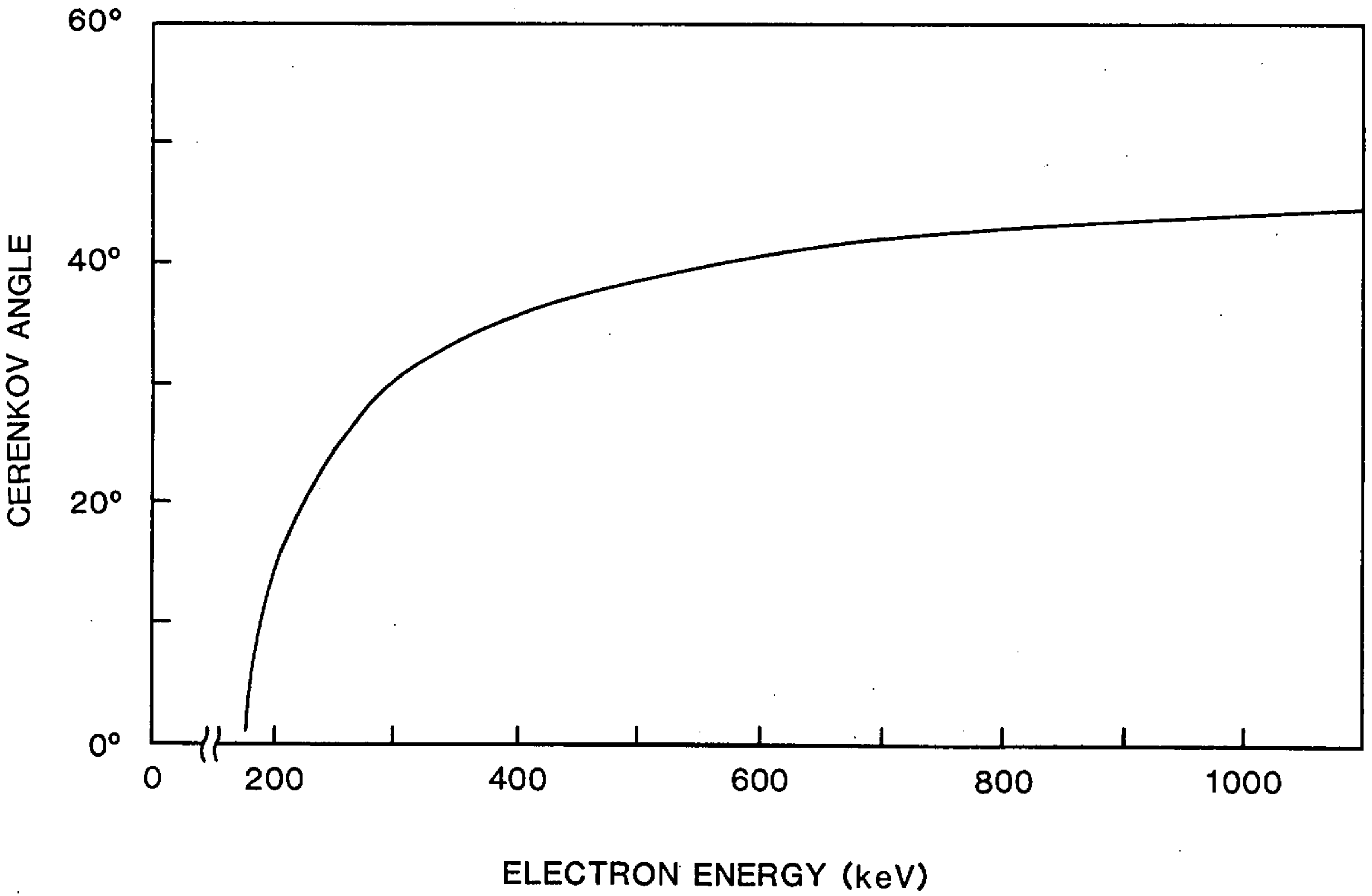

Fig.1 Relationship between incident electron energy T and the Cerenkov angle θ_c.

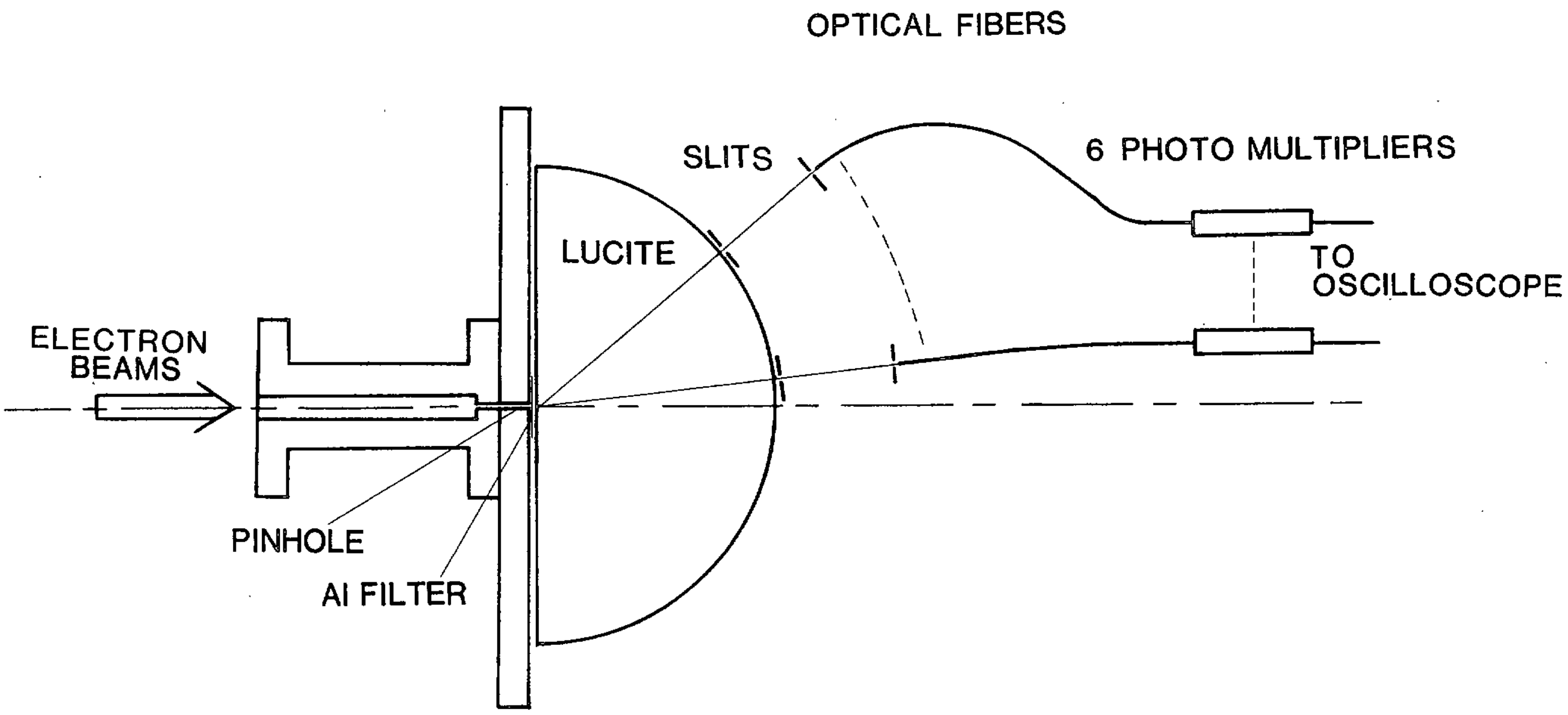

Fig.2 A schematic diagram of Cerenkov electron spectrometer.

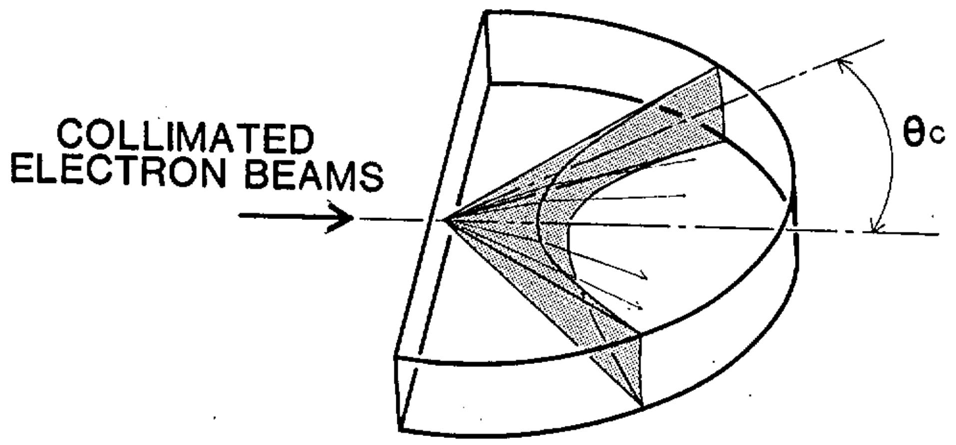

Fig.3 Pencile of Cerenkov radiation in a lucite plate.

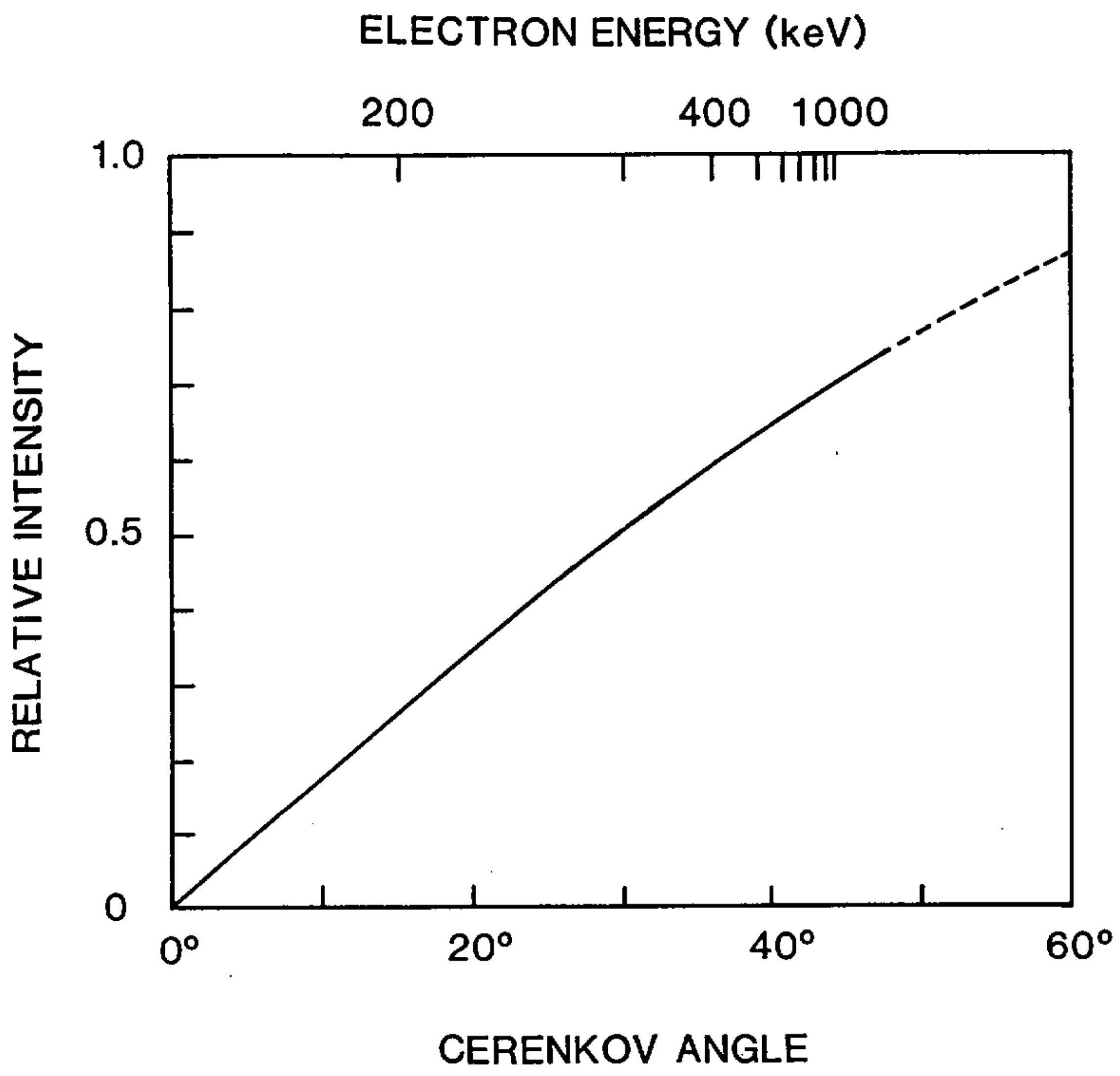

Fig.4 Relationship between incident electron energy and relative sensitivity of the Cerenkov electron spectrometer.

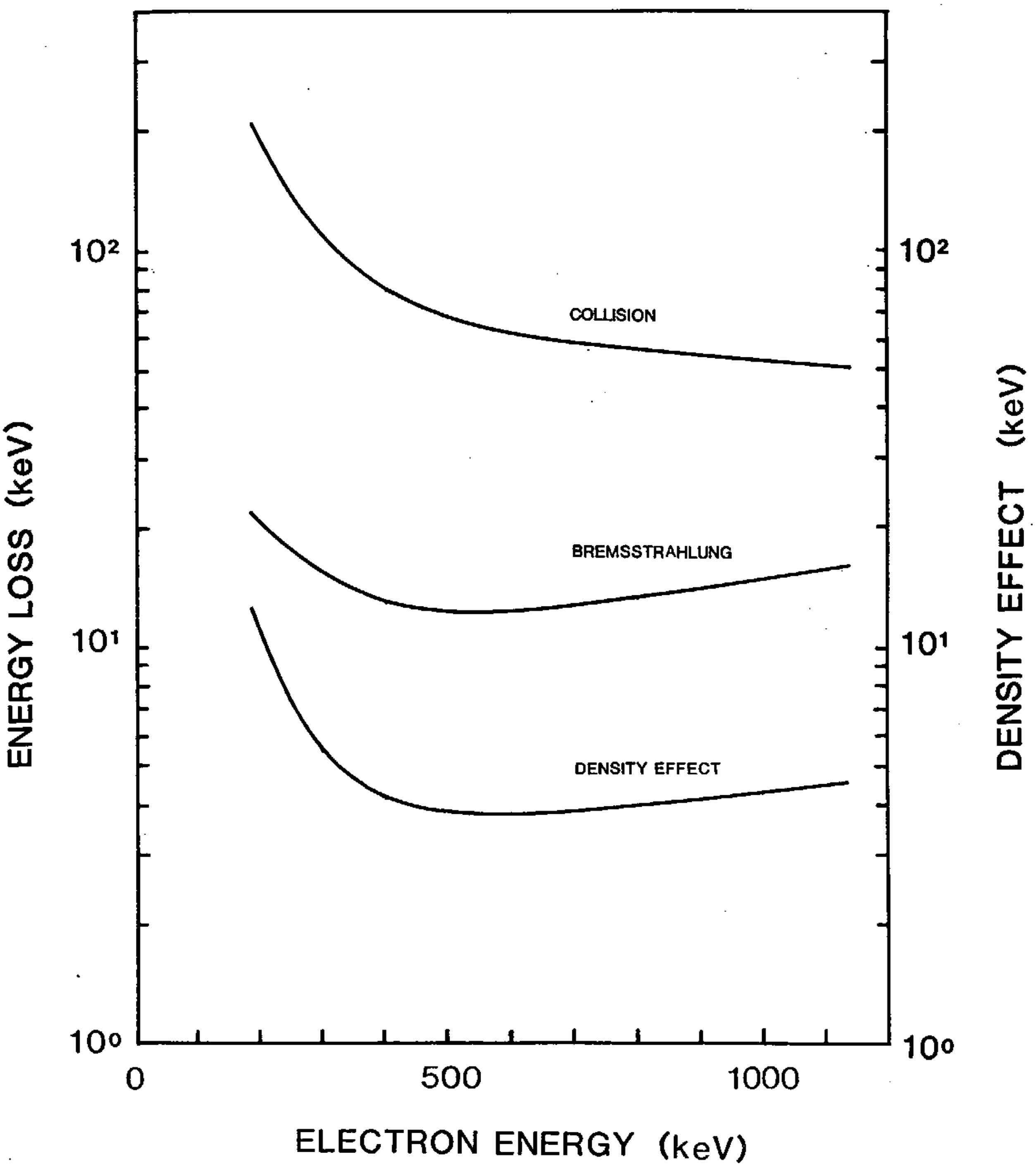

Fig.5 Energy losses of incident electrons in lucite (Mitsubishi Rayon #001).

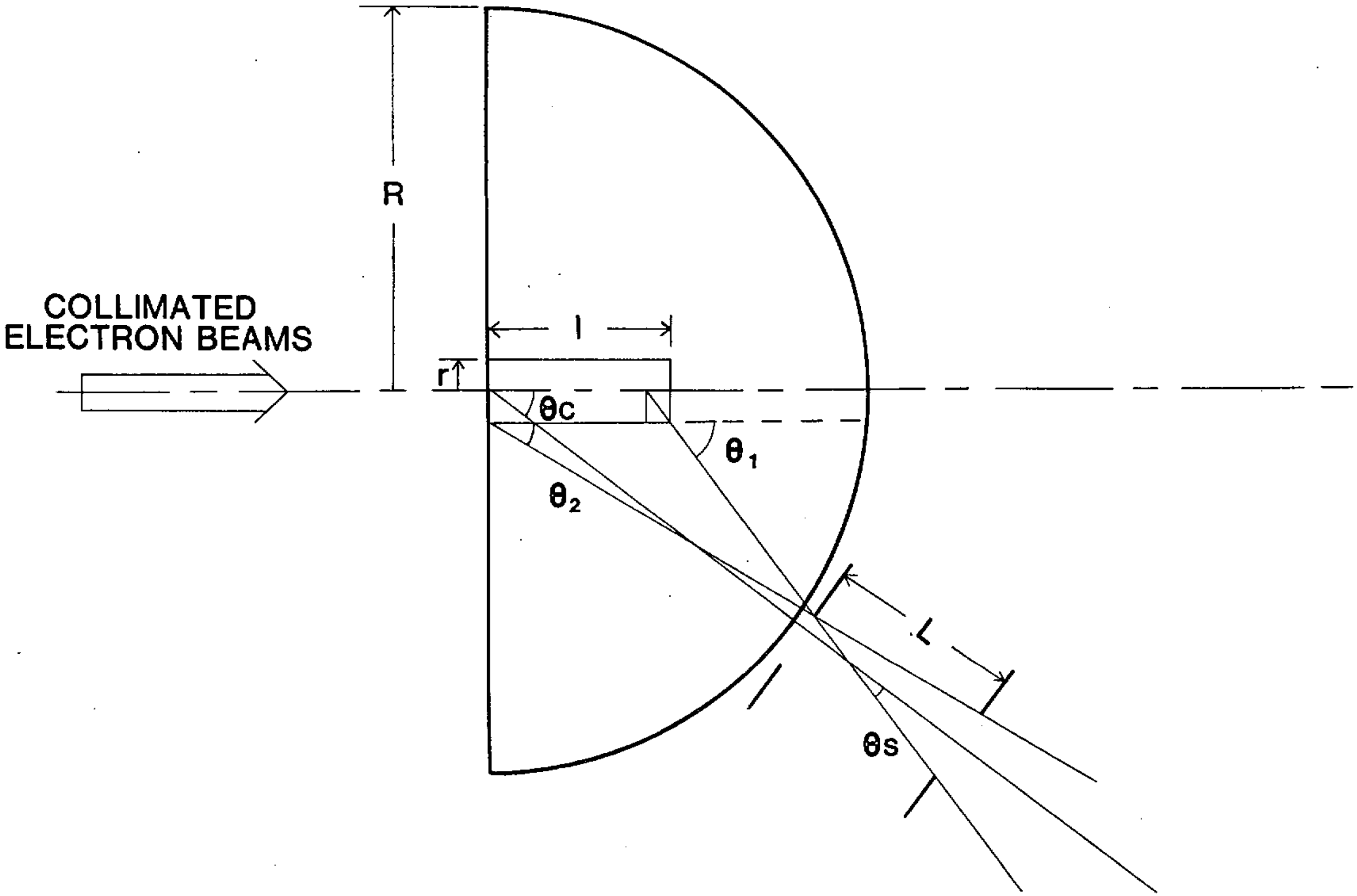

Fig.6 Schematic drawing showing the arrangement of the Cerenkov electron energy spectrometer.

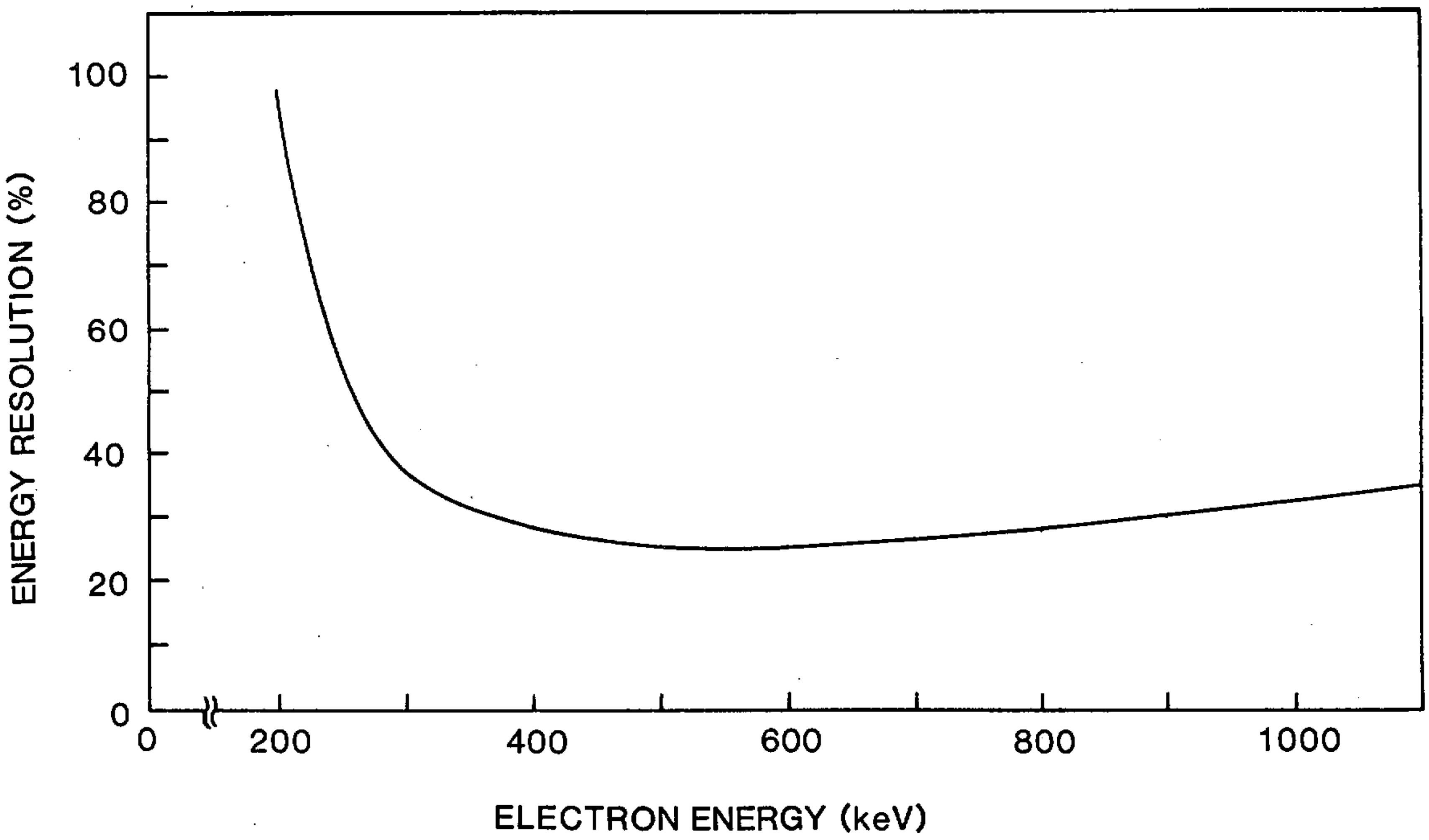

Fig.7 Energy resolution of the Cerenkov electron enegy spectrometer.

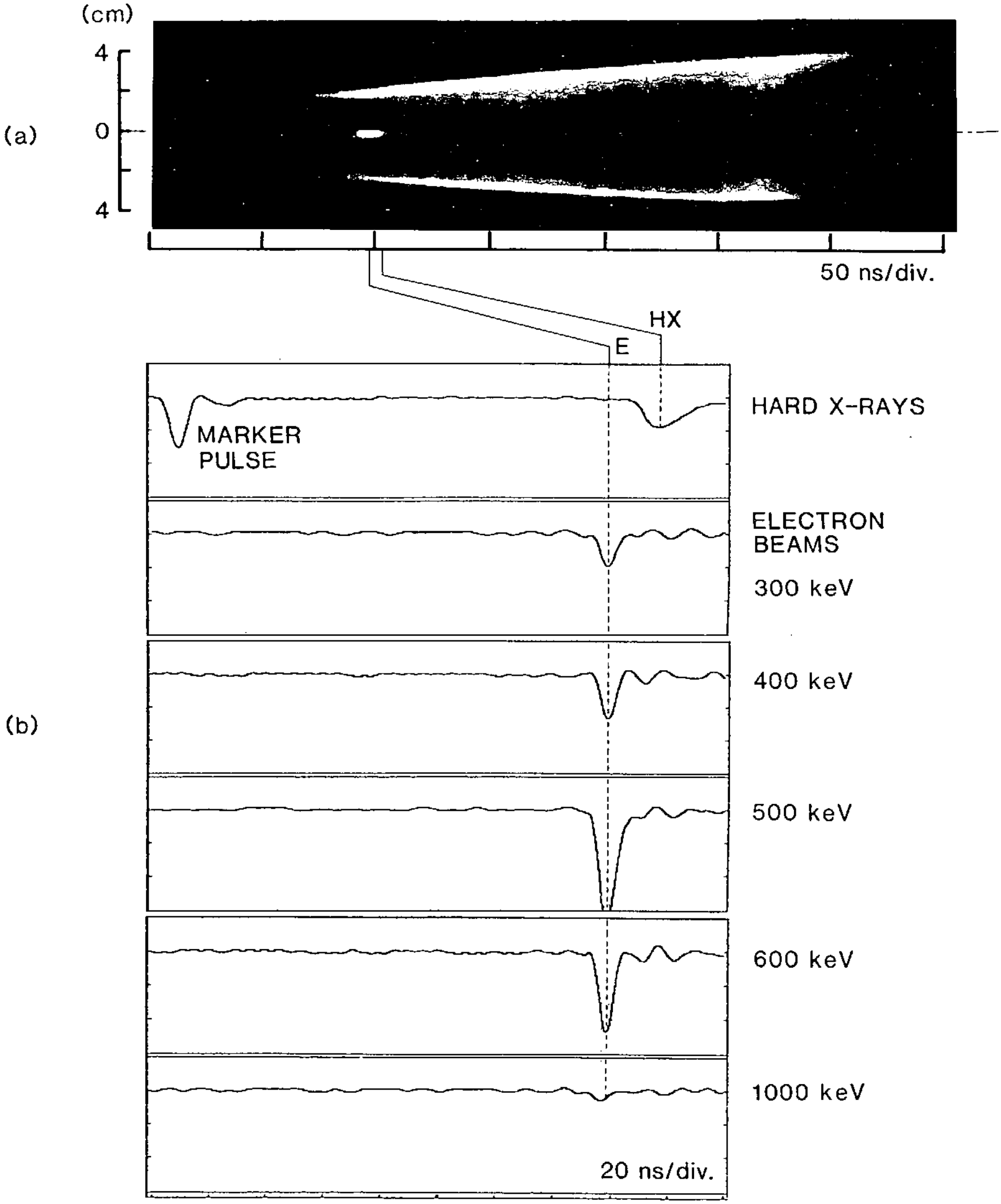

Fig.8 Typical example of streak photograph (a) and the energy anlyzed electron signals (b). The symbols E and HX represent the peaks of electron beams and hard X-rays.

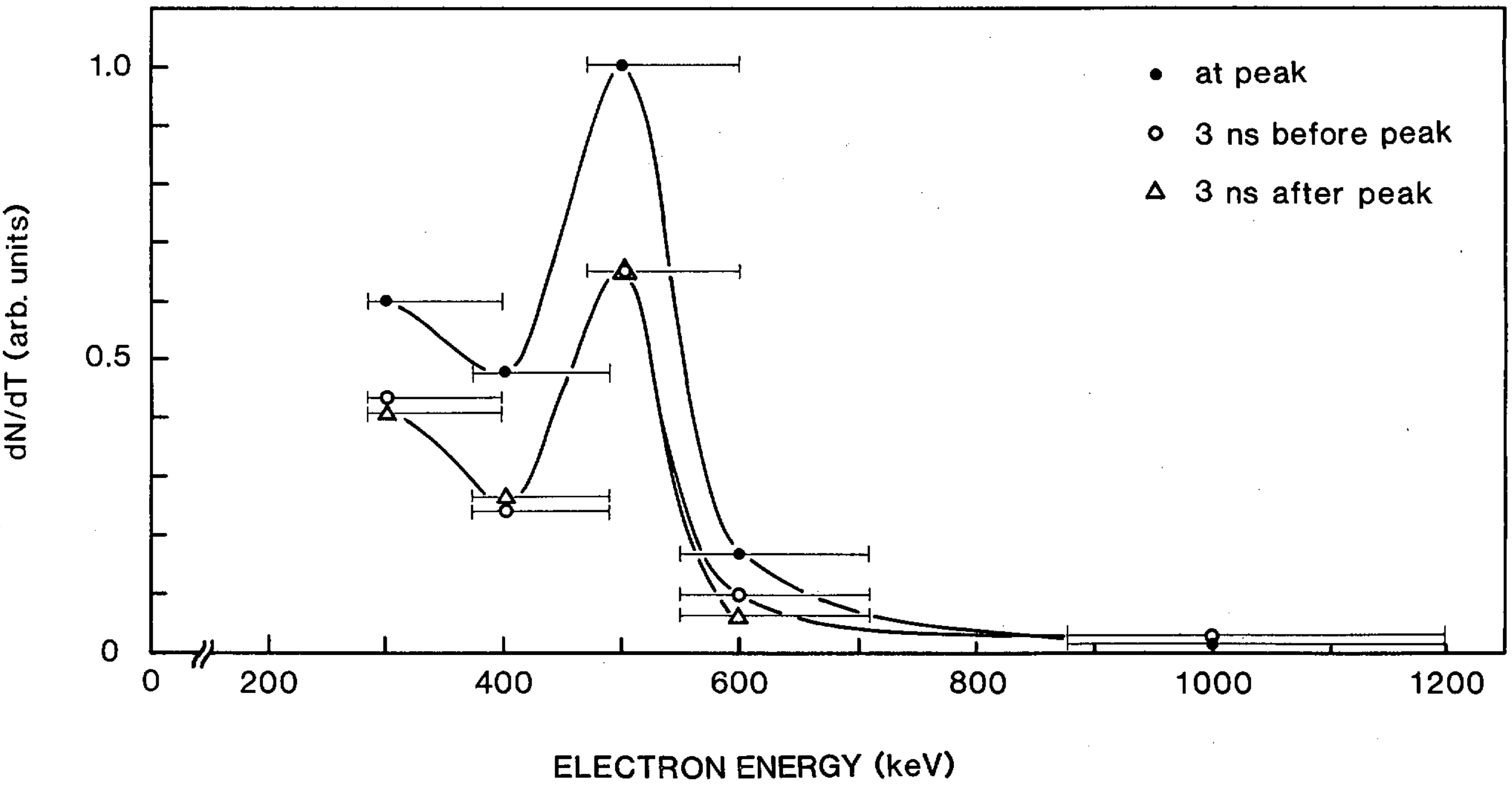

Fig.9 An example of energy spectrogram obtained from the energy analyzed electron signals shown in Fig. 8.

ENERGY CONVERTER FROM LASER ENERGY TO ELECTRICITY USING PLASMA AS A MEDIUM

THE SEPARATION OF IONS BY THE MAGNETIC FIELD

Yoshihiko KATO, Kenichi SATO, Keiji NAKAMURA,
Chobei YAMABE and Kenji HORII*
Department of Electrical Engineering, Nagoya University,
Nagoya, Aichi 464-01
*Toyota College of Technology

Abstract

In a energy converter from laser energy to electricity using plasma as a medium, it is reported here about the influence of the coarse of the mesh in the converter and about the increase of the conversion efficiency from plasma's kinetic energy to electricity using the plural ion collectors system [1).

§ 1. Principle of the energy conversion system

The diagram of the energy conversion system is shown in Fig.1. A TEA-CO_2 laser with a wavelength of 10.6 μm is used to generate plasma from the carbon target in vacuum chamber. The laser-produced plasma propagates into the energy converter called as PDC(Plasma Direct Converter). There are both ions and electrons in the plasma and each velocity is almost equal. Then plasma's kinetic energy is nearly equal to ion's because an ion is much heavier than an electron. When the plasma passes in magnetic field, the ions are separated from the plasma because electrons undergo more influence by magnetic field than ions. Therefore ions are collected by ion collector and ion's kinetic energy is converted to electricity. The converted electricity Wc, which is the PDC output energy, is calculated by the following equation,

$$Wc = Vc \times Icmean \times tc,$$

where Vc is the voltage applied on the ion collector, Icmean is the mean current on the ion collector and tc is the duration of the current. The typical magnetic flux density at the middle of the magnet is about 20 mT.

§ 2. The coarse of the mesh

§ 2-1 Experimental procedure

The value ℓ , defined as the distance between the metallic wires of the mesh, represents the coarse of the mesh used as an earth grid. When ℓ is large, the electric field between the earth grid and the ion collector is not perfectly shielded by the earth grid. Then the electric field undergoes a bad influence to the separation of ions. The other way, when ℓ is small, the geometrical transmission coefficient of the mesh decreases and the PDC output energy Wc also decreases. So, Wc is measured with the changes of ℓ and D as shown in Fig.2, where D is the distance between magnets and earth grid.

§ 2-2 Experimental result

Fig.3 shows the relationship between ℓ and Wc as a parameter D. Wc decreases with the increase of D because the ions cannot reach the ion collector on account of curving of the ions by the magnetic field. When ℓ is larger than 0.8mm, Wc decreases. This is because the electric field by ion collector voltage is imperfectly shielded by the earth grid. Therefore ℓ must be less than 0.8mm in this system.

§ 3. Increase of PDC output energy by using plural ion collectors system

§ 3-1 Experimental procedure

The conversion efficiency from ion's kinetic energy to electricity becomes largest when the voltage corresponding to the ion's energy is applied on the converter. Therefore it is difficult to increase the conversion efficiency using single collector system because the velocity of the ions in the laser-produced plasma is distributed in the range of $10^4 \sim 10^5$ m/s. While the plasma passes in the magnetic field, not only the ions are separated from the plasma, but also the track of the ion is changed according to the Larmor radius of the ion [2]. Therefore it is here tried to collect the ions by the plural collectors according to the ion's velocity. The ion collectors are put as shown Fig.4 and Wc in each collector is measured. Furthermore the angle θ of the ion collector B is defined as shown in Fig.4, and the dependence of θ on Wc is investigated.

§ 3-2 Experimental result

The PDC output energy in the collectors A and B are shown in Table 1. It is found that the maximum value of Wc is obtained increases when two ion collectors are used and each ion collector's voltage are optimized. The energy Wc is shown in Fig.5 as a function of θ.. It is found that Wc has a maximum value when θ is about 25°. At all, the maximum energy conversion efficiency of 24% are obtained under the best conditions of Vc and θ .

Next, it is examined how the ion collectors is disposed in order to make the efficiency from plasma's kinetic energy to electricity 50%. The conversion efficiency of 50% may be obtained if the ion collectors are put as shown in Fig.6, and the size of such a PDC is estimated to be about 2m.

§ 4. Conclusion

1. A fine mesh must be used for the earth grid to shield electric field by ion collector voltage.
2. The conversion efficiency is increased by plural ion collectors system. But the apparatus may be larger in order to increase the efficiency.

References

1) Y.Kato et.al:Annual Meeting of Tokai Chapter,IEE,Japan No.61(1990)

2) Y.Kato et.al:Papers of Technical Meeting on Plasma and Discharge,IEE,Japan EP-90-73,ED-90-92 (1990)

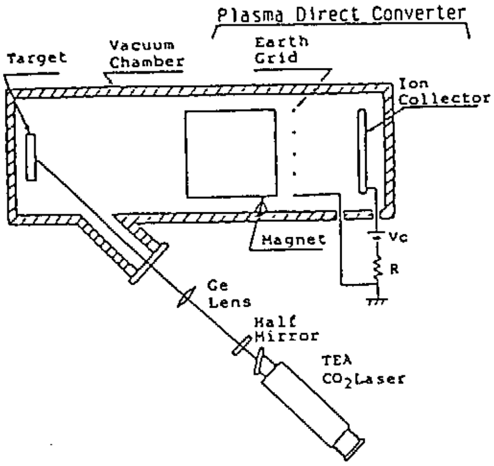

Fig.1. Energy conversion system

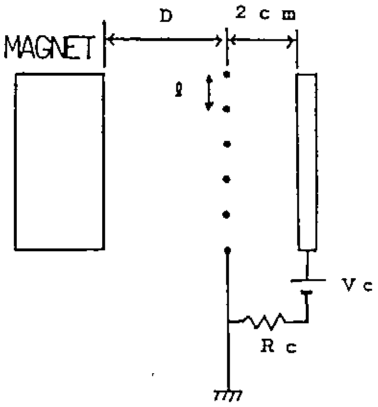

Fig.2. The coarse of the mesh

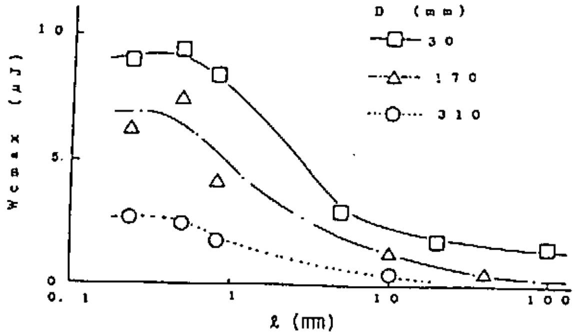

Fig.3. Characteristic of ℓ -Wcmax

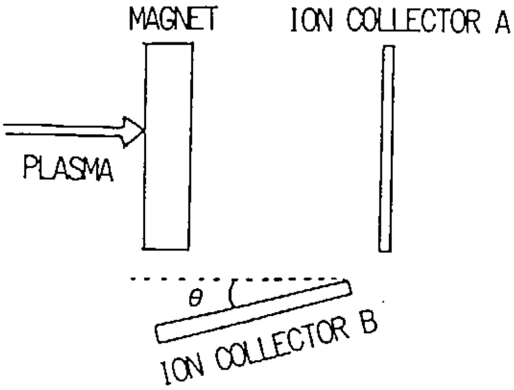

Fig.4. Two ion collectors system

Table 1. PDC output energy

ION COLLECTOR	Wc (μJ)	Vc (V)
A	5. 6	67
B	0. 7	10
A + B	6. 3	A 57 B 10
A + B	5. 6	A, B 57

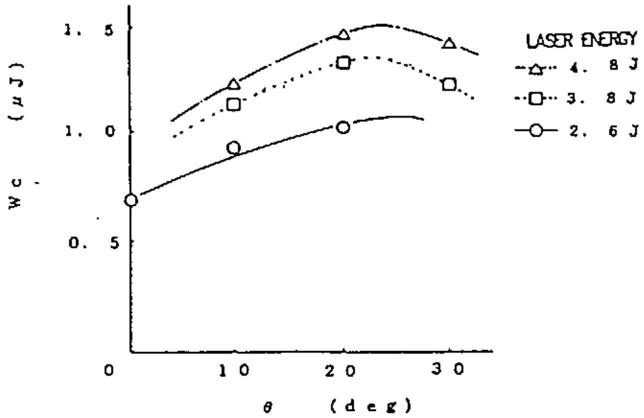

Fig.5. Characteristic of θ -Wcmax

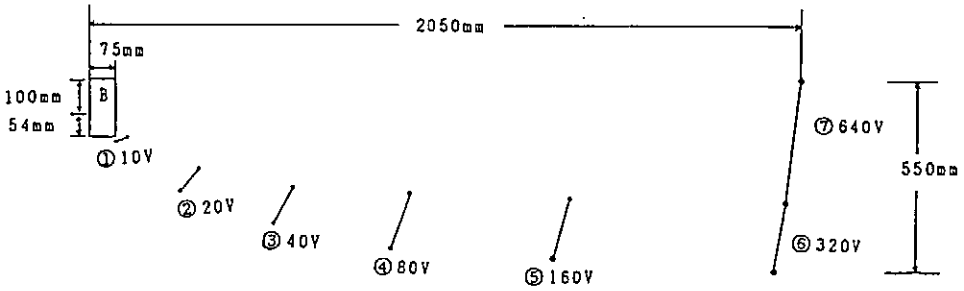

①～⑦: ion collector

Fig.6. Disposition of ion collectors

CHARACTERISTICS OF CORONA-PREIONIZED UV TEA LASER

Takeshi YASUDA, Takamitsu SUZUKI, Keiji NAKAMURA,
Chobei YAMABE and Kenji HORII*
Department of Electrical Engineering, Nagoya University,
Nagoya,Aichi 464-01
*Toyota College of Technology

ABSTRACT

Corona-preionized ultraviolet TEA lasers were examined; TEA-N_2 laser and KrF excimer laser. Capacitance C_s, which is related to preionization is optimized. It was sure that the value of C_s should be determined considering both the uniformity of discharge and the decrease of breakdown voltage. The laser power in the N_2 laser is saturated at about $E/P = 11.5$ V/cm/Torr. In KrF laser, the laser power is increased with increasing total pressure of the laser gas mixture and has the maximum value at $F_2/He \fallingdotseq 2/40$ torr.

1. INTRODUCTION

The laser action in the second positive band system of nitrogen is often used in a nitrogen laser. Though the various excitation methods in N_2 laser are proposed, we examined here a Corona-preionized TEA-N_2 Laser and applied this laser device to a KrF excimer laser.

The characteristics of a corona-preionized TEA laser are as follows.

(1) A corona-preionization system makes the effective discharge volume increase because the uniformity of discharge is improved.

(2) A corona-preionization system is prefer to a long-life laser device because of little spattering from the preionization source.

But, on the other hand, it have a fault such that a glow-to-arc transition is apt to occur under high pressure because the intensity of preionization is weak compared with X-ray or UV preionization system.

In this paper, it is tried to optimize the various parameters to obtain the maximum laser power of N_2 laser and to examine the characteristics of KrF laser.

2. EXPERIMENTAL DETAILS

The schematic diagram of experimental apparatus and electrical circuit is shown in Fig. 1. The main electrodes, 30 mm wide and 1000 mm long, are made of aluminum at a gap length of 25 mm. The anode is formed with the Chang profile(1)-(5) and the cathode has four parallel grooves on the surface along the laser axis. Many trapezoidal protrusions are distributed on the surface along the laser axis between each groove. A trigger electrode covered with a pyrex glass tube is put in each groove.

The electrical discharge circuit with the pulse forming network (PFN) is composed of the capacitances C_1, C_2, the inductances L_1, L_2, and the gap G.

After triggering the gap G, the electrical charge stored in C_1 is transferred to C_2, and the voltage is applied across the main electrodes. Then the trigger current passes through the capacitance C_s before the sparks of the main electrodes gap, and the preionization of the main discharge volume is carried out.

After that the main discharge is produced and the laser oscillation is obtained.

3. THE DEPENDENCE OF LASER POWER ON THE INTENSITY OF PREIONIZATION

The intensity of preionization can be controlled by changing the value of C_s. In order to examine the dependence of laser power on the intensity of preionization, the value of capacitance C is varied as a parameter of V_1 = 18.9 kV and 24.3 kV, where V_1 is the voltage applied on C_1, C is the value expressed by $C = C_s \cdot C_g/(C_s+C_g)$ (C_g: the capacitance of pyrex glass tube) under the condition of capacitances C_1 = 18 nF, C_2 = 17 nF, total pressure = 1 atm, ratio of mixture gas N_2/He = 1/42.

Figure 2 shows the variation of laser power as a function of C in the N_2 laser. The maximum value of the laser power is obtained at a certain value of C. Figure 3 shows Q_t as a function of C, where Q_t is the amount of electric charge injected to triggered circuit before the main discharge initiation. The value of Q_t is increased linearly with increasing the value of C. This experimental variation of Q_t can be considerably explained by the equation $Q_t = C \cdot V_{BD}$

In the relatively low region of C, the laser power is increased with C because the corona preionization is intensified with the increase of Q_t.

Figure 4 shows the variation of the breakdown voltage as a function of C. The value of breakdown voltage is decreased gradually with the increase of C, and that could explain the decrease of laser power. In other words, the provision of too much primary electrons causes the decrease of breakdown voltage and laser power.

This tendency is obtained in the KrF laser, too. Figure 5 shows the variation of laser power as a function of C. In the end, it is sure that the intensity of preionization should be determined in UV lasers considering both the uniformity of discharge and the decrease of breakdown voltage.

4. OPTIMIZATION OF PRESSURE

The optimization of gas pressure in N_2 laser is described here. Figure 6 shows the variation of laser power as a function of total pressure as a parameter of V_1 in the case of C_1 = 40nF, C_2 = 17 nF, N_2/He = 1/42. The laser power is increased with the total pressure up to a certain value of total pressure. However, when the total pressure is increased over that value, the laser power is decreased conversely.

In the relatively low pressure, the laser power is increased with the pressure because of the increase of nitrogen molecules.

However, too much increase of total pressure causes the occurrence of glow-to-arc transition and the decrease of laser power. The decrease of laser power is also due to the decrease of reduced electric field E/P. Figure 7 shows the variation of E/P as a function of total pressure. If the total pressure is increased, the value of E/P is decreased. Then the distribution of electron energy shifts to the lower energy, and the number of nitrogen molecules excited to upper laser level is decreased. Therefore the decrease of E/P causes the decrease of laser power.

Next, Fig. 8 shows the variation of laser power as a function of the ratio of mixture gas N_2/He. According to Fig. 8, the optimum ratio of N_2/He is found to be 1/42.

5. SATURATION OF LASER POWER

Figure 9 shows the variation of laser power as a function of V_1 as a parameter of total pressure. It is found that the value of E/P at the saturation point for the laser power is 11.5 V/cm/Torr in every total pressure (Ref. table 1).

That result suggests that the increase of E/P over 11.5 V/cm/Torr is not significant to increase the laser power. In this N_2 laser device, the maximum laser power 692.0 kW is obtained at C_1 = 40nF, C_2 = 17 nF, Cs = 2000 pF, total pressure = 1.5 atm, N_2/He = 1/42, and V_1 = 40.5 kV.

6. CHARACTERISTICS OF KrF LASER

This N_2 laser device is here applied to a KrF laser and the characteristics of the KrF laser is examined. Figure 10 shows the variation of laser power as a function of partial pressures of F_2/Kr for F_2/Kr/He gas mixture. The laser power is increased with total pressure. Moreover, the optimum partial pressures of F_2/Kr is found to be about 2/40 Torr independently to total pressure.

Figure 11 shows the variation of laser power as a function of V_1. The laser power is not saturated up to 35 kV for V_1, and that could imply that laser power is relatively increased with V_1.

REFERENCE

1) T.Yasuda et.al:Papers of Technical Meeting on Plasma and Discharge,IEE,Japan EP-90-72,ED-90-91 (1990)

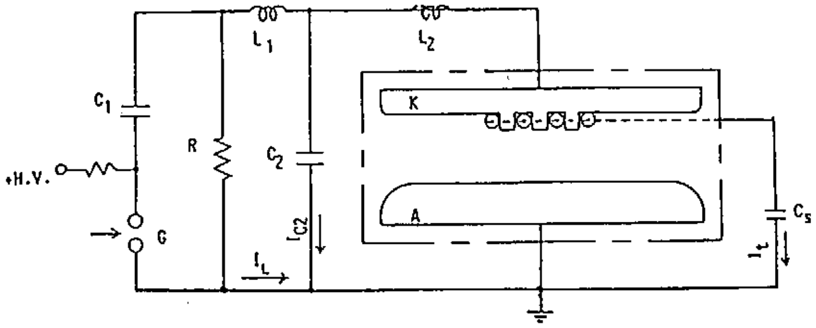

Fig. 1 Schematic diagram of experimental apparatus and electrical circuit

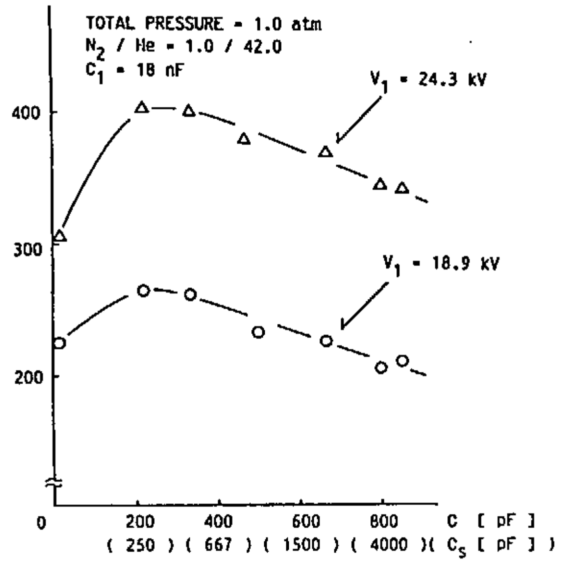

Fig. 2 Variation of laser power as a function of C in N_2 laser

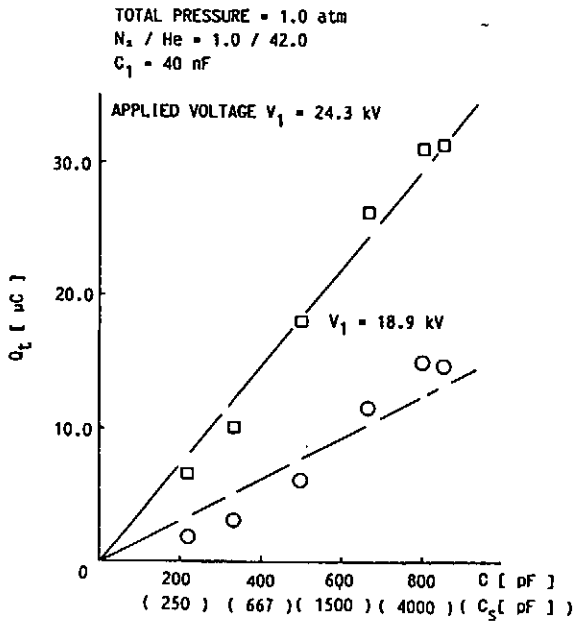

Fig. 3 Q_t as a function of C

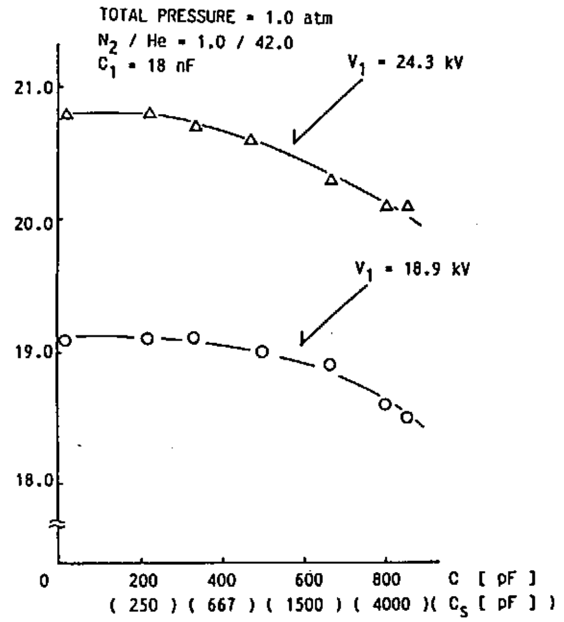

Fig. 4 Variation of breakdown voltage as a function of C

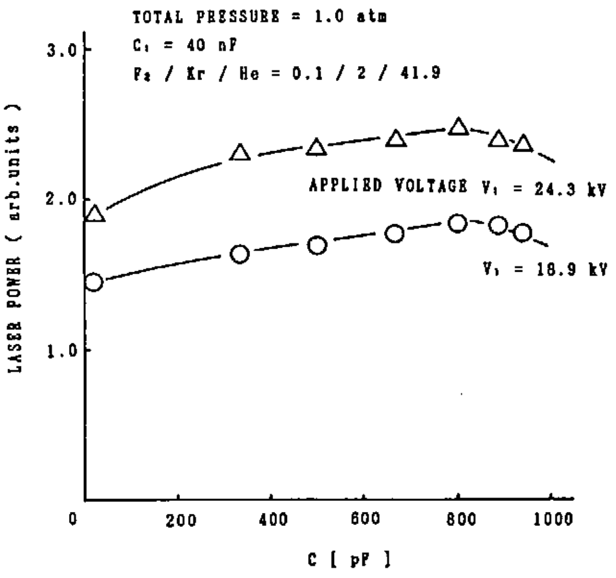

Fig. 5 Variation of laser power as a function of C in KrF laser

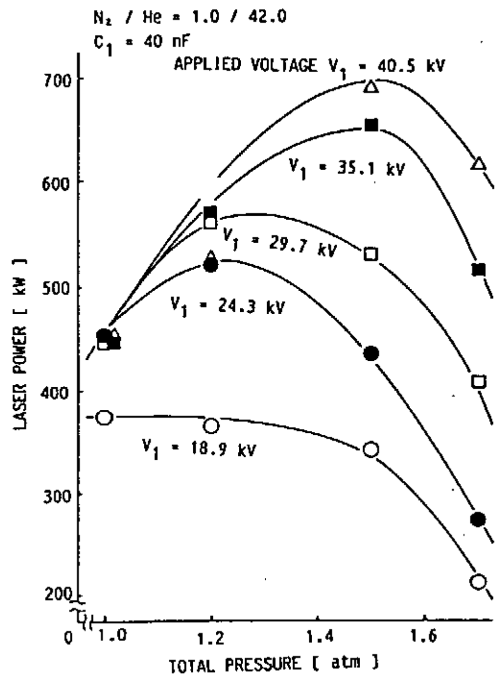

Fig. 6 Variation of laser power as a function of total pressure

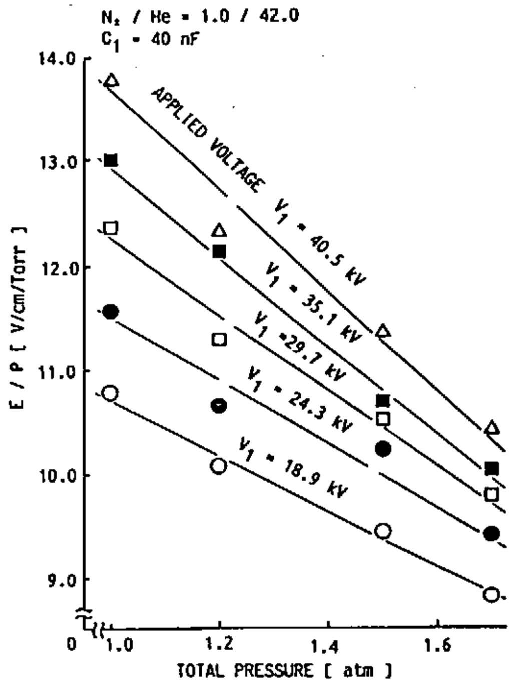

Fig. 7 Variation of E/P as a function of total pressure

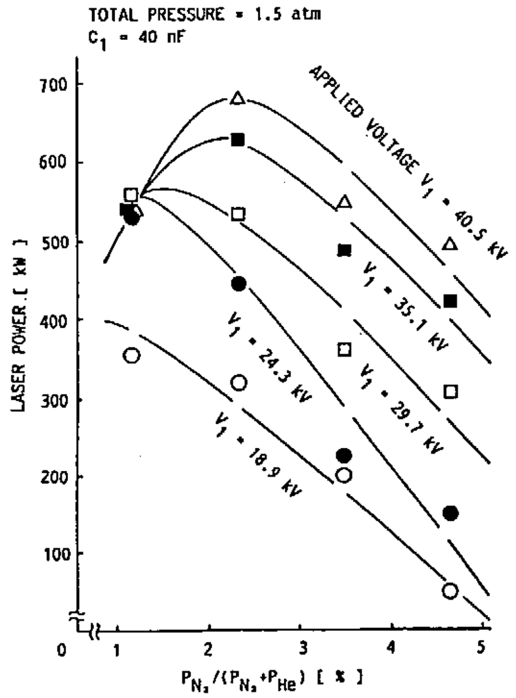

Fig. 8 Variation of laser power as a function of the ratio of mixture gas N_2/He

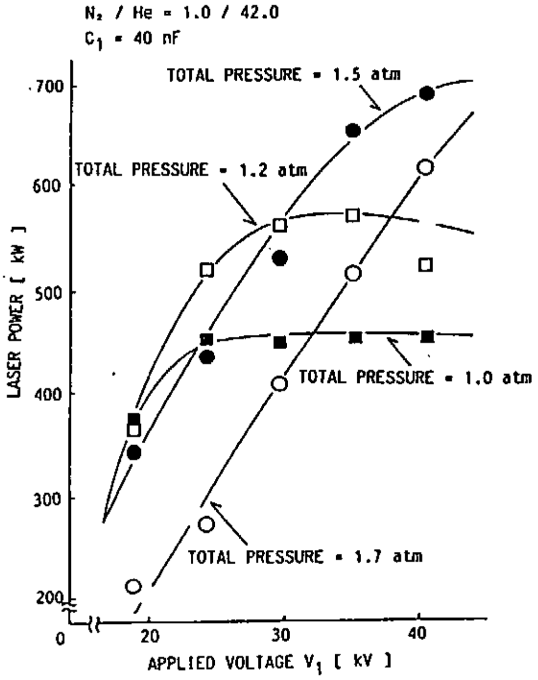

Fig. 9 Variation of laser power as a function of V_1

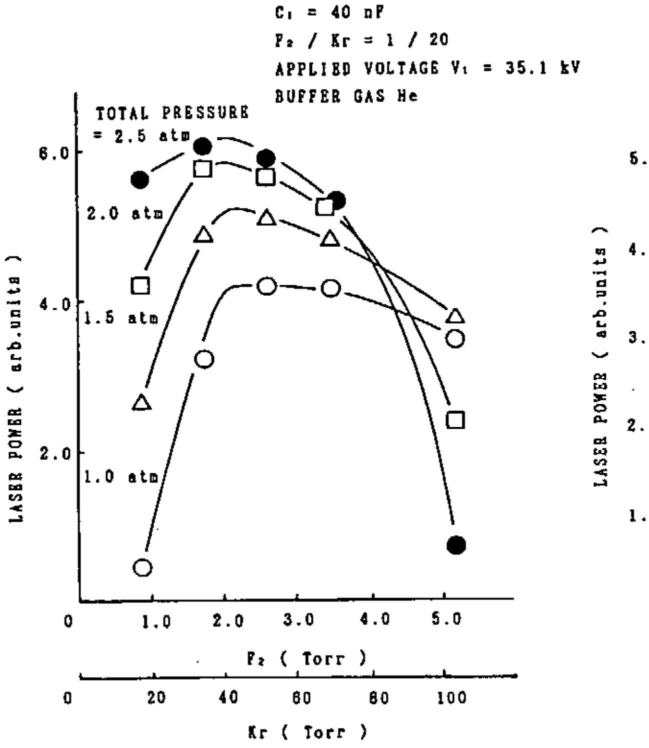

Fig. 10 Variation of laser power as a function of partial pressures of F_2/Kr for F_2/Kr/He gas mixture

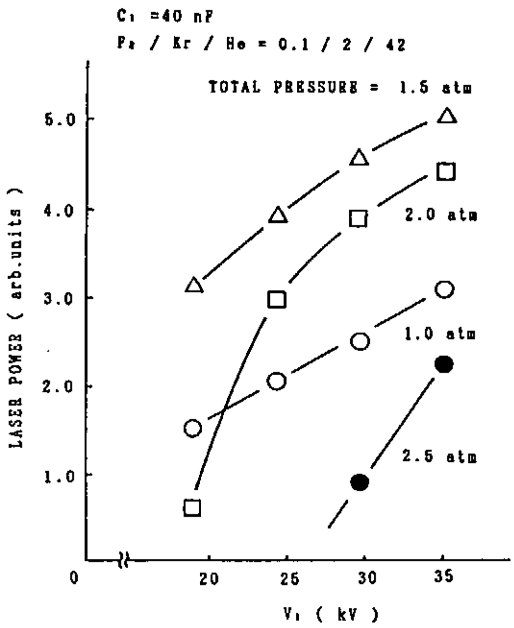

Fig. 11 Variation of laser power as a function of V_1

Total pressure (atm)	at saturation point		
	V_1 (kV)	V_{BD} (kV)	E/P (V/cm/Torr)
1.0	24.3	22.0	11.58
1.2	29.7	25.8	11.32
1.5	40.5	32.5	11.40
1.7	—	—	—

Table 1 E/P at saturation point for laser power

Pulse-Power Technology and Its Applications at LBT, Nagaoka

Laboratory of Beam Technology, Nagaoka University of Technology,
Nagaoka, Niigata 940-21

K. Yatsui, K. Masugata, Y. Sekimoto, W. Jiang, G. Imada,
H. Okuda, S. Kobayashi, T. Komorida, K. Shimiya, and T. Sonegawa

Abstract

An overview is presented on recent progress of pulse-power technology and its applications at Laboratory of Beam Technology, Nagaoka University of Technology. Even in a very short time, extremely high power density will be achieved, which significantly differs from a normal state. In fact, various applications can be available in wide area. It includes R & D in (a) inertial confinement fusion, (b) applications in material science, and (c) applications in laser engineering.

§1. Introduction

Since the establishment of our university in 1978, we started R & D of pulse-power technology and its applications. First of all, in 1980, we contructed a pulse-power machine, "ETIGO-I", producing the pulse-power output of 1.2 MV, 240 kA, 0.3 TW, 50 ns, 14.4 kJ. A little bit later, furthermore, we developed "MALIA-I" (Medium-Mass Atom Linear Induction Accelerator) in 1983, by which we successfully demonstrated the postacceleration of highly-charge and current-neurtralized proton beam. A lot of experimental results were successfully obtained on "ETIGO-I" by intense, pulsed light-ion beams (LIB) such as on generation, focusing, and propagation of LIB, development of new ion diodes, and target-interaction together with the development of various new diagnostic techniques. Applications of LIB were also tried and successful in the preparation of various thin films in material science. Quick preparation of thin films have been available by ion-beam evaporation (IBE), which gives the deposition rate of ~ 4 cm/s. In 1989, "ETIGO-I" was shut down, which was rebirthed as "VIVA-I" (Versatile Induction Voltage Adder) by using Marx generator of "ETIGO-I", which has the pulse-power output of 4 MV, 60 ns by being added 2 MV pulses in two-stages of induction cells. It is particularly specified as highly potential gradient of 2.5 MV/m.

In 1985, we built a new pulse-power machine, "ETIGO-II", which has the pulse-power output of 3 MV, 460 kA, 1.4 TW, 50 ns, 70 kJ. We succeeded in extremely tight focusing of proton beam by self-magnetically insulated "plasma-focus diode" (PFD) originally designed and developed at LBT, where focusing radius of ~ 180 μm was observed to yield power density of ~ 0.1 TW/cm^2 at the beam energy of ~ 1.5 MeV. Enhanced energy deposition was also observed experimentally by the beam-target interaction, which was understood by "plasma" effect from the comparison with computer simulation. Various new diagnostics have been developed particularly on time-resolved measurements of energy spectra, soft X-ray, spectroscopy, etc.

Applications in laser engineering started recently such as the development of highly-repetitive excimer lasers by supersonic gas flow using Ludwieg tube, magnetic pulse compressor by saturable transformer, Raman-type of free-electron laser by high-energy relativistic electron beam, laser-trigged lightning, etc.

In this paper, we briefly mention its recent progress of these studies.$^{1\sim12)}$

§2. R & D in Inertial Confinement Fusion

2-a) Generation and Focusing of LIB and Its Interaction with Targets[5,13~31]

First, we began to study basic characteristics of the LIB extracted from single-current-feed, magnetically insulated diode (MID). The detailed information was obtained by geometrically focused MID. The space-charge effect was disccussed in the connection with beam focusing. Medium-mass ion beams like boron and nitrogen were also obtained as well as LIB like proton beam. Later, dual-current-feed MID was also studied in detail.

Various new ion diodes were originally designed and successfully developed; planar-type self-magnetically insulated diode (PSID), self-magnetically insulated "plasma-focus diode" (PFD), and coaxial, cylindrical magnetically insulated diode (CMID).

Extremely tight focusing of proton beam was achieved by self-magnetically insulated PFD, where focusing radius of ~ 180 μm was observed to yield power density of ~ 0.1 TW/cm^2 at the beam energy of ~ 1.5 MeV. Enhanced energy deposition was also observed experimentally by the ion beam-aluminium target interaction, which was understood by "plasma" effect from the comparison with one-dimensional hydrocode simulation. We have evaluated the plasma temperature ~ 25 eV, the electron density ~ 10^{21} cm^{-3}, and the degree of ionization ~ 40 %.

2-b) Propagation of LIB in Wall-Confined Plasma Channel[32~37]

We studied the propagation of LIB using wall-confined plasma channel in various configuration. Good propagation of ~ 80 % was observed through 50 cm-long channel whenever the channel is stable against a macroscopic instability. When, however, the channel becomes unstable, the propagation efficiency tends to be strongly decreased against sausage instability. When such the intability is removed by applying longitudinal magnetic field, the propagtion efficiency again increases. We also studied the propagation of LIB in the overlapped channels. The effect of pressure in the channel was also studied on the propagation of LIB. Final focusing of proton beam by z-discharged plasma channel was observed both experimentally and theoretically.

2-c) Development of New Diagnostic Techniques[38~44]

Various new diagnostic techniques have been successfully developed of time-resolved measurements; Thomson-parabola energy spectrometer, soft X-ray using a microchannel-plate image intensifier, crystal spectroscopy of the emission from inner shell excited by charged particle beams, spectroscopic measurement using streak camera, and so on.

2-d) R & D of Pulse-Power Technology[45~50]

After the success of development of "MALIA-I" of postaccelerator of highly charge- and current-neutralized LIB by use of saturable ferrite cores, we have developed "VIVA-I" by using Marx generator of "ETIGO-I", which has the pulse-power output of 4 MV, 60 ns by adding 2 MV pulses in two-stages of induction cells. It is particularly specified as highly potential gradient of 2.5 MV/m. Various initial tests were successfully carried out on open-circuit test, dummny-load test, and eletron-beam production test.

§3. Applications in Material Science

3-a) Preparation of Various Thin Films at Low Temperature by IBE[10,12,51~58]

Using high-density, high-temperature "ablation" plasma when LIB is irradiated onto solid targets, we have prepared various thin films at low temperature such as of ZnS, ZnS:Mn, B, C, ITO, $BaTiO_3$, YBaCuO, apatite, and so on. Quick preparation of thin films have been available by IBE, which gives the instantaneous deposition rate of ~ 4 cm/s.

3-b) High-Energy Ion Implantation and Surface Modification[5,10,12,59~61]

High-energy ion implantation of intense, pulsed, boron and nitrogen beams into titanium has been performed to make TiN and TiB_2, respectively. The normalized resistivity of TiN formed was found to be in good agreement with the classical value after being fired by 100 shots continuously. A factor of ~ 40 % increase in Vickers hardness of titanium has been found when it is irradiated by 70 shots.

3-c) Radiation Damage Effect[62]

We have studied radiation damage effect by being irradiated by LIB onto Si_3N_4-SiC films ($SiN_{1.42}$, $SiN_{0.65}C_{0.62}$, and $SiC_{1.04}$) prepared on a stainless steel (SUS-316) or bare steel (SUS-316). Blistering (for $SiN_{1.42}$) or flaking (for $SiC_{1.04}$) takes place. Erosion rate is found to 0.46, 0.5 and 0.73 μm/shot for $SiN_{1.42}$, $SiN_{0.65}C_{0.62}$, and $SiC_{1.04}$, respectively.

§4. Applications in Laser Engineering

4-a) Highly Repetitive Excimer Laser by Supersonic Gas Flow[63]

We have constructed highly-repetitive (> 5 kHz) excimer lasers by using Ludwieg charge tube, where supersonic gas flow of > 200 m/s is available within the pulse width of ~ 100 ms.

4-b) Magnetic Pulse Compressor by Saturable Transformer[64]

To develop highly-repetitive, long-lived circuit for excimer lasers, we have designed and developed a new circuit where a saturable transformer is inserted in magnetic pulse compressor. The initial pulse of 17.5 kV, 1.8 kA, and 1.5 μs has been converted into the pulse of 34 kV, 9.2 kA, and 90 ns, which yields the energy conversion efficiency of ~ 63 %. Furthermore, significant reduction in the prepulse has been achieved by inserting saturable inductor in parallel to a peaking capacitor.

4-c) Raman-Type of Free Electron Laser by High-Energy Relativistic Electron Beam

To develop intense and pulse radiation source in millimeter or sub-millimeter range, we have started basic studies of Raman-type of FEL by high-energy relativistic electron beam such as obtained by VIVA-I mentioned above.

4-d) Laser-Triggered Lightning

To control lightning artificially by laser, which happens and very harmful particularly in Hokuriku area in winter, we are developing high-power CO_2, YAG, or excimer lasers. Basic characteristics of plasma channel produced by these lasers or by its combination are studied.

§5. Summary

Recent progress has been quickly overviewed on pulse-power technology and its applications at LBT, Nagaoka. Although our project originally started in inertial confinement fusion research, there are recently growing and wide interests in applications in material science or laser engineering. Very promising and fruitful achievements can be expected in the future since it is able to obtain extremely high power density even in a very short time.

Acknowledgements

This work was partly supported by a Grant-in-Aid from the Ministry fo Education, Science, and Culture of Japan.

References

1) K. Yatsui: Proc. US-Japan Workshop on Compact Toroid, Osaka Univ., 105 (1981).
2) K. Yatsui et al.: Proc. 4th Int'l Conf. on High-Power Electron and Ion Beam, Paris, 27 (1981).
3) K. Yatsui et al.: Proc. 5th Int'l Conf. on High-Power Particle Beams, San Francisco, 34 (1983).
4) K. Yatsui et al.: Proc. 1984 INS Int'l Symp. on Heavy Ion Accelerator and Their Applications to Inertial Fusion, Tokyo, 882 (1984).
5) K. Yatsui et al.: Laser and Particle Beams 3, 119 (1985).
6) K. Yatsui et al.: Laser and Particle Beams 5, 415 (1987).
7) K. Yatsui et al.: Proc. 11th Int'l Conf. on Plasma Phys. and Controlled Nucl. Fusion Res., Kyoto, 3, 177 (1987).
8) K. Yatsui et al.: Proc. 7th Int'l Conf. on High-Power Particle Beams, Karlsruhe, I, 522 (1988).
9) K. Yatsui et al.: Proc. 12th Int'l Conf. on Plasma Phys. and Controlled Nucl. Fusion Res., Nice, 3, 15 (1989).
10) K. Yatsui: Laser and Particle Beams 7, 733 (1989).

11) K. Yatsui et al.: Proc. 8th Int'l Conf. on High-Power Particle Beams, Nobosibirsk, C03 (1990).

12) K. Yatsui et al.: Proc. 3rd Int'l Workshop on Intense Ion Beam Interaction with Matter, Albuquerque (1990).

13) K. Masugata et al.: Jpn. J. Appl. Phys. 20, L347 (1981).

14) K. Yatsui et al.: Bull. Amer. Phys. Soc. 27, 1072 (1982).

15) K. Masugata et al.: Jpn. J. Appl. Phys. 20, L347 (1982).

16) K. Yatsui et al.: Phys. Rev. A26, 3044 (1982).

17) K. Yatsui et al.: Bull. Amer. Phys. Soc. 2, 1055 (1983).

18) T. Yoshikawa et al.: J. Appl. Phys. 56, 3137 (1984).

19) K. Masugata et al.: Bull. Amer. Phys. Soc. 29, 1292 (1984).

20) E. Sai et al.: Proc. Proc. Collab. Res. Mtg. on Development of High-Power Particle Beams, IPPJ-742, 69 (1984).

21) Y. Shimotori et al.: Proc. Topical Mtg. on Particle Beam Fusion and Its Related Problems, IPPJ-769 (2), 267 (1986).

22) A. Tokuchi et al.: Proc. 2nd Int'l Topical Symp. on ICF Res. by High-Power Particle Beams, Nagaoka, 430 (1986).

23) M. Murayama et al.: Jpn. J. Appl. Phys. 27, 1526 (1988).

24) M. Matsumoto et al.: Laser and Particle Beams 6, 555 (1988).

25) A. Takahashi et al.: Proc. Topical Mtg. on Particle Beam Fusion and Its Related Problems, IPPJ-769 (2), 282 (1986).

26) K. Yatsui et al.: Bull. Amer. Phys. Soc. 32, 1877 (1987).

27) K. Yatsui et al.: "Laser Interaction and Related Plasma Phenomena", (Plenum Press, NY and London), 8, 653 (1988).

28) K. Masugata et al.: Laser and Particle Beams 7, 287 (1989).

29) W. Jiang et al.: Proc. 9th Int'l Workshop on Laser Interaction and Related Plasma Phenomena, Monterey (1989).

30) W. Jiang et al.: Jpn. J. Appl. Phys. 29, 434 (1990).

31) W. Jiang et al.: Laser and Particle Beams 9, #3 (in press) (1991).

32) K. Yatsui et al.: Phys. Lett. 89A, 235 (1982).

33) T. Yamada et al.: Jpn. J. Appl. Phys. 21, L699 (1982).

34) T. Yamada et al.: Jpn. J. Appl. Phys. 21, L278 (1983).

35) K. Yatsui et al.: Proc. 5th Int'l Conf. on High-Power Particle Beams, San Francisco, 82 (1983).

36) S. Nakamura et al.: Proc. Collab. Res. Mtg. on Particle Beam Appl. to Fusion Res., IPPJ-678, 266 (1984).

37) M. Nakahama et al.: Jpn. J. Appl. Phys. 25, L13 (1986).

38) H. Tanaka et al.: Jpn. J. Appl. Phys. 21, L647 (1982).

39) T. Matsuzawa et al.: Rev. Sci. Instrum. 56, 2279 (1985).

40) M. Ikeda et al.: Proc. Topical Mtg. on Particle Beam Fusion and Its Related Problems, IPPJ-769 (2), 305 (1986).

41) Y. Shimotori et al.: Proc. 6th Int'l Conf. on High-Power Particle Beams, Kobe, 97 (1986).

42) K. Masugata et al.: Ann. Rev. Inst. Plasma Phys. April '87 ~ March '88, 103 (1988).

43) Y. Kawano et al.: Laser and Particle Beams 7, 277 (1989).

44) H. Okuda et al.: Proc. IEEJ Symp. on Plasma Physics, EP-90-95 (in Japanese)(1990).

45) T. Tanabe et al.: Phys. Rev. Lett. 56, 831 (1986).

46) T. Aoyama et al.: Proc. Symp. on Production and Target Interaction of Particle Beam, Nagoya, 100 (1989).

47) K. Masugata et al.: Proc. 8th Int'l Conf. on High-Power Particle Beams, Novosibirsk, U17 (1990).

48) K. Yatsui et al.: Bull. Amer. Phys. Soc. 35, 2054 (1990).

49) K. Yatsui et al.: Proc. 3rd Int'l Workshop on Intense Ion Beam Interaction with Matter, Albuquerque (1990).

50) K. Shimiya et al.: Proc. Symp. on Development of Intense Pulsed Particle Beams and Its Applications, Nagaoya, 59 (1990).

51) M. Yokoyama et al.: Proc. World Conf. on Advanced Materials for Innovations, Energy Transportation and Communications, Tokyo, IA03 (1987).

52) Y. Shimotori et al.: J. Appl. Phys. 63, 968 (1988).

53) K. Yatsui: Jpn. J. Appl. Phys. 28, 468 (1989).

54) Y. Shimotori et al.: Proc. 6th Symp. on Plasma Processing, Kyoto, 569 (1989).

55) K. Yatsui et al.: Bull. Amer. Phys. Soc. 34, 2063 (1989).

56) Y. Shimotori et al.: Proc. 4th Int'l Workshop on Electroluminescence, Tottori, 232 (1989).

57) K. Yasui et al.: Bull. Amer. Phys. Soc. 35, 2143 (1990).

58) T. Sonegawa et al.: Proc. IEEJ Symp. on Plasma Physics, EP-90-64 (in Japanese)(1990).

59) K. Yatsui et al.: Proc. Int'l Joint Symp. on Newer Trends of Surface Modification, 21 (1988).

60) K. Yatsui et al.: Proc. 20th Symp. on Ion Implantation and Submicron Fabrication, Tokyo, 21 (1989).

61) T. Takaai et al.: Proc. Int'l Conf. on Surface Enginnering, Toronto (1990).

62) K. Kamata et al.: Laser and Particle Beams 5, 495 (1987).

63) G. Imada et al.: Proc. IEEJ Symp. on Plasma Physics, EP-90-93 (in Japanese)(1990); also, in preparation for publication.

64) S. Kobayashi et al.: Proc. IEEJ Symp. on Plasma Physics, EP-90-94 (in Japanese)(1990); also, in preparation for publication.

CHARACTERISTICS OF ION BEAM GENERATED WITH THE "POINT PINCH DIODE"

M. Sato, S. Tokimasa, M. Yatsuzuka,
S. Nobuhara and T. Tazima†

Department of Electrical Engineering,
Himeji Institute of Technology,
Shosha, Himeji 671-22, Japan
†National Institute for Fusion Science
Furo-cho, Nagoya 464-01, Japan

Abstract

We investigated the characteristics of the ion beams generated with the "Point Pinch Diode", and detected copper ions with the Thomson-parabola ion spectrometer. From time of flight measurement for the ion beams, we evaluated the ratio of number densities between the proton H^+ and the copper ion in the fourth state of ionization Cu^{4+}. The result shows that the number density of Cu^{4+} typically corresponds to a half of that of H^+.

§1. Introduction

The "Point Pinch Diode"1) has been proposed as one of the diode used in a simple and cheap pellet compression scheme by indirect irradiation of relativistic electron beams (REB) 2), and consists of a small spherical cathode and a small flat anode. In this diode, an ion beam with high current density (several tens of kA/cm^2) is easily generated, although only a small energy is put into the diode (about 1 kJ) 3). It was also reported that this ion beam contained a lot of metallic ions, the origin of which was anode materials4).

In order to apply this metallic ion beam to development of new materials (e.g. modification of surface layer), we have to know the characteristics of the ion beam at the outside of the diode. For example, there are the detail informations of a radial profile and a composition of the ion beam, and numbers of each ion species. Generally a Thomson-parabola ion spectrometer is used to evaluate the composition of the ion beam, and an array of a biased ion collector (BIC) is also used to evaluate the radial profile of it. We tried to make rough evaluation of the numbers of ions by the time of flight (T.O.F.) method.

The T.O.F. method is generally used to analyze the species of ion beams[5]. After analyzing the ion species, we roughly evaluate the number density n of the ion beam from the equation of the current density j.

$$j = Z n e v$$

Here Z and e are the charge state of ionization and the charge of the proton, respectively. If j is measured with any detectors, n is able to be calculated, because the velocity v of the ion is also obtained by the T.O.F. method.

We also tried a new method of distinguishing metallic ions, because the Thomson-parabola ion spectrometer and the T.O.F. method can only distinguish the ratios of A/Z, where A is the mass of ions. The new method is similar to the ion implantation technique for development of semiconductors[6], and its procedure is as follows. The accelerated ions are put into a silicon target located at the outside of the diode. After the shot, the silicon target is analyzed with the secondary ion mass spectroscopy (SIMS). By this method, the effect of charge state of ionization is removed. Therefore, if the ions of Cu^{4+} have been accelerated, the signal which corresponds to the mass of the copper 65 is able to be detected.

In this paper we present the results of investigating the ion beam generated with the "Point Pinch Diode", mainly by the T.O.F. method.

§2. Experimental Setup

The pulse power generator "HARIMA-II" (400 kV, 3 Ω, 50 ns) was used in experiments. All of the experiments reported here were performed with the output voltage of 480 kV. Figure 1 shows the experimental setup arranged at the end of the "HARIMA-II". As shown in Fig. 1, the "Point Pinch Diode" consists of a hemispherical mesh cathode and a flat anode. The cathode is made by reforming the mesh which consists of fine wires with separation of 1.1 mm. The wires are made of stainless steel, and its diameter is 0.1 mm. A transparency of the mesh is 72 %. The anode was a square copper plate which is attached to the end of a anode rod of which diameter is 60 mm. A size and a thickness of the anode plate were 30 and 1.5 mm, respectively.

The behavior of the "Point Pinch Diode" is as follows. When a high voltage is supplied from the "HARIMA-II", electrons emitted from the top of the cathode are accelerated to the anode. By an azimuthal magnetic field generated by the electrons, electrons emitted near the top of the cathode move towards the center of the diode, that is pinch occurring. These electrons bombard the cathode, and produce an spot like anode plasma. This anode plasma expands towards the cathode. At the same time, the cathode plasma expands towards the anode. Just before closure of an anode-cathode (A-K) gap, an intense ion beam is generated.

A voltage at the diode (V_d) was measured with a resistive voltage divider. A diode current (I_d) was measured with a Rogowski coil. Two types of biased ion collectors (BIC) were used to measure a current of the ion beam. One of them is called as a large BIC, and is used to measure a total current of the ion beam (I_i). A grounded plate which has many small apertures is located in front of the BIC. This ground plate was used to pass only a small part of the ion beam. The diameter of the aperture and the distance of separation between the apertures are 0.5 and 10 mm, respectively. From these values, the transparency of the grounded plate is 0.2 %. A charge collector in the BIC was biased at -450 V to remove the accompanying electrons.

Another type of a BIC has a biased grid to remove the accompanying electrons, and its collector is not biased. This BIC was used in evaluation of time of flight for the ions. That is, the signals measured with two BICs are compared. As shown in Fig. 1, a collector 1 of BIC1 was placed at 200 mm from the anode surface, a collector 2 of BIC2 was also placed at 400 mm from the collector 2. The collector 1 is made of the mesh which is same one used as the cathode. Since the mesh collector was used, same part of the ion beam was detected with the two collectors. The voltage of -500 V was supplied to each biased grid to remove the accompanying electrons. A detail procedure for the T.O.F. method is mentioned in §1. In the experiments, the exact value of j is not obtained, because the BIC with the biased grid has some meshes. Therefore we evaluated ratios of number densities between the proton and metallic ions.

A Thomson-parabola ion spectrometer was employed for analyzing the species and those energies of the ion beams, and consisted of a collimator, an electric and a magnetic deflection section, and a film holder. The collimator has two pinholes of which diameters are 0.2 and 0.5 mm. The maximum values of the magnetic and the electric field are 0.54 T and 6 kV/cm, respectively. The film CR-39 was used for detection of the analyzed ions.

§3. Experimental Results

3.1 Measurement of Ion Beam Current with the large BIC

The wave-forms of the diode voltage and the diode current are shown in Fig. 2 (a). In this shot, the cathode radius and the A-K gap length were about 6.5 and 2.4 mm, respectively. The diode voltage initially reaches at 200 kV by 10 ns, and slowly increases up to about 300 kV. After that, V_d sharply drops due to shortening of the A-K gap by expansion of the anode and the cathode plasma. Just before this shortening, the intense ion beam is generated. The diode current starts to rise 10 ns after Vd rises, and its value just before shortening is about 30 kA.

Figure 2 (b) shows the wave-form of the ion beam measured with the large BIC. This signal was obtained by the same shot shown in Fig. 2 (a). The wave-form of I_i is a pulse shape and its peak value is 780 A. The increase after the pulse is caused by shortening of the gap between the grounded plate and the collector of the large BIC. Figure 3 shows dependence of the ion beam current on the A-K gap length. This dependence is similar to one reported in ref. 4. The current increases with increase of the A-K gap, after that it decreases. In Fig. 3, I_i has the maximum value of 850 A at the A-K gap length of 1.8 mm.

3.2 Analysis of Ion Species with Thomson-Parabola Ion Spectrometer

The species and the energies of the ions were analyzed with the Thomson-parabola ion spectrometer. The traces on the film CR-39 are shown in Fig. 4. The experiment to obtain the traces was performed under the condition of the cathode radius of 6.5 mm and the A-K gap length of 1.8 mm. In this shot, the Thomson-parabola ion spectrometer operated with the electric field of 3 kV/cm and the magnetic field of 0.1 T. A spot like trace is found at an intersection of a vertical and a horizontal line. This corresponds to the trace by neutral particles, and corresponds to the origin of the coordinate in the Thomson-parabola ion spectrometer.

Figure 4 shows that the ion beam contains a lot of hydrogen, carbon and oxygen ions. It is considered that these ions are generated from the anode plasma produced from water and oil mist adsorbed on the anode surface, because only the copper is used as the anode material. In the carbon and the oxygen ions, it is found that the ions which have two to four times higher energies than that obtained by the diode voltage (170 kV). These high energy ions are able to be produced through charge-exchange process. The copper ions in the third to the fifth state of ionization are also detected. The energies of these ions are slightly lower than that of the protons. This means that the copper ions are only accelerated when an effective A-K gap length is considerably short.

3.3 Evaluation of Number Densities of Each Ion Species by Time of Flight Method

Figures 5 show the wave-forms of the diode voltages and the ion currents measured by using the BICs with the biased grid. The wave-forms shown in Figs. 5 (a) and (b) were obtained with the A-K gap lengths of 2.4 and 3.3 mm, respectively. In both cases, the cathode of which radius was about 8.5 mm was used. In Fig. 5 (a), three spikes are easily distinguished as H^+, H_2^+ and Cu^{4+}. The timings of the other ions shown in Fig. 5 (a) are estimated by using the diode voltage of 250 kV. From calculation of the time of flight for the ions, the energies of the H^+, H_2^+ and Cu^{4+} are estimated as 230, 260 and 210 keV, respectively. The reason why these energies are different from the diode voltage is caused by no taking into account of inductive correction and overlapping of low energy protons to the other ions. However it is estimated that evaluation errors are less than 10 %.

Using the current densities and the velocities of the ion beams, we calculate the ratio of the number densities between the proton H^+ and the copper ion in the fourth state of ionization Cu^{4+}. The calculated ratio for Fig. 5 (a) is as follows.

$$H^+ : Cu^{4+} = 1 : 0.5$$

This value is typical one. This ratio also agrees with one obtained by counting the traces on the film CR-39. In the case of a long A-K gap length, the number density of Cu^{4+} was higher than that of H^+. The maximum ratio is obtained from Fig. 5 (b);

$$H^+ : Cu^{4+} = 1 : 6.1$$

This result is due to the decrease of H^+, and the peak value of Cu^{4+} is not varied from that of Fig. 5 (a). The reason why H^+ decreases is not made clear, but it is considered that the decrease of H^+ is caused by the difference of a radial profile of H^+ at a time when the protons are accelerated.

3.4 Distinguishing Copper Ions with SIMS

We also tried the new method of distinguishing metallic ions, because the Thomson-parabola ion spectrometer and the T.O.F. method can only distinguish the ratios of A/Z. The detail procedure of the new method is mentioned in §1. Figure 6 (a) shows the analyzed result with the auger electron spectroscopy (AES). This result shows what kind of the atoms are located in the surface layer of the silicon target. Since the signal corresponds to the mass of the copper 65 was detected with AES, we performed analysis with the secondary ion mass spectroscopy (SIMS).

The analyzed result with SIMS is shown in Fig. 6 (b). A vertical and a horizontal axis of Fig. 6 (b) show the counts of signals for each atom per second and the period from start of analysis (sputter time), respectively. This sputter time corresponds to the analyzing depth from the surface of the silicon target, and the sputter time of twelve minutes also corresponds to the depth of two hundreds angstroms. Each number shown in Fig. 6 (b) shows each detected mass at each time. From this figure, it is made clear that the copper atoms are located only near the surface of the silicon target, and the surface layer of the silicon target contains a lot of the chromium and the iron atoms. This means that the electrode plasmas are deposited on the surface of the target. In order to remove the effect of the electrode plasmas, we shall use the silicon target as the detector of the Thomson-parabola ion spectrometer.

§4. Summary

We investigated the characteristics of the ion beams generated with the "Point Pinch Diode" at the outside of the diode, and obtained same dependence of the ion beam current on the A-K gap length reported ago. The traces by metallic ions were also detected. From these results, it was verified that previously reported results are same as our results.

From time of flight measurement for the ions, we evaluated the ratios of number densities between the proton H^+ and the copper ion in the fourth state of ionization Cu^{4+}. The typical ratio was as follows.

$$H^+ : Cu^{4+} = 1 : 0.5$$

In the case of a long A-K gap length, the number density of Cu^{4+} was higher than that of H^+. The maximum ratio was as follows.

$$H^+ : Cu^{4+} = 1 : 6.1$$

References

1) T. Tazima, M. Sato and H. Yonezu: Jpn. J. Appl. Phys. 25 (1986) L697.

2) T. Tazima, M. Sato and H. Yonezu: Proc. 6th Int. Conf. High-Power Particle Beams, Kobe (1986) 313.

3) T. Tazima and M. Sato: Proc. 8th Int. Conf. High Power Particle Beams, Novosibirsk (1990) 523.

4) M. Sato : Jpn. J. Appl. Phys. 26 (1987) 927.

5) D. W. Swain, S. A. Goldstein, L. P. Mix, J. G. Kelly and G. R. Hadley: J. Appl. Phys. 48 (1977) 1085.

6) J. W. Mayer, L. Eriksson and J. A. Davies: Ion Implantation in Semiconductors, Academic Press, (1970).

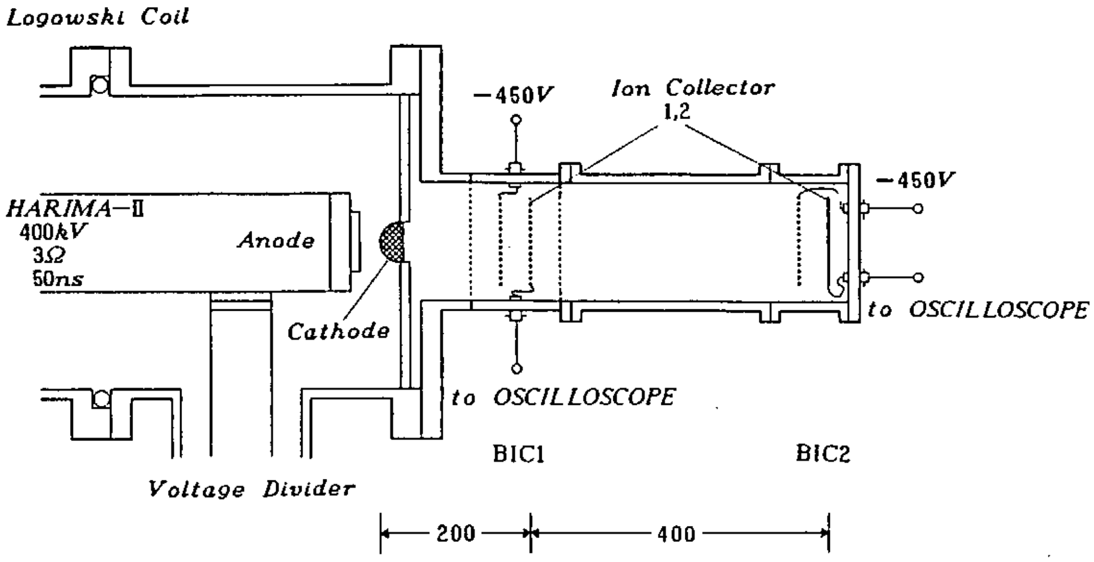

Fig. 1. Schematic drawings of the experimental setup for ion beam generation with the "Point Pinch Diode".

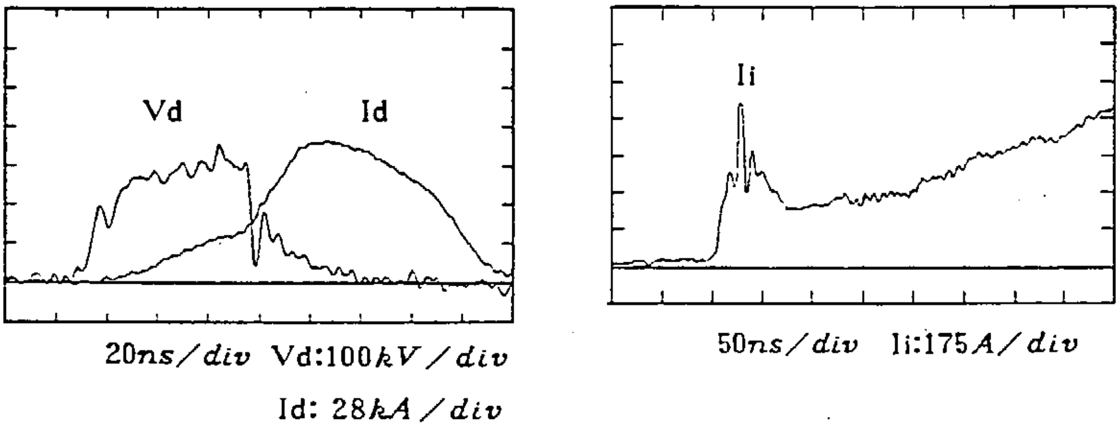

(a) (b)

Fig. 2. The typical wave-forms of the diode voltage V_d and the diode current I_d (a), and the total current of the ion beam I_i (b).

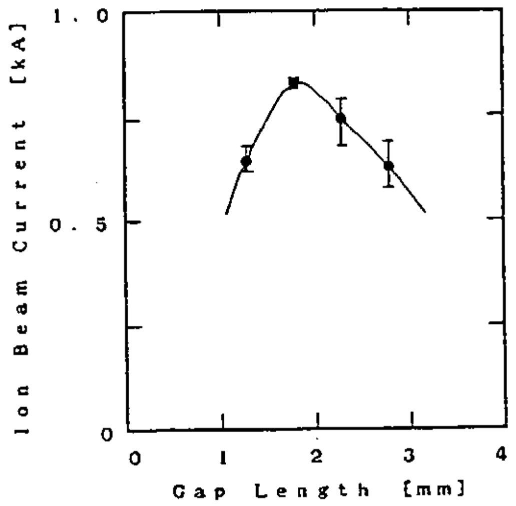

Fig. 3. Dependence of the total current Ii on the A-K gap length.

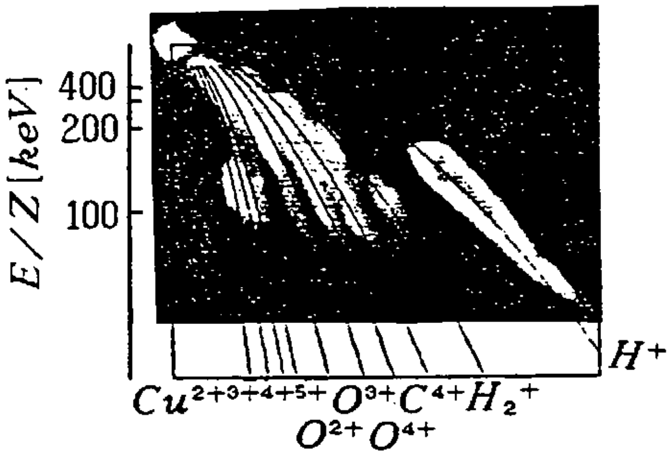

Fig. 4. Traces on the film CR-39 located in the Thomson-parabola ion spectrometer.

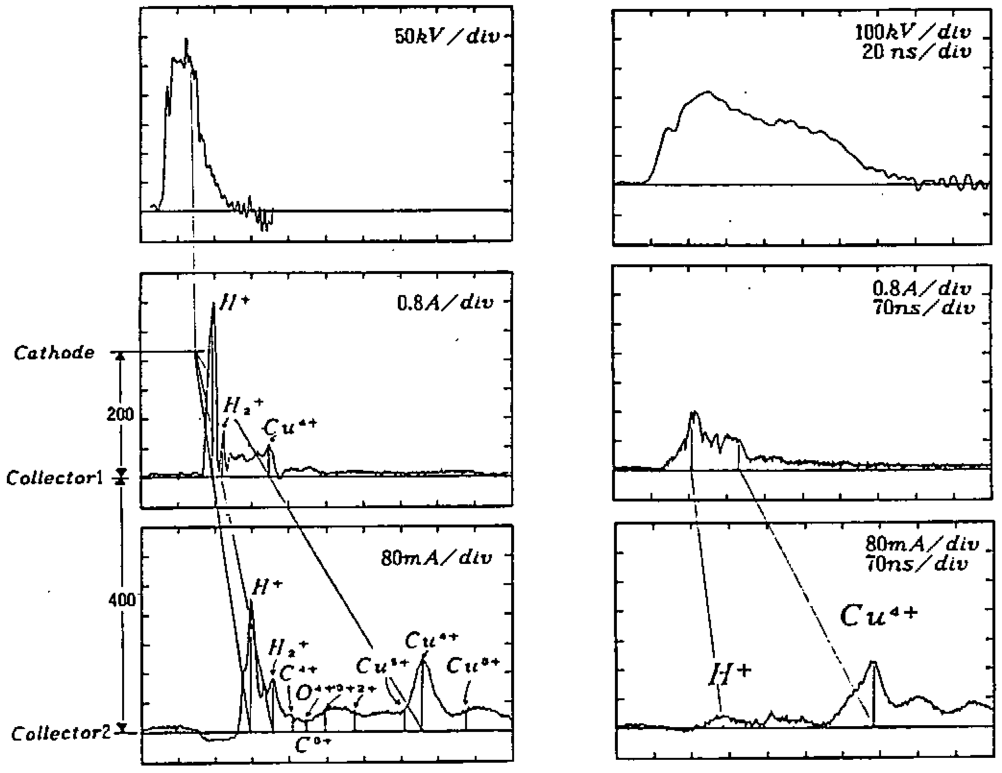

(a)

(b)

Fig. 5. The wave-forms of the diode voltage and the ion beam currents measured using the BICs with the biased grid. The experiments were performed with the A-K gap length of 2.4 mm (a) and 3.3 mm (b).

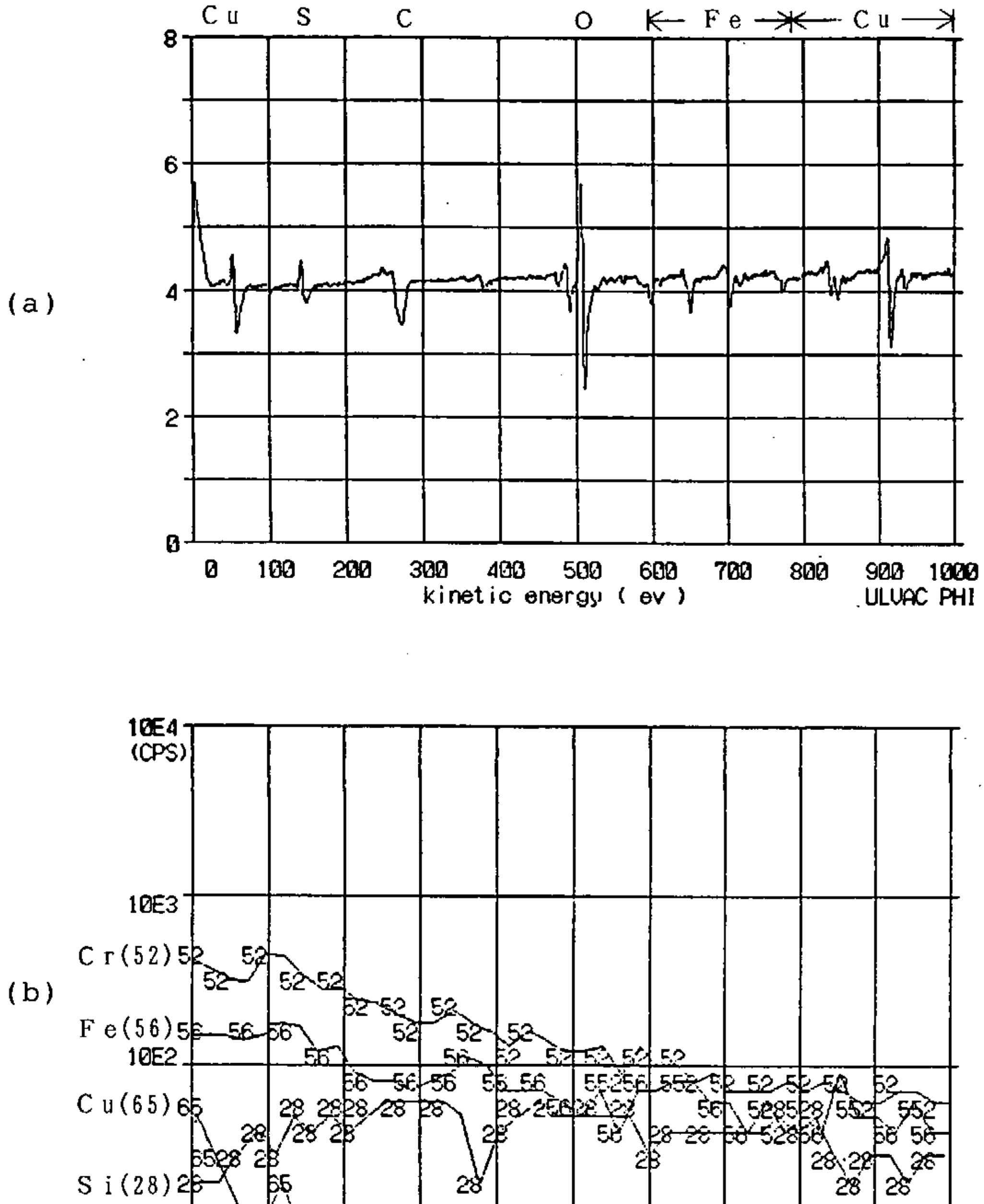

Fig. 6. Analyzed results for the silicon target with the auger electron spectroscopy (a) and the secondary ion mass spectroscopy (b).

Soft X-ray emission from a gas-puff z-pinch plasma

S.Ueda, S.Maeda and H.Akiyama

Kumamoto University

Abstract

Soft X-ray emission or radiation were studied by using a gas-puff z-pinch device, which has no triggered switch. A PIN-photodiode covered by aluminum was used for the detection of soft X-ray. The three kinds of spatial emission pattern were observed from measurement using pinhole camera. Hot spots were observed near the middle of discharge. In order to determine the pressure of the gas during the discharge, a simulation of a gas-puff z-pinch plasma was done with the snow plow model. The gas pressure is supposed as approximately 1Torr.

1. Introduction

The soft X-ray sources with high intensity have many applications as X-ray lithography, soft X-ray microscopes(1),(2), et al. Synchrotron orbital radiation(SOR) and plasma X-ray sources are more efficient and higher intensity than other X-ray sources. Plasma X-ray sources is more attractive because of low cost.

One of the plasma X-ray sources is a gas-puff z-pinch, in which a hollow plasma is imploded by a large axial current. The gas-puff z-pinch device has some advantages, for example, the compact device and to interrupt the secondary discharge. The gas-puff z-pinch devices have been studied extensively(3)-(5). In their experiments, the devices using a triggered spark gap were used. Here a gas-puff z-pinch device without a triggered spark gap is constructed to get the lowest inductance and time- and space-resolved soft X-ray emissions are measured.

2. Experimental Setup

Fig.1 shows the schematic diagram of experimental apparatus. The chamber is cylindrical in shape, and about 1m high and 0.35m in diameter. The electrodes material is brass. The inductance of the device is about 100nH. An annular gas with 2mm thickness is injected from cathode to anode through a fast opening valve. The discharge is triggered by a gas injected between the electrodes. The diameter of injected gas is varied by exchanging a different cathode. The capacitor with 1.88 μ F is charged to 20kV.

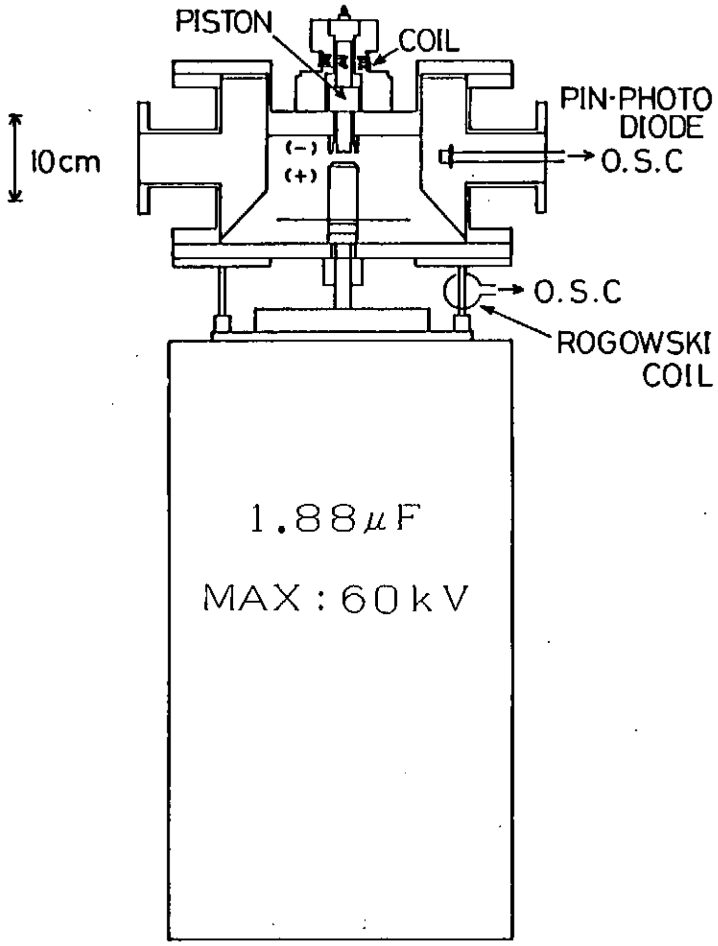

Fig.1 Schematic diagram of the gas-puff z-pinch device

3. Experimental Results

A. Soft X-ray emission

Soft X-ray was detected with a PIN-photodiode covered with a 2 μ m-thick aluminum. The current was measured with a Rogowski coil located at one of the return rods. The injected gas was Ar. The diameter of injected gas and the gap separation are changed. The waveforms of X-ray are divided into three patterns. Fig.2 shows typical waveforms; (a)l=1cm, 2r=5mm, (b)l=1cm, 2r=18mm, (c)l=2cm, 2r=18mm, where l and 2r are the gap separation and the diameter of injected gas respectively. Several soft X-ray pulses are measured during a single discharge in Fig.(a). Only single pulse is measured in Fig.(b), because the convergent time in (a) is shorter than one in (b). In Fig.(c), the X-ray is emitted at initial current, because of the electron bombardment to anode.

B. Pinhole photograph

The spatial distributions of soft X-ray are measured with a pinhole camera. Fig.3 shows the schematic diagram of the pinhole camera. The camera is placed in the vacuum chamber. The diameter of the pinhole is 400 μ m. The aluminum filter with thickness 2 μ m is located behind the pinhole. The film is FUJI medical X-ray film(SUPER HR-A).

Fig.4 shows the spatial distributions of soft X-ray. The films were developed after four discharges in (a) and (c), and the four hot spots are observed in Fig.(a). In Fig.(b), only single spot is observed. The hot spots are produced in the middle between the electrodes. In Fig.(c), the bright place is near anode because of the electron bombardment.

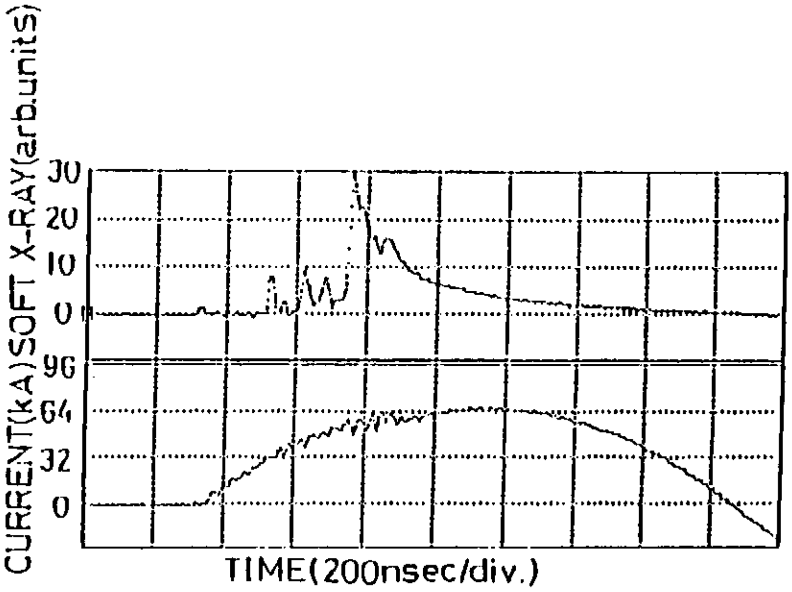

(a)l=1cm, 2r=5mm

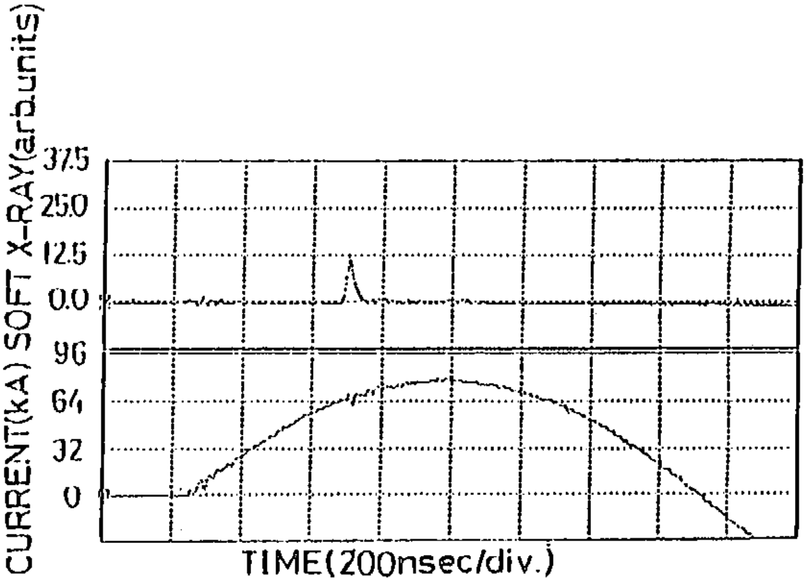

(b)l=1cm, 2r=18mm

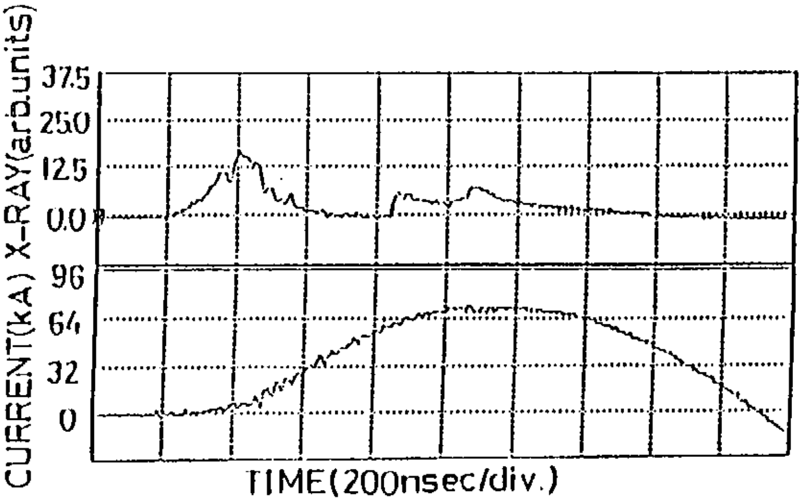

(c)l=2cm, 2r=18mm

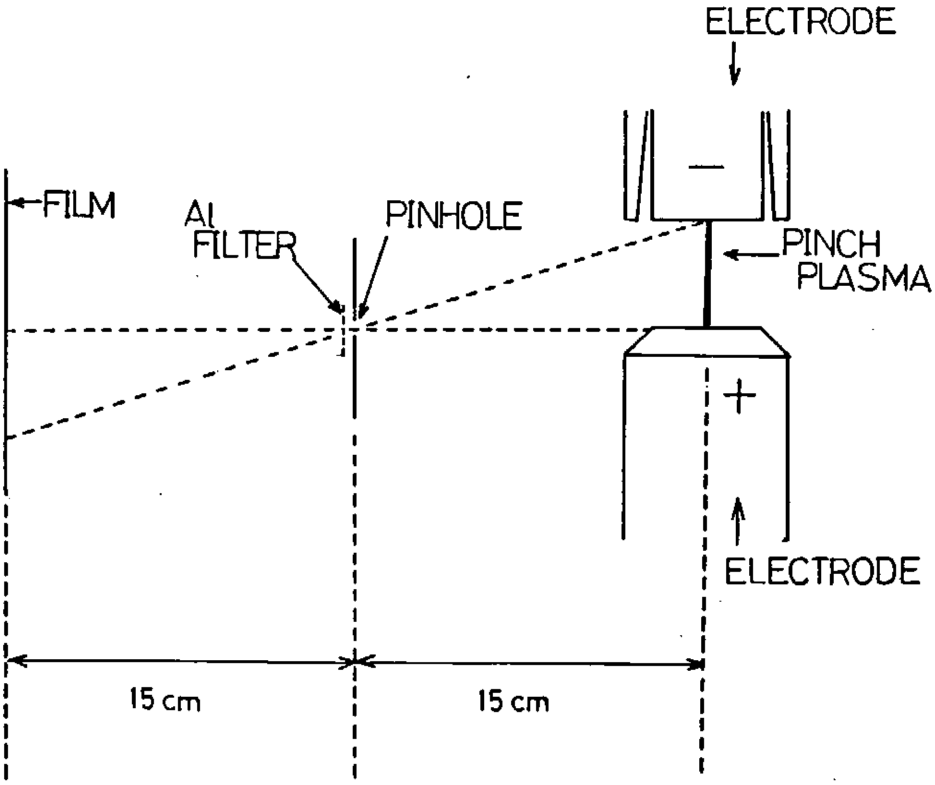

Fig.3 Schematic diagram of the pinhole camera

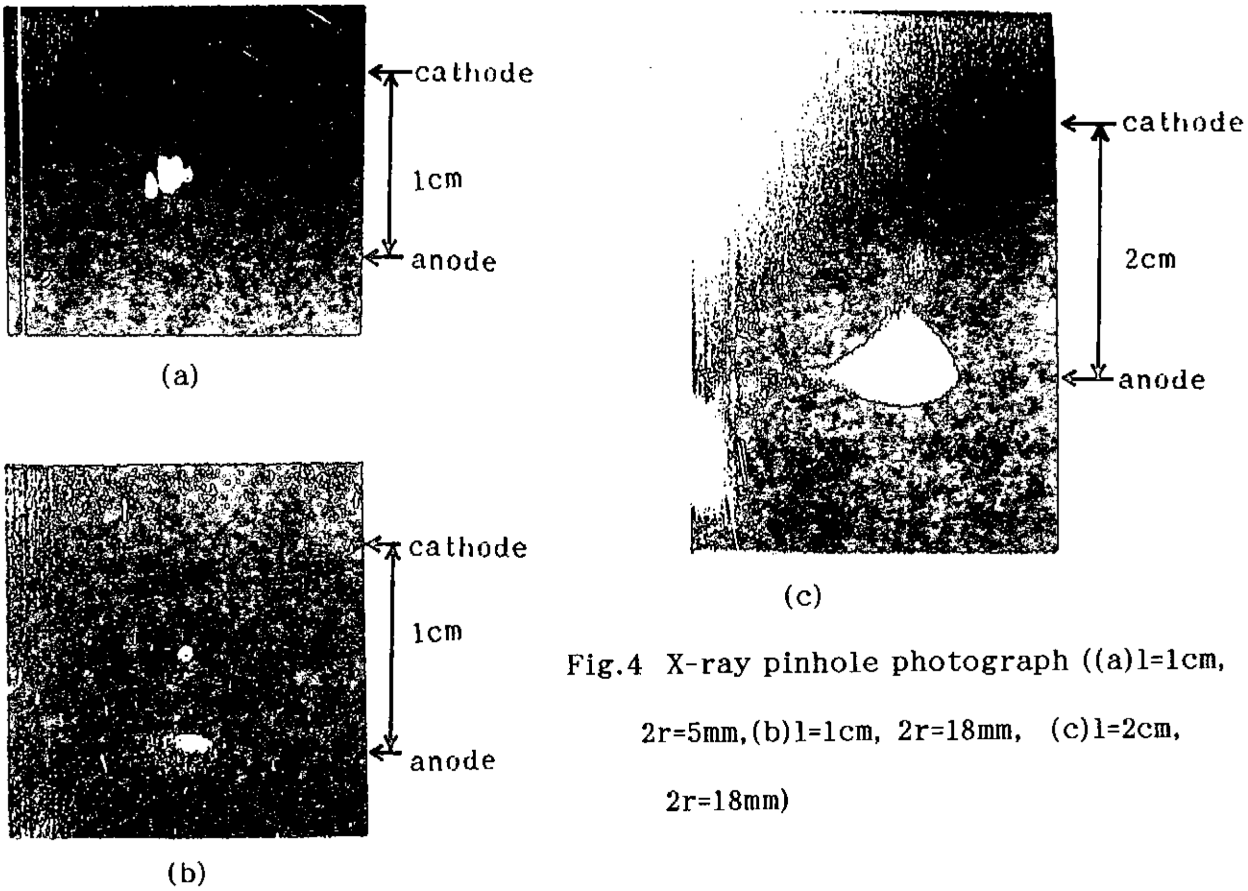

(a)

(b)

(c)

Fig.4 X-ray pinhole photograph ((a)l=1cm, 2r=5mm,(b)l=1cm, 2r=18mm, (c)l=2cm, 2r=18mm)

4. Simulated Results and Discussions

An initial gas pressure as one of unknown parameters is determined by a comparison between experimental and simulated results. The snow plow model⁽⁵⁾ is used here.

Fig.5 shows the simulated results. The upper and lower figures are in the cases of 2r=18mm and 5mm respectively. Two arrows mean the time and the current of soft X-ray emission in the experiment. From Fig.5, the initial gas pressures are near 1Torr.

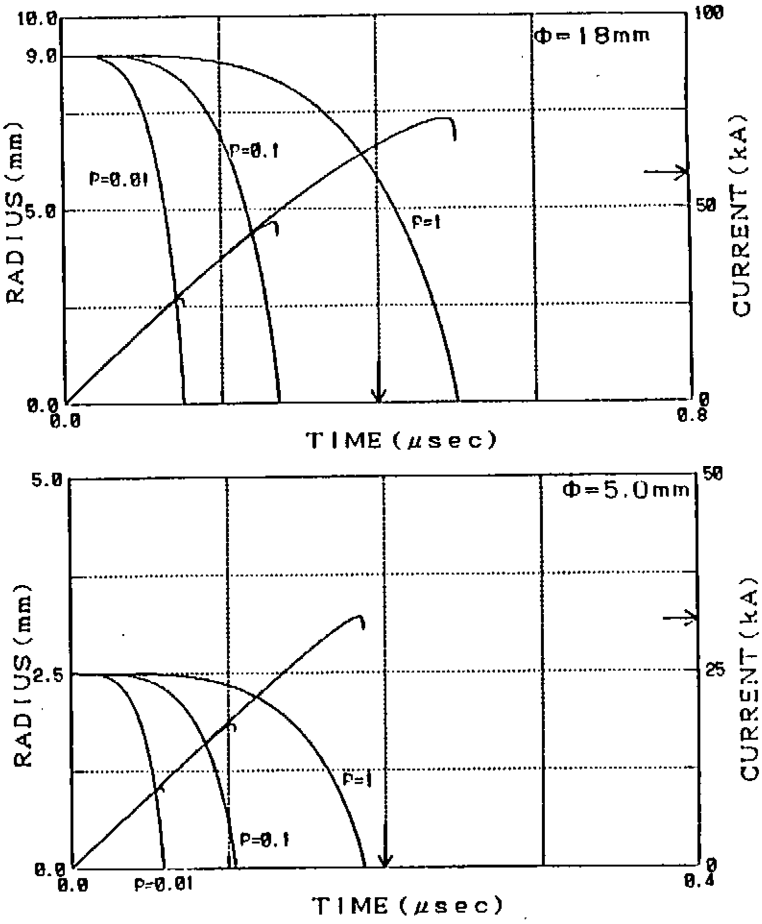

Fig.5 Simulated result

5. Summary

The gas-puff z-pinch device, which has no triggered spark gap, was constructed, and the soft X-ray was observed. The number of soft X-ray pulses changes by the diameter of injected gas. Hot spots were observed in the middle between the electrodes. The X-ray emission is observed near the surface of anode in the case of longer gap separation, because of the electron bombardment to anode.

The initial gas pressures are determined from the comparison with the experimental and simulated results, and are near 1Torr.

References

1)I.N.Weinberg and A.Fisher : Appl.Phys.Lett., 47 (1985) 1116

2)J.Kirz and H.Barback : Rev.Sci.Instrum., 56 (1985) 1

3)P.G.Burkhalter, et al. : J.Appl.Phys., 50 (1979) 4532

4)R.B.Spielman, et al. : J.Appl.Phys., 57 (1985) 830

5)W.Clark, et al. : J.Appl.Phys., 53 (1982) 5552

6)H.A.B.Bodin, et al. : Nucl.Fusion, 1 (1960) 54

X-ray Radiation from a Gas-puff Z-pinch Plasma

K.Takasugi, A.Takeuchi*, H.Takada**, M.Kimura
and T.Miyamoto

Atomic Energy Research Institute
Nihon University

ABSTRACT

A z-pinch experiment was carried out with a hollow-shaped Ar gas-puff. Three types of discharge were found depending on the delay time of discharge from gas-puff detection.

Strong x-ray radiations were emitted from spots, a volume with cloud structure and the anode surface. Number of x-ray spikes observed in a scintillation probe signal is correlated with spot images of an x-ray photograph. X-ray bursts are sometimes observed.

Energy analysis of the x-ray pictures show that the x-ray emission taken in the pictures is concentrated in the energy range 8 - 10 keV. Although the emission from the bulk plasma is not involved in this range, materials evaporated from the electrode are considered to play an important role on the x-ray radiation, then the dynamics of the z-pinch itself.

---

* Present address : Ishikawajima-Harima Heavy Industries.

** Present address : Toshiba Corporation.

INTRODUCTION

A gas-puff z-pinch has become attractive as an intense x-ray source for many purposes. The advantages of the device are repetitive, reproducible, small in spot size, and tunable in wave length with its operation gas. Several experiments are performed with the gas-puff z-pinch,[1,2] and the existence of hot spots is confirmed. Formation of the spot is attributed to electron acceleration by local pinch formation.

The z-pinch plasma is one of the high energy density plasmas which are available in laboratory. In the system, the plasma pressure is sustained by the self-magnetic field. In such a plasma, the role of radiation loss is important not only on the energy balance but also on the dynamics itself. The radiative collapse has been discussed for bremsstrahlung radiation,[3,4] and has been also treated by numerical calculation.[5] Experimentally micropinch formation on a plasma focus is discussed in relation to heavy impurities.[6]

The subject of this experiment is to understand the basic characteristics and the mechanism of x-ray emission from the gas-puff z-pinch. In this report, we show experimental observations of x-ray radiation from the z-pinch plasma and the source of x-ray emission, and its relation to the pinch formation is discussed.

GAS-PUFF Z-PINCH DEVICE

Figure 1 is the experimental setup of "SHOTGUN" z-pinch device at Nihon University. The anode, which is made of brass, has a hollow shaped laval nozzle with inner diameters ranged from ϕ16 mm to ϕ36 mm. Supersonic gas is injected between two electrodes. The cathode is also made of brass, and this is a flat plate with many holes to pass excess gas. The discharge chamber is evacuated less than 10^{-5} torr.

Operation gas is puffed by a high speed gas valve. Solenoid coil wound on the valve is energized by 600 V - 1200 μF

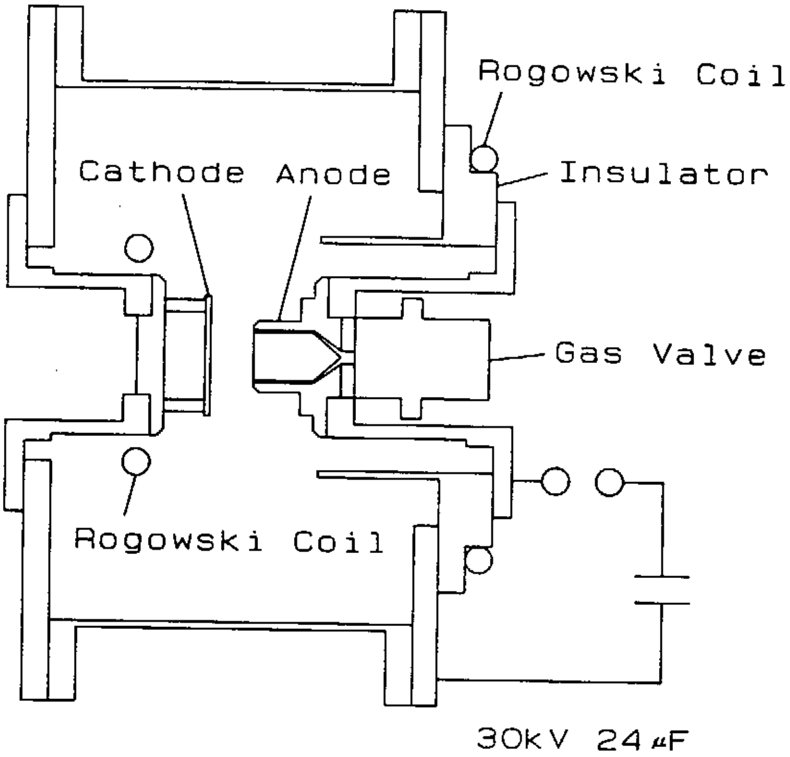

Fig.1. Schematic diagram of the SHOTGUN z-pinch device.

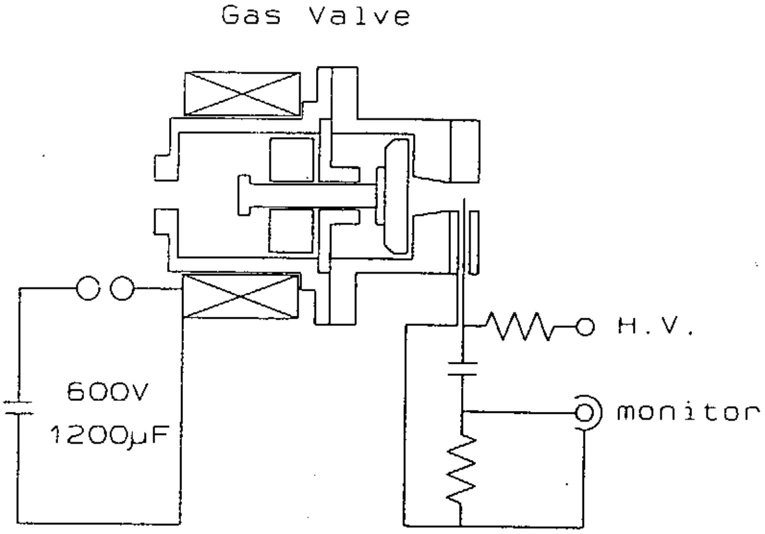

Fig.2. Principle of gas-puff detection.

capacitor, and then it attracts an iron hammer inside the valve vessel, which strikes to open the valve (Fig.2). A pin-probe is placed at the exit of the valve. The probe is charged to 1 kV, and breakdown occurred at 0.2 torr for Ar gas. The breakdown signal is transfered to shield room by an optical fiber, and is used for triggering the z-pinch discharge. The delay time τ_d of the trigger is counted from this signal.

DIAGNOSTICS

Two rogowskii coils are located for detecting the discharge currents as shown in Fig.1. The anode coil is used to measure the total input current through the anode. The cathode coil is placed inside the chamber, which detects the current between both electrodes. The difference between two signals means current leakage between the electrodes.

Ultraviolet (UV) light is detected by an X-ray Diode (XRD). This is a secondary emission detector, and is basically used for detecting soft x-rays. As the signal transmission line is sensitive to electrical noise, Ni cathode XRD is directly exposed to plasma without window in this experiment. The energy range of the XRD is 20 eV - 3 keV.

A scintillation probe with 5 μm Be window is used to detect the x-ray. An NE-102A scintillator is used in the probe. The scintillation light is directly introduced to the shield room by an optical fiber. The energy range of the probe is > 1 keV.

An x-ray pinhole camera is used to take time-integrated picture of x-ray image. The camera has four pinholes, and four different x-ray filters can be used simultaneously to get informations on the energy. Fuji HR-A medical x-ray film with G-8 intensifying screen is selected for taking soft x-ray image.

EXPERIMENTAL OBSERVATIONS

The z-pinch discharge was carried out with Ar gas-puffing. The plenum pressure is 4 atm relative to atmosphere. The gas is in-

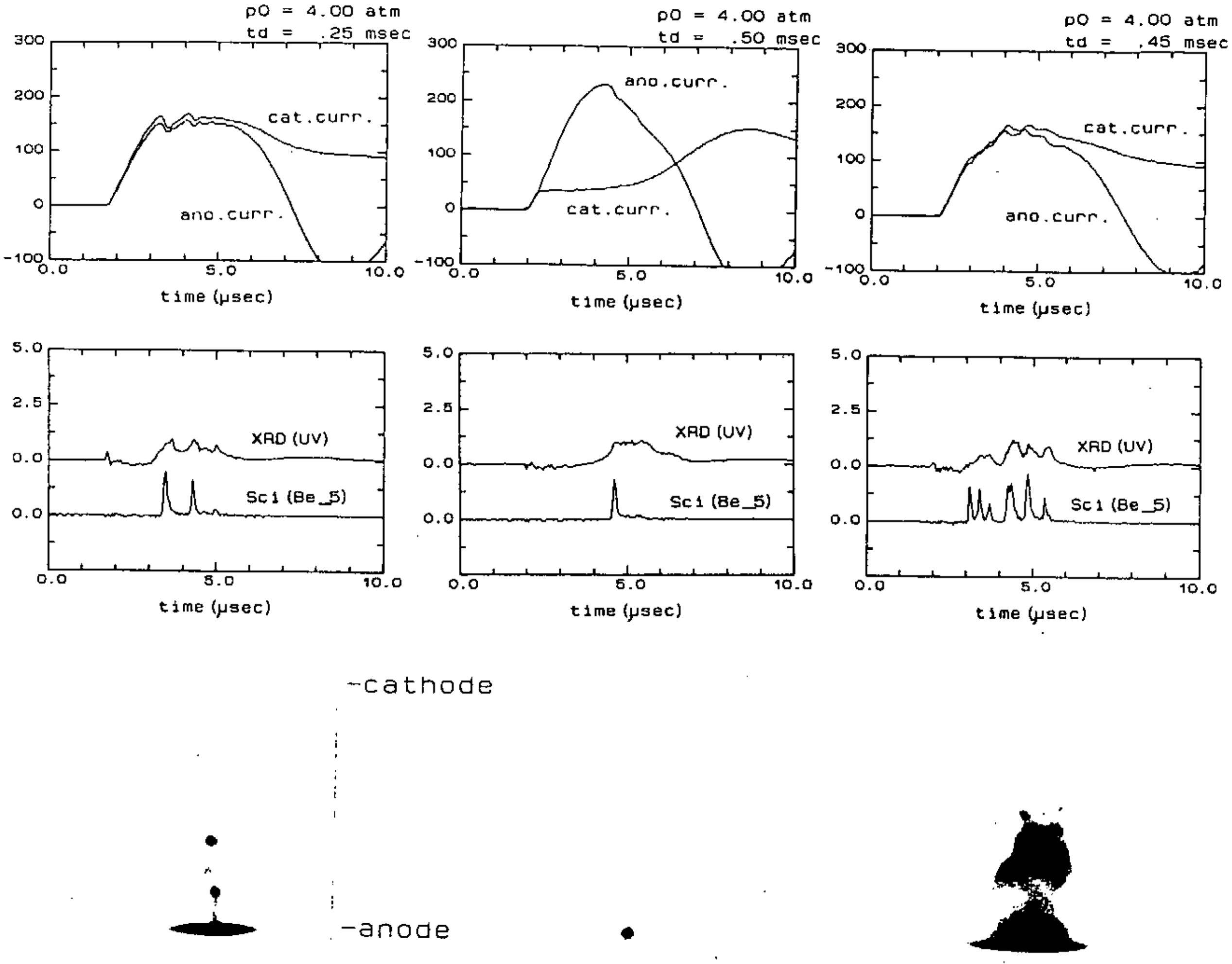

Fig.3. Typical current waveforms, UV and x-ray signals, and x-ray photographs at (a) τ_d=0.25 msec, (b) τ_d=0.5 msec and (c) τ_d=0.45 msec.

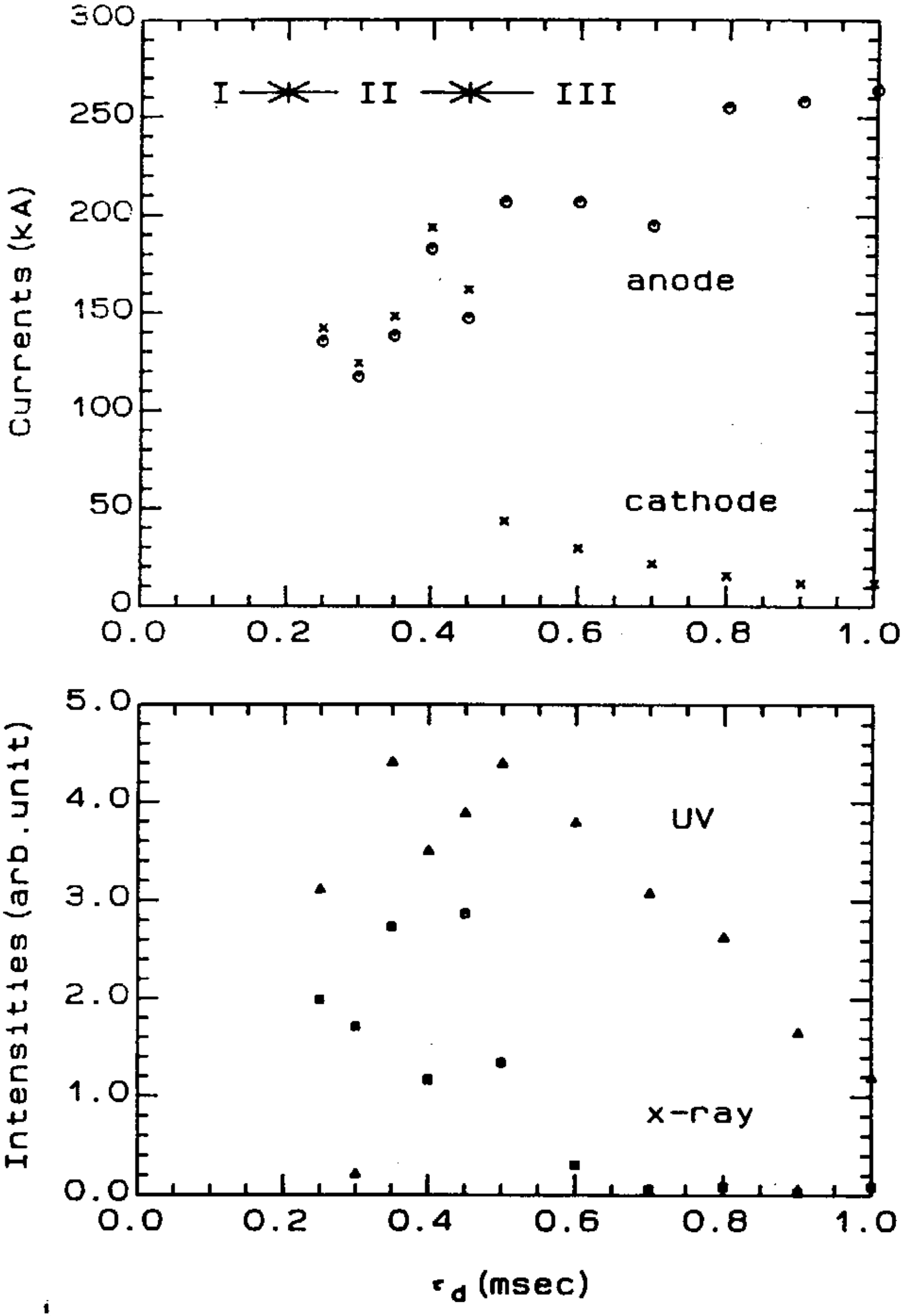

Fig.4.(a) Anode and cathode currents measured at the peak of x-ray signal as a function of the delay time τ_d from gas-puff detection.

(b) Integrated value of UV and x-ray signals.

jected into the chamber through the nozzle with inner diameter ϕ 26 mm, and the distance between the electrodes is 44 mm. Typical current waveforms, UV and x-ray signals, and x-ray photographs are shown in Fig.3. The delay of discharge from gas-puff detection τ_d is taken as a parameter.

At τ_d = 0.25 msec, the cathode current follows the anode one until its peak value as shown in Fig.3(a). Two x-ray spikes are observed simultaneously with current dips. In the x-ray photograph, two small spots, an emission with a cloud structure and an emission from anode surface were observed. Usually the number of x-ray spikes corresponds to that of spot images. This is the case of typical z-pinch discharge. After the current peak, the anode current oscillates, and the cathode one decays slowly. This is the same phenomenon observed in LIMAY-I.[7,8]

At τ_d = 0.5 msec, the cathode current is left from the anode current (Fig.3(b)). The difference between the anode and cathode currents shows the leakage of current between the electrodes. An x-ray spike is also observed at the dip of anode current. The current dip occurs just after its peak. Then the pinch occurs near the anode as shown in the x-ray picture, which is independent to the cathode current. This is the case of plasma focus-like discharge.

At τ_d = 0.45 msec (Fig.3(c)), bursts of x-ray emissions were observed. This phenomenon sometimes occur on z-pinch discharges. Although this cannot be anticipated, the total x-ray output is intense. The cloud structure of the x-ray image is seen entirely.

Figure 4(a) shows the anode and the cathode currents at the peak of x-ray signal. Three regions are shown for τ_d. In the region II, the discharges are conventional z-pinches. The current flows between both electrodes without leakage until its peak value. UV and x-ray signals are relatively strong. The x-ray bursts like Fig.3(c) are sometimes observed. In the region III, the x-ray signal is still observed. The difference between the anode and cathode currents indicates the focus-like discharge between anode and chamber wall. In the region I, the gas is not filled between the electrodes. Then the discharge starts with a long and random delay from the trigger pulse.

X-ray transparency of the filter materials of the x-ray camera

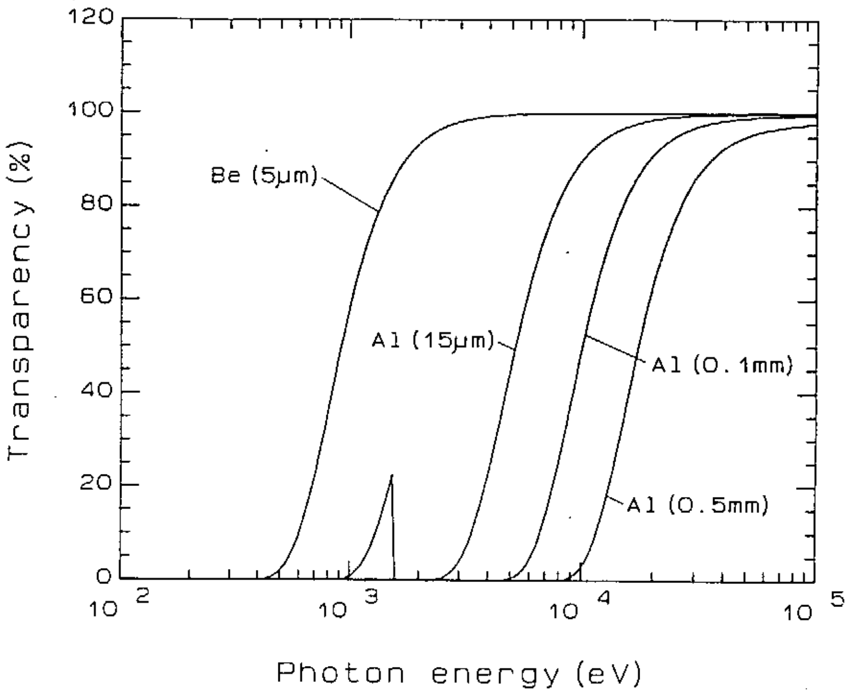

Fig.5. X-ray transparency of Be(5 μm), Al(15 μm), Al(0.1 mm) and Al(0.5 mm).

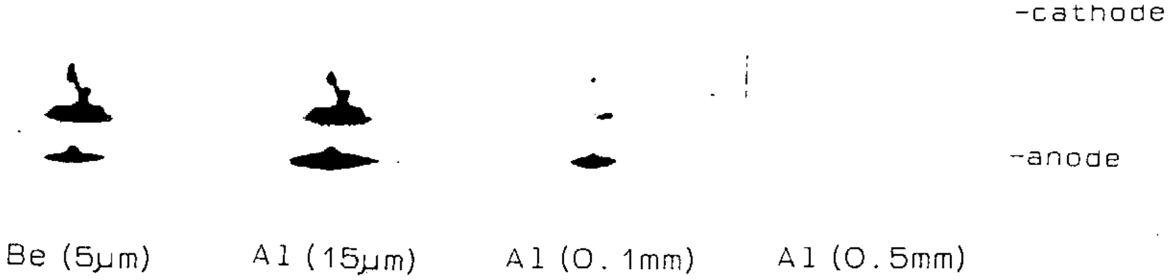

Fig.6. Typical x-ray photographs taken in a shot with different filters.

is shown in Fig.5 as a function of photon energy. The filters of 5 μm Be, 15 μm Al, 0.1 mm Al and 0.5 mm Al are used for comparison. As the space between the filters (windows) and the film is filled with atmosphere, x-rays with energy less than 3.5 keV are absorbed. So the difference between the pictures with the filters of 5 μm Be and 15 μm Al is negligible. Typical x-ray pictures taken in a shot with different filters are shown in Fig.6. In this discharge, the inner diameter of the nozzle is ϕ 36 mm and the distance between the electrodes is 25 mm. A remarkable and spatially uniform attenuation between the photographs with 0.1 mm Al and 0.5 mm Al is shown. The energy range between two filters is 8 - 10 keV. Cu-K (8.9 keV) and Zn-K (9.6 keV) x-rays are involved in this range. Ar-K (3.2 keV) x-ray is greatly attenuated, so that the bulk structure of the pinched plasma is not shown in the picture.

SUMMARY AND DISCUSSION

There are three types of discharges as shown in Fig.4, I. the vacuum discharge, II. the z-pinch discharge between two electrodes, and III. the plasma focus-like discharge. In the region III, a single spike of x-ray emission is observed. The pinch occurs in front of the anode, which is independent of the discharge between two electrodes. The strong x-ray emission is observed at the type II discharge. The spot emissions, the emission in the cloud structure and the emission from the anode surface are observed in x-ray image. The bursts of x-ray are sometimes observed in this discharge, which accompanies a strong emission with the cloud structure. The relation between the cloud-like emission and the pinch formation is not clear.

The four x-ray pictures with the different filters show that the x-ray emissions taken in the pictures are concentrated in the energy range 8 - 10 keV. In this range, the strong lines of the electrode materials (Cu and Zn) are involved. If the x-rays of the spots are emitted from those materials, they will directly affect the dynamics of the z-pinch itself.

As the number of x-ray spikes is correlated with the spot images, the spots are accompanied by pinch formations. A spot is seen near the anode on a single emission, and some spots are distributed center region on multiple emissions. The spot emissions are considered to start at the anode and move toward the cathode with blinking. According to this model, the velocity of the blinking emission is 1.2×10^6 cm/sec for Fig.3(a), which corresponds to 45 eV for Cu atom. This do not necessarily mean that some material of the emission source move toward the cathode. There is a possibility of inclined distribution of the material.

Once the materials are evaporated, they penetrate the discharge column, then become ionized. If the atoms are fully ionized, bremsstrahlung radiation loss has Z^4 dependence, where Z is atomic number. Anyway those high-z impurities are expected to shine brighter than the operation gas. The radiative power loss concentrates on the impurities. Then a radiative collapse will occur at the plasma involving heavy impurities. The nonuniformity in the impurity distribution will trigger MHD instabilities. In this problem, atomic processes must be treated exactly to calcurate the energy loss. This is an important subject in plasma dynamics, and the role of radiative power loss is important in z-pinch formation and control, and its application to x-ray source.

One of the authors (K.T.) appreciates Dr. F.J.Wessel for the discussions on z-pinch operation and measurements.

REFERENCES

1) J.Shiloh, A.Fisher and N.Rostoker : Phys. Rev. Lett. 40, 515 (1978).
2) N.R.Pereira and J.Davis : J. Appl. Phys. 64, R1 (1988).
3) R.S.Pease : Proc. Phys. Soc. London Ser. B70, 11 (1957).
4) S.I.Braginskii : Sov. Phys. JETP 6, 494 (1958).
5) B.E.Meierovich : Sov. J. Plasma Phys. 11, 831 (1985).
6) K.N.Koshelev et.al.: Sov. J. Plasma Phys. 15, 619 (1989).
7) K.Takasugi et.al.: AIP Conf. Proc. 195, 466 (1989).
8) H.Akiyama et.al.: Rev. Sci. Instrum. 61, 1344 (1990).

DEVELOPMENT OF WIRE AND COIL DESIGNING FOR HIGH-MAGNETIC FIELD GENERATION

Giyuu KIDO

Institute for Materials Research, Tohoku university,
Aoba-ku, Sendai 980

Abstract

The ultimate tensile strength, and electric conductivity have been investigated for Cu(Nb), Cu(Be), Cu(Cr), Cu(Ag), and Cu(Nb-Ti) wires in order to produce higher magnetic field than 50 T. The highest tensile strength is realized in Cu(Nb) wire. The Cu(Nb) and Cu(Ag) are regarded as the best materials for the nondestructive pulsed-magnetic-field generation.

The coil designing was also studied to generate high magnetic field. It was found that the fiberglass reinforcement of wire by layer by layer is quit effective to produce high pulsed magnetic field. By using this technique, a 55 T field can be generated even using pure copper wire. The usage of water (ice) for solidifying the solenoid shortens considerably the cooling time of the pulsed magnet.

$1. Introduction

High magnetic fields have continuously provided nobel phenomena in semiconductor, superconductor, magnetic substances, plasma, etc. Since the large Maxwell stress is imposed at the solenoid coil during the generation of high magnetic field, the maximum intensity of the field is limited by the ultimate tensile strength of the wire. The solenoid requires the materials with characteristics of not only high conductivity but also high tensile strength to produce high magnetic field non-destructively. Generally, copper-base alloys have much better conductivity than that of ferroalloys. Long pulsed fields exceeding 10 ms can be generated by copper-base alloy wires. I have investigated the conductivity and ultimate tensile strength in Cu(Nb), Cu(Be), Cu(Cr), Cu(Ag), and Cu(Nb-Ti) wires.

On the other hand, the maximum intensity of the magnetic field can be increased by the designing of the solenoid coil and reinforcement. New techniques of the pulsed magnet are described briefly.

$2. Wire properties

2-1 Cu(Nb)

The tensile strength of Cu(Nb) wire increases with drawing process and reaches to 200kG/mm^2 1). Fine filaments assist the strength of the wire. The maximum long-pulsed-magnetic-field of 68.4 T was produced by Foner using this sort of wire 2). His wire has ultimate tensile strength of 126 kG/mm^2. The homemade wire was made by Ikeda as follows. At first, Cu and Nb pellets were mixed and melt in a calciner crucible furnace. Then, the resultant ingot of 20 mm in diameter was drawn by the machine. The Nb concentration is 19 wt% (17 vol%). Fig. 1 shows the tensile strength as a function of reduction rate. The wire of strength higher than 150 kg/mm^2 can be attained for the reduction rate of 10^4. In order to use 2 mm wire, we should start the ingot of 20 cm in diameter or bundle the fine wires.

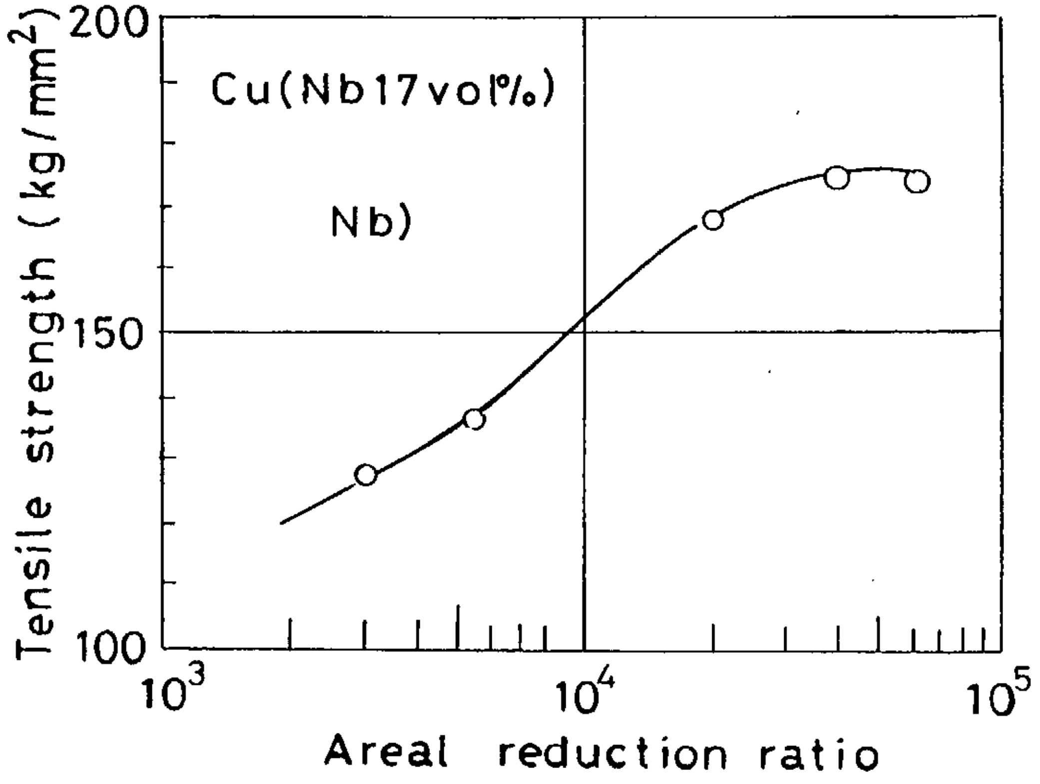

Fig. 1 tensile strength vs. reduction rate of Cu(Nb).

I also asked to make the Cu(Nb 18 wt%) wire at Vacuum Metallurgical Co., Ltd. The starting ingot was 30 mm in diameter and final diameter was 1.93 mm. The tensile strength reached to 91 kg/mm^2, and the resistivity was 3.1 $\mu\Omega\cdot$cm at room temperature.

2-2 Cu(Be)

The highest tensile strength of copper-base alloy has been reported in this materials system. The wire of Cu(Be 2wt%) was made by NGK Insulators, Ltd, and the insulation was rapped by The Fujikura Cable Works, Ltd. The ingot was solution treated and drawn into the wire. The ultimate tensile strength is approximately 95 kg/mm^2, and the resistivity is 11 $\mu\Omega\cdot$cm after the drawing. The tensile strength and conductivity increase by 40% with the precipitation hardening at approximately 400℃ for one hour. However, the wire becomes brittle by this heat treatment. The hardening should be made after the winding of the solenoid. Our pulsed magnet was wound by the solution treated wire. Up to 55 T has been generated in 2 ms pulsed field3).

2-3 Cu(Cr)

In order to design long pulsed magnet, the resistivity should be lower than 0.5 $\mu\Omega\cdot$cm at 77 K. The Cu(Cr) wire is less-expensive to attain, since no special drawing process is needed and no expensive raw materials are required. Our wires were mainly produced by The Fujikura Cable Works, Ltd. The yield strength reaches to 45 kg/mm^2, and the resistivity at 77 K is as small as one half of that of pure copper wire. The maximum field attained using this wire was 43 T4).

2-4 Cu(Ag)

Cu(Ag) had been used militarily in USA during the World War II because of the remarkable elasticity. The tensile strength increases with increasing silver concentration and reaches its maximum (more than 100 kg/mm^2) around 10 at%5,6). We have made both the wire and plate with Cu(Ag 38 at%) alloy at Tanaka Kikinzoku Kogyo K. K. The ultimate tensile strengths of wire and plate were 45 and 54 kg/mm^2, respectively. The resistivity of wire was 2.21 $\mu\Omega\cdot$cm at room temperature and 0.288 $\mu\Omega\cdot$cm at 77 K. It was found that the conductivity of this matter is almost same as that of copper.

2-5 Cu(Nb-Ti)

Usually, the copper part is used for the current stabilization in a superconducting wire, and which shares more than one third of the wire cross-section. However, the ultimate tensile strength of Nb-Ti is more than 5 times stronger than that of copper. When using this wire at the normal state, the current mainly flows in the copper part and the wire is sustained by the superconductor part. I asked Kobe Steel, Ltd. to make the Cu(Nb-Ti) wire for the pulsed-magnet-operation. The characteristics of wires, which had been tested, are shown in table 1. Herlach et al. reported that they could generate 67 T in 12 mm bore using Cu(Nb-Ti) wire with fiberglass reinforcement7).

Table 1. Ultimate tensile strength and electric resistivity of copper-base wires for pulse magnet.

Wire	Tensile Strength	Resistivity RT	Resistivity 77 K	reference
Cu(Nb 17vol%)	91 kg/mm^2	3.1	0.87 μΩ · cm	
Cu(Nb 18vol%)	126	2.9	0.82	2)
Cu(Be 2wt%)	95	10.7	9.2	
Cu(Cr 2wt%)	43	2.2	0.6	
Cu(Ag 38at%)	45	2.2	0.29	
Cu(Ag 12at%)	90	2.3	–	6)
Cu30%(Nb-Ti)	70	5.8	1.8	

$3 Magnet designing

The highest field is gained by the reinforcement of solenoid coil. Recently, Herlach et al. reported that the fiberglass reinforcement of wire is quit effective to produce high pulsed magnetic field7). Figure 2 schematically shows the cross-section of their pulse magnet. Each wire layer is sustained by thin fiberglass layer, and the coil is reinforced by the thick layer. The fiberglass has the tensile strength of 300 kg/mm^2. At the liquid nitrogen temperature, the fiberglass is stronger than the Kevlar (aramid fiber: registered by Du Pont) though this relation is opposite at the room temperature. By employing this technique, a 55 T field can be generated using a pure copper wire. Without the sustainment between wire layers, higher than 40 T was quit difficult to produce with the copper wire.

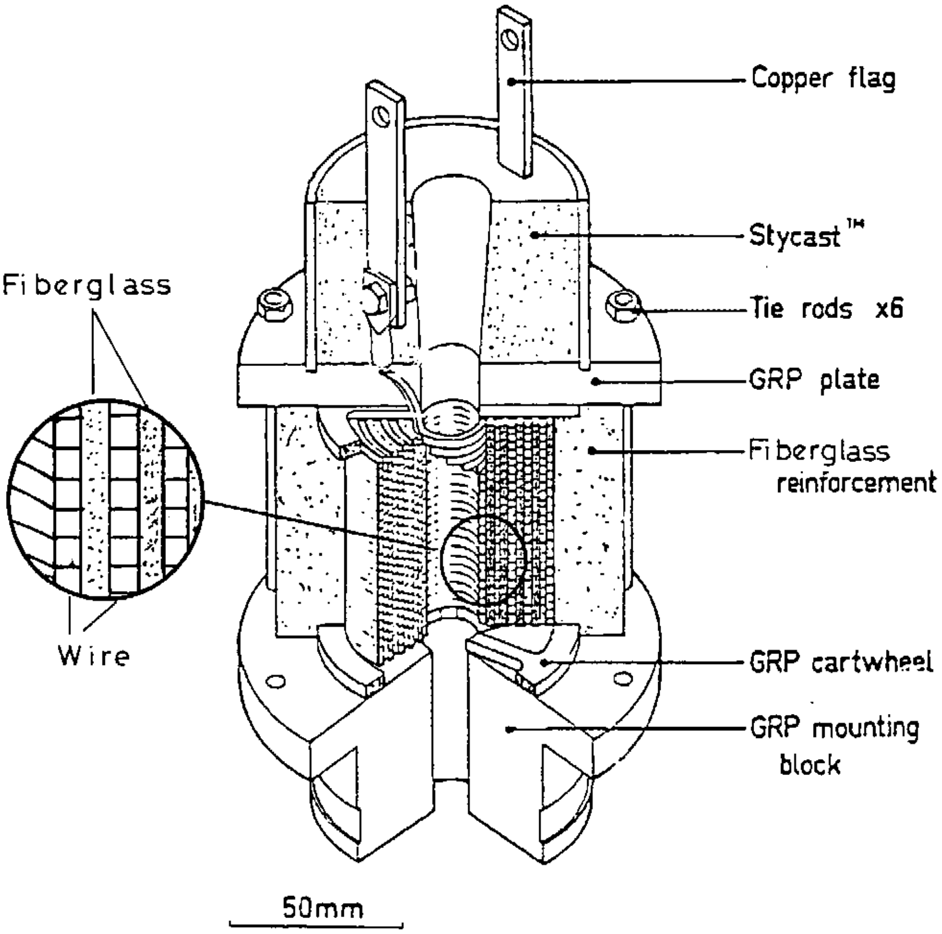

Fig. 2. Cross-section of brand-new pulsed magnet developed by Herlach et al.

A rapid cooling of solenoid coil is desirable to apply the pulsed magnetic fields in the experiments. The usage of water (ice) for solidifying the solenoid is proposed by Motokawa to make a pulsed magnet economically[8] (see Fig. 3). The author found that the magnet of this type cools down to 77 K in a few minuet after the generation of 40 T field. This time interval is less than one tenth of that using epoxy for solidifying the solenoid.

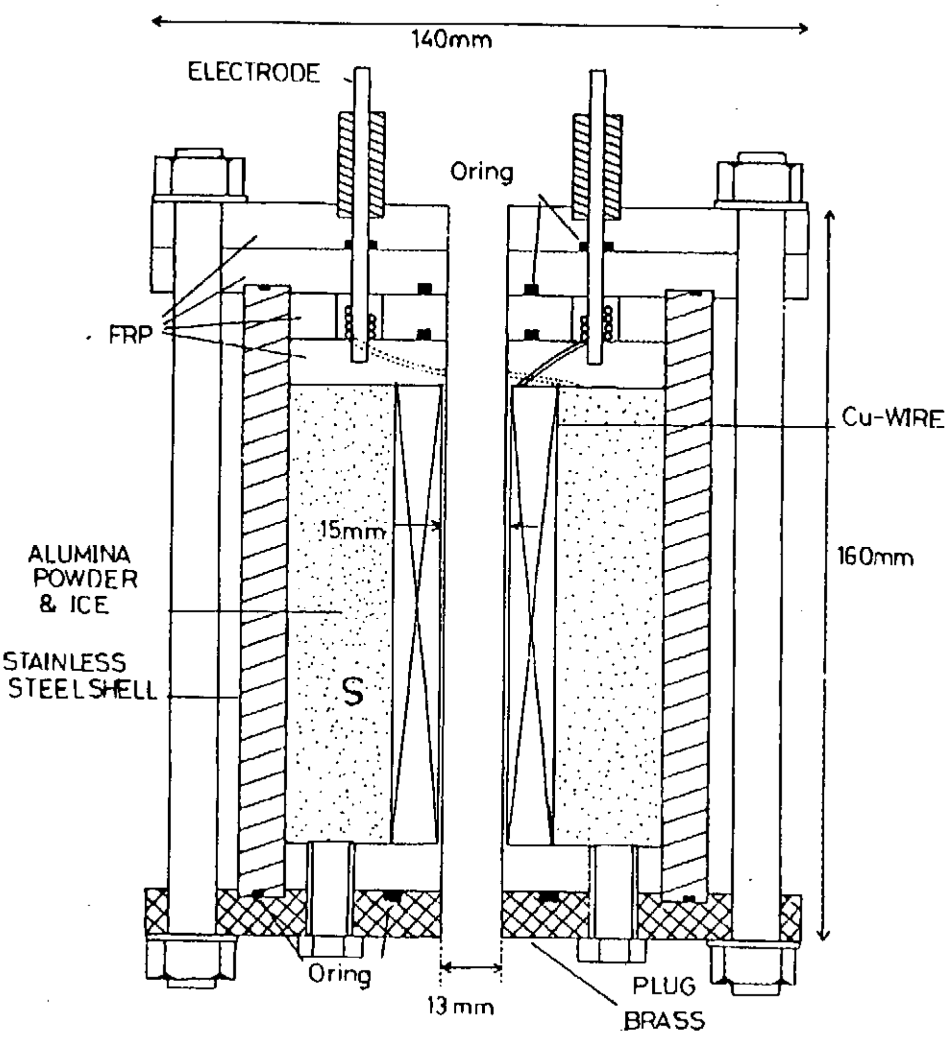

Fig. 3. Cross-section of Motokawa pulsed magnet.

$4 Summary

The yield strength of the copper-base alloy was investigated to produce the highest pulsed magnetic field nondestructively. Both Cu(10%Ag) and Cu(Nb) wires are regarded as the best materials because of its high strength and conductivity.

A fiberglass reinforcement against the wire layer remarkably increased maximum field strength. An 80 T field possibly will be generated by employing the Cu(Nb) wire, fiberglass reinforcement and ice adhesion.

Acknowledgments

The author wish to thank Professor K. Ikeda for the collaboration on Cu(Nb) material. Thanks are also due to Professor M. Motokawa for cooperation on the ice adhesive magnet. He also wish to thank Professor F. Herlach for the colaboration and showing details of his magnet before the publication.

References

(1) J. Bevk, J. P. Harbison, and J. L. Bell, J. Appl. Phys. 49 (1978) 6031-6038.

(2) S. Foner, E. Bobrov, C. Renaud, E. Gregory, and J. Wong, IEEE Trans. Mag., 24 (1988) 1059-1062.

(3) G. Kido, S. Kajiwara, Y. Nakagawa, S. Hirosawa, and M. Sagawa, IEEE Trans. Mag., MAG-23 (1987) 3107-3109.

(4) G. Kido, and K. Hiruma, Solid State Physics, 13 (1978) 417-421.

(5) Denki Zairyou Binran, Supplement (ed. S. Komagata: Kinbara Publishing, Tokyo, 1948) pp. 8 and 14

(6) Y. Sakai, K. Inoue, and H. Maeda, Bull. Jpn. Institute Metals (1990, Spring) pp. 245.

(7) F. Herlach, Private communication

(8) M. Motokawa, H. Nojiri, and Y. Tokunaga, Physica B, 155 (1989) 96-99

Recent Issues of NIFS-PROC Series

NIFS PROC-1	*U.S.-Japan Workshop on Comparison of Theoretical and Experimental Transport in Toroidal Systems Oct. 23-27, 1989* ; Mar. 1990
NIFS PROC-2	*Structures in Confined Plasmas –Proceedings of Workshop of US-Japan Joint Institute for Fusion Theory Program–* ; Mar. 1990
NIFS PROC-3	*Proceedings of the First International Toki Conference on Plasma Physics and Controlled Nuclear Fusion –Next Generation Experiments in Helical Systems– Dec. 4-7, 1989* ; Mar. 1990
NIFS PROC-4	*Plasma Spectroscopy and Atomic Processes –Proceedings of the Workshop at Data & Planning Center in NIFS–*; Sep. 1990
NIFS PROC-5	*Symposium on Development of Intensed Pulsed Particle Beams and Its Applications*; Oct. 1990
NIFSPROC-6	*Proceedings of the Second International TOKI Conference on Nonlinear Phenomena in Fusion Plasmas -Theory and Computer Simulation*-Apr. 1991